QUANTUM SIMULATION WITH PERIODICALLY DRIVEN SUPERCONDUCTING CIRCUITS

by

Mahdi Sameti

Submitted in conformity with the requirements
for the degree of Doctor of Philosophy in Physics

School of Engineering & Physical Sciences

Submitted April, 2018

Abstract

Superconducting quantum circuits have made tremendous advances in realizing engineered quantum dynamics for quantum simulation and quantum information processing over the past two decades. Technological developments in the field of superconducting circuits have raised them to be the leading platform for implementing many-qubit systems. This thesis introduces a sequence of concepts for engineering spin-lattice Hamiltonians in analog quantum simulation with superconducting circuits. Our approach to quantum simulation is to engineer driving schemes that lead to implementations of the desired models. The applications of this approach are in our work mainly centered around two types of systems: interesting many-body topological quantum systems, namely Kitaev's toric code and honeycomb model and two-body systems that can be employed as building blocks of larger quantum simulators or quantum computers. In the first part of this thesis, we make a proposal for an analog implementation of the toric code in superconducting circuits. We also discuss a realistic implementation of this model on an eight qubit lattice. In the second part, we present our analog approach for implementing arbitrary spin-spin interactions in linearly and nonlinearly coupled superconducting qubits. Our proposed toolbox has the potential of easy generalization to a variety of systems and interactions. Lastly, based on our two-body toolbox, we set forward two possible implementations of the Kitaev honeycomb model and show that the engineered two-body interactions work - with good accuracy - in this many-body model.

Acknowledgements

I would like to first thank my supervisor Prof. Michael J. Hartmann for providing the opportunity to do my Ph.D. with him. I was so lucky to have such a nice, caring and supportive person as my supervisor and I'm very much grateful to him for all his continuous supports, advices, encouragements, flexibility, patience and kindness during the course of my M.Sc. and Ph.D. and for all I've learnt from him. I would like to thank our collaborators in the Quantum Device Lab at ETH Zurich, Prof. Andreas Wallraff, Dr. Anton Potočnik and Michele Collodo for contributing in the project on the toric code and for giving me the opportunity to be a part of their experimental project on a non-linear coupler. Special thanks goes to my former colleagues at TUM Munich, Dr. Mehdi Abdi, Dr. Peter Degenfeld-Schonburg and Dr. Martin Leib and to my colleagues at Heriot-Watt university, Oliver Brown, with who I shared most of my journey towards my Ph.D., and Dr. Edmund Owen. I would like to extend my warm thanks to Dr. Luca Tagliacozzo for insightful discussions on lattice gauge theories and tensor networks. Huge thanks goes to all my friends who made my Ph.D. a much better and positive experience. Sincere thanks goes to the heads of the department Prof. D. Reid and Prof. G. Buller for their supports towards my scientific travels and to Loraine Markland for all her assistance.

This work is dedicated to my parents. Without your immense and precious support and attention, I never would have reached this stage. Thank you very much for all you did for me before coming abroad to study, after that in Germany and Scotland and for all you will do for me in the future! Thank you very much for being there whenever I needed you, raising my hopes during hopeless times, carrying the pressures with me shoulder to shoulder and tolerating my bitter attitudes. I'm well aware that I could never ever repay any of my debts to you but I hope, through this work, I could give you moments of happiness as a gift. Next to my parents, I'm deeply indebted to my sister and brother, Marsa and Mohammad, whose never-ending kindness was the best companion in my life. May each day of life bring its best for you!

Contents

Publication List

This thesis is based in part on the following publications,

- Mahdi Sameti, Anton Potočnik, Dan E. Browne, Andreas Wallraff, Michael J. Hartmann, *Superconducting quantum simulator for topological order and the toric code*, Phys. Rev. A 95, 042330 (2017).

- Mahdi Sameti and Michael J. Hartmann, *Floquet engineering of arbitrary spin-spin interactions*, to be submitted.

Other publication which is not included in this thesis,

- M. Abdi, P. Degenfeld-Schonburg, M. Sameti, C. Navarrete-Benlloch and M. J. Hartmann, *Dissipative optomechanical preparation of macroscopic quantum superposition states*, Phys. Rev. Lett. 116, 233604 (2016).

Chapter 1

Introduction

This work combines several subjects that have attracted a great deal of attention in recent years in the physics community: superconducting quantum circuits, quantum simulation, topological phases of matter and periodically driven quantum systems. Superconducting circuits are a solid-state platform to test the quantum optical phenomena in the microwave regime. These circuits are endowed with a nonlinear element called Josephson junction which makes it feasible to define two-level quantum systems (i.e. qubits) in such circuits. Thanks to the rapid progresses in the fabrication and measurement of superconducting circuits, they have nowadays been elevated to the position of a forerunner in the race towards implementing quantum computers. Using superconducting circuits, large scale systems, primarily considered to belong to condensed matter physics, can now be studied with photons on a circuit lattice.

In particular, our goal in this thesis is to exploit the potential of superconducting circuits in implementing quantum simulators for intriguing many-body models, i.e. Kitaev topological models, as well as few-body Hamiltonians. The topological models are interesting on their own since they feature phenomena like degeneracy and non-locality of the ground states and exotic quasiparticles called anyons. These phases have broadened our views on phase transitions as the contemporary setting of symmetry-breaking does not apply to them and topological phase transitions do not involve symmetry-breaking. Moreover the nonlocality of their ground states makes them a perfect candidate to encode quantum information since local perturbations cannot destroy quantum information stored in such states. In addition, one can perform fault-tolerant quantum information processing based on anyons. Unfortunately the relevant models do not have direct natural realizations and any implementation of them demands for an artificial quantum system. In this work, based on superconducting circuits platform, we focus on analog implementations of Kitaev's toric code and honeycomb lattice models. In contrast with the digital quantum simulation approach which is based on one- and two-body interactions, in an analog quantum simulation the interactions are directly implemented by designing suitable architectures and engineering external modulations. The heart of this thesis is devoted to explain how efficient modulation schemes can be engineered to lead to desired target Hamiltonians. In addition to the topological models, we employ these schemes in quantum simulations of two-body Hamiltonians. Modulating a quantum system with periodically-driven perturbations, specifically in the field of ultracold atoms and trapped ions, has become a major tool for shaping the properties of quantum systems. We adopt these approaches to superconducting circuits and extend it to the cases with multiple periodic drives.

In the next chapter, we provide an introduction to the field of superconducting circuits. The reader will become familiaraized with the physics of superconducting circuits, their use in quantum information processing as qubits and the Hamiltonian description of an arbitrary superconducting circuit through this chapter. In chapter 3, we discuss the meaning and aims of quantum simulations and approaches to perform a quantum simulation. A brief literature review is provided at the end of that chapter. In chapter 4, we present our results for an analog quantum simulation of the toric code in superconducting circuit using transmon qubits. The toric code includes four body interactions which should be implemented either using a digital approach via a series of two-body interactions or by using of an effective Hamiltonian in an analog approach. Our idea to implement this effective Hamiltonian is to couple the four qubits to an ancilla which is driven via a multi-tone drive at appropriate frequencies. These frequencies are detuned from the transition frequency of the ancilla and via a suiable choice of the parameters, we make sure that any other interaction with the ancilla is off-resonant. As a result, the ancilla can be adiabatically eliminated but the off-resonant interactions effectively lead to desired four-body interactions. The desired four-body interactions can be made - using the right parameters - to be the leading order of an effective Hamiltonian. We then examine a minimal eight-qubit lattice and discuss the possibility of preparing the ground state of the toric code in such lattice using an adiabatic approach.

In chapter 5, we develop a toolbox for analog implementations of two-qubit interactions which is versatile enough to be generalized to other systems. Here our workhorse to engineer desired interactions is Shirley's time independent Floquet formalism. We first apply this formalism to a system with two superconducting qubits with linear coupling, in which the qubits are driven by several types of perturbations. We show that by choosing proper driving protocols with single and two frequencies, arbitrary spin-spin interactions can be implemented in such a circuit. Moreover, the parameters of the effective Hamiltonian can be calculated to an arbitrary high order in perturbation. As a second setup, we consider qubits that are coupled via a driven nonlinear coupling, and show that parity-conserving two-spin couplings are realized in such a circuit by suitable driving.

In chapter 6, we put the engineered two-body couplings of chapter 5 together to make two proposals for implementations of the Kitaev honeycomb lattice model in superconducting circuits based on driven qubits and driven couplings schemes. Finally in chapter 7, we summarize the results of this work and discuss possible future advances that could be built on our work.

Chapter 2

Superconducting quantum circuits

Superconducting circuits have become a promising platform to build engineered and controlled quantum systems with applications in quantum information and quantum computation. In these electrical circuits, all elements e.g. capacitors, inductors, etc. are made of superconducting material like aluminium and the circuit operates inside a helium dilution refrigerator at millikelvin temperatures. Physical implementation of artificial quantum systems have taken many forms: Photons in cavities, ultracold atoms, trapped ions, quantum dots, etc.. Among them, superconducting circuits have the advantage of being relatively simple to fabricate using standard lithographic techniques, all-electrical control of the circuit using microwave fields and large and tunable nonlinearities. This chapter is meant to serve as an introduction to some aspects of superconducting circuits. We first discuss the frequency regime at which superconducting circuits operate in Sec. 2.1. We then start a discussion about building blocks of superconducting circuits by considering the most simple superconducting circuit, i.e an LC resonator in Sec. 2.2. In Sec. 2.3, we introduce a Josephson junction. This nonlinear element can be employed as a circuit element to implement a qubit with superconducting circuits. This issue is discussed in Sec. 2.4. In particular, we analyse a transmon qubit which we use for our designs in this thesis. After introducing the building blocks of superconducting circuits with a single dynamical mode, we discuss some practical architectures with two degrees of freedom. In Sec. 2.5, we discuss circuit

QED i.e. circuit analog of cavity QED, in which a transmon is coupled to a resonator. Then, we present coupling schemes between two transmon qubits in Sec. 2.6. The process of measurement of a transmon qubit is discussed in Sec. 2.7. In the last section of this chapter, we present a systematic approach to derive the Hamiltonian of a many-mode circuit.

2.1 Operating regime of superconducting circuits

There are several energy scales that should be taken into account when working with superconducting circuits. The first one is the *plasma frequency* f_p which is related to the fluctuation of electron density in metals. For aluminium the plasma frequency is $f_p = 3.6 \times 10^{15}$Hz [1]. This is several orders of magnitude larger than the MHz-GHz regime of superconducting circuits. In this regime, the penetration depth of photons is almost zero and plasmon excitations can be well approximated to be in their ground state. The second energy scale is the superconducting gap, Δ. The operating temperature and applied drive frequencies should be well below this energy scale to avoid creating excitations on top of BCS ground state. For aluminium $2\Delta/h \approx 80 - 100$GHz, which sets much lower limit on the temperatures and frequencies than the plasma frequency. The requirement that thermal fluctuations do not create electronic excitations in a circuit defines a limit from below for the working frequencies. For typical fridge temperatures of about 20mK, this will give frequencies of $\omega \gtrsim 5k_BT \approx 2$GHz for a suppression of thermal excitations down to 1 percent for the first excited state.

2.2 Quantum LC oscillator

We start out our journey through superconducting circuits in this section by introducing the simplest superconducting circuit, i.e. an LC circuit. This simple circuit encompasses the underlying physics of more complicated superconducting devices and networks while it also stands as a model for realistic

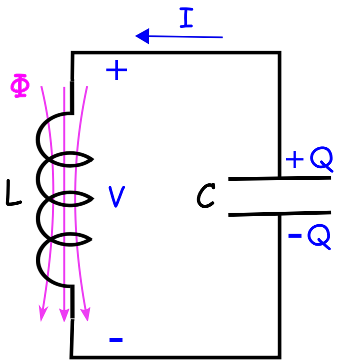

Figure 2.1: Quantum LC circuit.

devices like waveguides and resonators. It consists of a capacitor C in parallel with an inductor L. There are four dynamical variables associated with this circuit. These are the flux Φ through the inductor, the charge Q of the capacitor, the voltage V across the elements and the current $I(=-I_c)$ through the circuit. These dynamical variables are not independent and are related by the following equations,

$$\begin{aligned}\Phi(t) &= \int_0^t V(t')dt', \\ Q(t) &= \int_0^t I_c(t')dt', \\ \Phi(t) &= LI(t), \\ Q(t) &= CV(t).\end{aligned} \tag{2.1}$$

The state of the circuit is then fully determined by a single variable and the rest are recovered by the above equations. In classical circuit theory [3], it is desirable to work with voltages and currents. For example, we can solve the four dynamical equations to derive a second-order equation for the voltage,

$$\frac{1}{L}\int_0^t V(t')dt' = -C\frac{d}{dt}V(t) \Rightarrow \frac{d^2}{dt^2}V(t) + \frac{1}{LC}V(t) = 0. \tag{2.2}$$

The solution of this equation is a sinusoidal function with frequency $\omega = 1/\sqrt{LC}$. In quantum physics, we typically deal with Lagrangians and Hamiltonians which conveniently are written in terms of fluxes and charges instead of voltages and currents. Here we take the rescaled flux,

$$\phi = 2\pi \frac{\Phi}{\Phi_0} = \frac{\Phi}{\phi_0}, \tag{2.3}$$

as the canonical coordinate, where $\Phi_0 = h/(2e)$ is the magnetic flux quantum and $\phi_0 = \Phi_0/(2\pi) = \hbar/(2e)$. We will identify ϕ as a phase shortly.

In terms of ϕ the inductive and capacitive energy of the LC circuit read,

$$\begin{aligned} \mathcal{E}_L &= \frac{1}{2} L I^2 = \frac{\phi_0^2}{2L}\phi^2, \\ \mathcal{E}_C &= \frac{1}{2} C V^2 = \frac{1}{2} C \phi_0^2 \dot{\phi}^2. \end{aligned} \tag{2.4}$$

The Lagrangian of the circuit reads,

$$\mathcal{L} = \mathcal{E}_C - \mathcal{E}_L = \frac{1}{2} C \phi_0^2 \dot{\phi}^2 - \frac{\phi_0^2}{2L}\phi^2. \tag{2.5}$$

This Lagrangian gives the equation of motion to be, $\ddot{\Phi} - (1/LC)\Phi = 0$, the solution of which is as expected a sinusoidal wave at frequency $1/\sqrt{LC}$. The Lagrangian also defines the conjugate momentum corresponding to ϕ to be,

$$\pi_\phi \equiv \frac{\partial \mathcal{L}}{\partial \dot{\phi}} = C\phi_0^2 \dot{\phi} = \phi_0 Q = \hbar n, \tag{2.6}$$

where we used $Q = C\dot{\Phi}$. n is the number of electron pairs on the capacitor. The fact that the conjugate of ϕ is the number validates the interpretation of ϕ as a phase. Eq. (2.6) also implies that Φ and Q are conjugate variables as well. The Hamiltonian is written as,

$$H = \pi_\phi \dot{\phi} - \mathcal{L} = \frac{\hbar^2}{2\phi_0^2 C} n^2 + \frac{\phi_0^2}{2L}\phi^2. \tag{2.7}$$

This is the Hamiltonian of a harmonic oscillator (with a mass $m = \phi_0^2 C$) which is quadratic in position (ϕ) and momentum ($\pi = \hbar n$). There are two energy scales for this harmonic oscillator: The kinetic energy scale is the charging energy $E_c = e^2/(2C)$ required to add one electron to the capacitor and the potential energy scale is $E_L = \phi_0^2/(2L)$. In terms of these energy scales the

Hamiltonian reads,

$$H = 4E_c n^2 + E_L \phi^2. \tag{2.8}$$

Note that here we take the phase to be the canonical coordinate and the number of charges to be the conjugate momentum. For a harmonic oscillator it is also possible to take the opposite choice [1]. However as we will see in the next section, for a Josephson junction which is a nonlinear element in phase, it is desirable to take the phase as position to work with a *nonlinear potential* rather than a *nonlinear kinetic energy.* To quantize the Hamiltonian, we can now define the phase and number operators respectively as $\hat{\phi}$ and $\hat{n}$. We drop the hat and use ϕ and n as operators and eigenvalues interchangeably unless there is an ambiguity. The canonical quantization of a harmonic oscillator requires that the two conjugate variables satisfy the canonical quantization relation $[\phi, \pi] = i\hbar$. Analogous to a harmonic oscillator, we define the creation and annihilation operators $(a^\dagger, a)$ for the LC circuit as follows,

$$\phi = \overline{\phi}(a + a^\dagger), \quad n = -i(2\overline{\phi})^{-1}(a - a^\dagger), \tag{2.9}$$

where $[a, a^\dagger] = 1$ and

$$\overline{\phi} = \sqrt[4]{\frac{E_c}{E_L}} = \sqrt{\frac{\hbar}{2\phi_0^2}\sqrt{\frac{L}{C}}}, \tag{2.10}$$

is the zero-point fluctuation of the phase operator. $\overline{\phi}$ characterizes the uncertainty of phase and number operators in the ground state of the circuit,

$$\sqrt{\langle 0|\phi^2|0\rangle} = \overline{\phi}, \quad \sqrt{\langle 0|n^2|0\rangle} = (2\overline{\phi})^{-1}. \tag{2.11}$$

The quantized Hamiltonian has the form,

$$H = \hbar\omega a^\dagger a, \tag{2.12}$$

with,

$$\omega = \sqrt{\frac{1}{LC}} = \frac{4}{\hbar}\sqrt{E_c E_L}. \tag{2.13}$$

We also define the characteristic impedance of the LC circuit as,

$$Z = \sqrt{\frac{L}{C}} = \frac{2\phi_0^2}{\hbar}\sqrt{\frac{E_c}{E_L}}. \tag{2.14}$$

The operator representation of other dynamical variables are written as follows,

$$\begin{aligned}
\Phi &= \phi_0\phi = \sqrt{\frac{\hbar Z}{2}}(a + a^\dagger), \\
Q &= \frac{\pi}{\phi_0} = 2en = -i\sqrt{\frac{\hbar}{2Z}}(a - a^\dagger), \\
V &= \frac{Q}{C} = \frac{-i}{C}\sqrt{\frac{\hbar}{2Z}}(a - a^\dagger), \\
I &= \frac{\Phi}{L} = \frac{1}{L}\sqrt{\frac{\hbar}{2Z}}(a + a^\dagger).
\end{aligned} \tag{2.15}$$

So far we considered an LC circuit with a single resonance. In general, a larger network composed of linear elements exhibits several resonances. These resonances are characterized by defining a *frequency dependent impedance* $Z(\omega)$ or *admittances* $Y(\omega)$. An in-depth discussion about impedances and admittances can be found in [1, 2]. It can be shown that the impedance and admittances of the network are represented by a number of LC circuits in series or in parallel, each of which is associated with a resonance mode of the network. This means that the very feature of an LC network is the equidistant energy levels of its modes. This feature hinders the applicability of an LC circuit (or network) as a qubit. According to the DiVincenzo criteria [4], the first requirement to use a physical system in quantum information processing is to define a two-level system, i.e. a qubit. In the next section we introduce the Josephson junction and show how this element circumvents the issue about LC networks.

2.3 Josephson junctions

The nonlinear element which makes superconducting circuits a suitable platform for quantum information processing is the Josephson junction [5, 6]. A Josephson Junction consists of two superconductors (e.g. aluminium) which are separated by an insulating layer (e.g. aluminium oxide). The ground state of the superconductor is a coherent condensate of electron pairs called Cooper pairs. Thanks to this fact, one can reduce the complexity associated with microscopic details of the many-body wavefunction of a superconductor and describe it in terms of the collective macroscopic state i.e. a single value wavefunction. In this macroscopic state the only important dynamical variable is the number of Cooper pairs N (i.e. charge $Q = -2eN$ or equivalently the coherent phase ϕ) and the state of the superconductor can be written in *charge basis* denoted by $|N\rangle$. Therefore the state of a Josephson junction with charge $Q_L = -2eN_L$ on the left superconductor and charge $Q_R = -2eN_R$ on the right superconductor is then written as $|N_L, N_R\rangle$. There are two energy scales associated with a Josephson junction: The **charging energy** $E_c = e^2/(2C_J)$ which is due to a capacitance C_J between the superconducting electrodes. E_c is the Coulomb energy required to transfer one electron from one side to the other side of the junction. The total contribution of the capacitive energy is written in an operator form as,

$$H_c = E_c \sum_{N_L,N_R} (N_L - N_R)^2 |N_L, N_R\rangle \langle N_L, N_R| \,. \tag{2.16}$$

The second energy scale is the **Josephson energy** E_J due to the tunneling of Cooper pairs through the junction. The tunneling Hamiltonian is written as,

$$H_T = -\frac{1}{2} E_J \sum_{N_L,N_R} |N_L, N_R\rangle \langle N_L - 1, N_R + 1| + |N_L, N_R\rangle \langle N_L + 1, N_R - 1| \,, \tag{2.17}$$

where the first term describes a process in which a Cooper pair tunnels from the left to right and the second term describes the opposite process. E_J is related to the parameters of the superconductor through the Ambegaokar-Baratoff formula [11],

$$E_J = \frac{1}{2} \frac{h}{(2e)^2} G_N \Delta, \tag{2.18}$$

where G_N is the normal state conductance and Δ is the superconducting gap. As both H_c and H_T are number-conserving, we can fix an arbitrary reference state $|N_{L0}, N_{R0}\rangle$ with $N_{L0} + N_{R0} = N$ where N is the total number of pairs.

In this case, any state $|N_L, N_R\rangle$ is uniquely given by the number of pairs n that should tunnel to the left from the reference state to reach $|N_L, N_R\rangle$, i.e. $|N_L, N_R\rangle \equiv |N_{L0} - n, N_{R0} + n\rangle$. Therefore $|N_L, N_R\rangle$ can be replaced by a simplified notation $|n\rangle$. We can now write the total Hamiltonian of the Josephson junction in terms of $|n\rangle$,

$$H = \sum_n 4E_c(n - n_g)^2 |n\rangle \langle n| - \frac{1}{2}E_J \sum_n |n + 1\rangle \langle n| + |n\rangle \langle n + 1|, \qquad (2.19)$$

where $n_g = (N_{L0} - N_{R0})/2$. Without loss of generality we take $N_{L0} = N_{R0}$, so $n_g = 0$.

Charge number states $|n\rangle$ are the eigenstates of the capacitive part of the Hamiltonian, i.e. in the absence of tunneling. We now define the Fourier transform of $|n\rangle$ as follows,

$$|\phi\rangle = \sum_{n=-\infty}^{\infty} e^{i\phi n} |n\rangle. \qquad (2.20)$$

It requires that ϕ is the conjugate variable to the number of tunnelled electrons n. We can thus identify ϕ as the phase drop over the junction and we call $|\phi\rangle$ a phase state. The definition of the phase state indicates that $|\phi + 2\pi\rangle$ and $|\phi\rangle$ are the same states since n is an integer number and therefore ϕ is defined modulo 2π. $|\phi\rangle$ is the eigenstate of the *phase operator*. To avoid any ambiguity with this periodic structure of phase, we define the phase operator as,

$$e^{i\hat{\phi}} |\phi\rangle = e^{i\phi} |\phi\rangle. \qquad (2.21)$$

Conversely charge states can be written in terms of phase states through inverse Fourier transform,

$$|n\rangle = \frac{1}{2\pi} \int_{-\infty}^{+\infty} d\phi . e^{-i\phi n} |\phi\rangle. \qquad (2.22)$$

One can easily verify that in term of charge states, the phase operator is expressed as,

$$e^{i\hat{\phi}} = \sum_{m=-\infty}^{\infty} |m\rangle \langle m + 1|. \qquad (2.23)$$

This means that ϕ is the generator of increments in charge state. Likewise, the charge operator is the generator of infinitesimal changes in phase,

$$e^{i\delta\phi\hat{n}} \left|\phi\right\rangle = \left|\phi + \delta\phi\right\rangle . \tag{2.24}$$

By expanding both sides to the linear order we arrive at the action of charge operator on phase states,

$$(1 + i\delta\phi\hat{n}) \left|\phi\right\rangle = \left|\phi\right\rangle + \partial_\phi \left|\phi\right\rangle \delta\phi \Rightarrow \hat{n} \left|\phi\right\rangle = -i\partial_\phi \left|\phi\right\rangle . \tag{2.25}$$

Using this representation, it is easy to show that phase and charge operators satisfy the following commutation relations,

$$\begin{aligned} [n, e^{i\phi}] &= -e^{i\phi}, \\ [n, e^{-i\phi}] &= e^{-i\phi}. \end{aligned} \tag{2.26}$$

The tunneling part of the Hamiltonian (2.19) is written as,

$$H_T = -\frac{E_J}{2}(e^{i\hat{\phi}} + e^{-i\hat{\phi}}) = -E_J \cos(\hat{\phi}). \tag{2.27}$$

Finally the Hamiltonian of a Josephson junction in a compact form reads,

$$H = 4E_c n^2 - E_J \cos(\phi). \tag{2.28}$$

2.3.1 Josephson equations and Josephson inductance

A current operator can be defined through the Heisenberg equation for the the charge number operator,

$$I = 2e\dot{n} = 2e\frac{i}{\hbar}[H, n] = \frac{E_J}{\phi_0} \sin\phi = I_c \sin\phi. \tag{2.29}$$

$I_c = E_J/\phi_0$ is the critical current of the junction which is the maximum supercurrent that could pass through the junction with Josephson energy E_J. Forcing higher currents through the junction necessarily results in breaking the Cooper pairs and the flow of normal current. As I is a nonlinear function of ϕ, the Josephson junction should behave as a nonlinear inductor, i.e. its inductance depends on the phase operating point. The inductance at specific point $\phi = \phi_f$ is given by linearizing the current at ϕ_f,

$$L_J(\phi_f) = \phi_0 \frac{\partial \phi}{\partial I}\Big|_{\phi=\phi_f} = \phi_0 \Big(\frac{\partial I}{\partial \phi}\Big|_{\phi=\phi_f}\Big)^{-1} = \frac{\phi_0}{I_c \cos(\phi_f)} = \frac{\phi_0^2}{E_J \cos(\phi_f)}. \quad (2.30)$$

In the case of small phase fluctuations around zero we have $\langle \phi \rangle = \langle I \rangle = 0$ and we get $L_{J0} = \phi_0^2/E_J$. For an arbitrary current mean value I, the Josephson inductor reads,

$$L_J = \frac{L_{J0}}{\sqrt{1 - (I/I_c)^2}}. \quad (2.31)$$

Let us now assume that an external voltage $V(t)$ is directly applied to the junction, the phase over the junction evolves as follows,

$$\dot{\Phi} = V(t) \Rightarrow \phi(t) = \phi(t=0) + \frac{1}{\phi_0}\int_0^t V(t')dt'. \quad (2.32)$$

In case of a dc voltage $V(t) = V_{dc}$, the phase over the junction reads,

$$\dot{\Phi} = V_{dc} \Rightarrow \phi(t) = \phi(t=0) + (V_{dc}/\phi_0)t. \quad (2.33)$$

Replacing this phase in Eq. (2.29) leads to,

$$I = I_c \sin(\phi(t=0) + \omega_J t), \quad (2.34)$$

which is an AC current with Josephson frequency $\omega_J = V_{dc}/\phi_0 = 2\pi \times 483.6 \times 10^{12} V_{dc}$ Hz. The two Eq. (2.29) and (2.34) are the two Josephson relations.

We now comment on typical experimental values for the parameters of a Josephson junction [13]. For an Al-AlOx-Al junction with an overlap of 100 nm by 100 nm the junction inductance and capacitance would be of the order of 10 nH and 1fF which leads to a self oscillation frequency of 50 GHz. To lower this frequency to the practical range for superconducting circuits one would need to increase the capacitive or inductive energies of the junction. Shunting the junction with a capacitance (e.g. 50 fF) or an inductance (e.g. 1.5 μH) would then be a straightforward solution. A transmon [14–16] is an

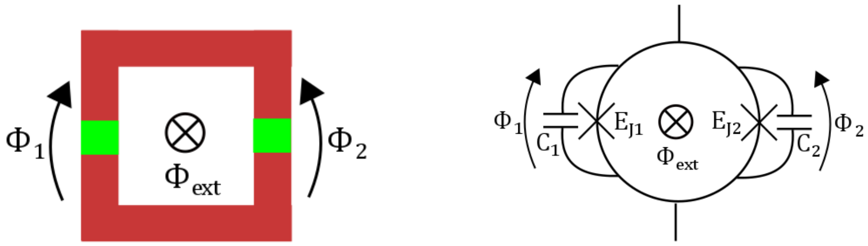

(a) (b)

Figure 2.2: **(a)** A dc-SQUID comprises two Josephson junctions in parallel and can be threaded by an external flux Φ_{ext}. **(b)** The circuit model of the dc-SQUID. In general, there is also an equivalent inductive element (linear) related to the loop, but we assume it is negligible.

example of the first case, i.e. a capacitively-shunted junction and a Fluxonium [17] is an example of the latter case, namely a junction which is shunted by a superinductor, see Sec. 2.4.

2.3.2 Tunable Josephson junction: dc-SQUID

A superconducting loop which contains one or more Josephson junctions is called a Superconducting QUantum Interference Device (SQUID). When the loop contains one junction, the device is called an rf-SQUID and in the case of two junctions it is called a dc-SQUID [18, 19]. Due to the high sensitivity of SQUIDs to an external flux through the superconducting loop, these devices have important applications in magnetic field measurement and sensing i.e. magnetometers. As we will show below, when the loop is threaded by an external flux the dc-SQUID can be seen as a tunable Josephson junction and therefore has wide applications in superconducting quantum circuits and qubits [21]. We consider a dc-SQUID as shown in Fig. 2.2. We assume that the phase drops over the two junctions are ϕ_1 an ϕ_2 and that Φ_{ext} is the external flux through the loop. The Fluxoid quantization constraint [20] requires that,

$$\phi_1 - \phi_2 + \phi_{ext} = 2\pi n, \quad n \in \text{integer}, \tag{2.35}$$

where $\phi_{ext} = \Phi_{ext}/\phi_0$. This constraint reduces the dynamical degrees of freedom from two to one. Motivated by this equation, we define the dynamical variable to be $\phi = (\phi_1 + \phi_2)/2$. The Lagrangian of the dc-SQUID reads,

$$\mathcal{L} = \frac{1}{2}C_1\phi_0\dot{\phi}_1^2 + \frac{1}{2}C_2\phi_0\dot{\phi}_2^2 + E_{J1}\cos(\phi_1) + E_{J2}\cos(\phi_2). \tag{2.36}$$

In terms of the dynamical variable ϕ this Lagrangian reduces to [1],

$$\begin{aligned}\mathcal{L} = \frac{1}{2}C_\Sigma\phi_0^2\dot{\phi}^2 &+ (E_{J1} + E_{J2})\cos(\frac{\phi_{ext}}{2})\cos(\phi)\\ &+ (E_{J1} - E_{J2})\sin(\frac{\phi_{ext}}{2})\sin(\phi),\end{aligned} \tag{2.37}$$

where $C_\Sigma = C_1 + C_2$. This Lagrangian leads to the following Hamiltonian,

$$H = 4E_c n^2 - E_J(\phi_{ext})\cos(\phi + \phi_s), \tag{2.38}$$

where the charging energy E_c, effective Josephson energy $E_J(\phi_{ext})$ and phase shift ϕ_s are defined as follows,

$$\begin{aligned}E_c &= \frac{e^2}{2C_\Sigma},\\ E_J(\phi_{ext}) &= \sqrt{E_{J1}^2 + E_{J2}^2 + 2E_{J1}E_{J2}\cos\phi_{ext}},\\ \phi_s &= \arctan\left(\tan(\phi_{ext/2})\frac{E_{J2} - E_{J1}}{E_{J2} + E_{J1}}\right).\end{aligned} \tag{2.39}$$

If ϕ_s is time independent, it gives a constant phase shift and can be absorbed into the definition of ϕ. In the case of a symmetric SQUID, i.e. $E_J = E_{J1} = E_{J2}$ and $C_1 = C_2$ the Hamiltonian reads,

$$H = 4E_c n^2 - 2E_J\cos(\frac{\phi_{ext}}{2})\cos(\phi), \tag{2.40}$$

which has the form of the Hamiltonian of a junction with tunable Josephson energy $E_{J,eff} = 2E_J\cos(\phi_{ext}/2)$.

---

[1] This form of the Lagrangian holds only when $C_1 = C_2$ or ϕ_{ext} is time-independent. Otherwise there is an additional term proportional to $\dot{\phi}_{ext}\phi$, but we are not interested in that term.

2.4 Superconducting qubits

After an introduction to the physics of Josephson junctions, we are ready to discuss how a Josephson junction can be used as a circuit element to define various types of qubits in this section [25, 26]. In principle, there are three basic configurations to bias a Josephson junction in a circuit: charge bias, flux bias and current bias. Accordingly, the three basic types of qubits that can be identified in these circuits are named charge qubit, flux qubit and phase qubit [22–24]. These configurations and their corresponding potential energy are shown in Fig. 2.3. The equivalent circuit for all of these configurations has a Josephson junction in parallel with a capacitor C_Σ and an inductor L, see Fig. 2.4. Note that all these circuits have one degree of freedom e.g. phase of the junction (hence a single qubit), and C_Σ and L are the total capacitance and inductance seen from the junction. For each of theses circuits there are three characteristic energies : Josephson energy (E_J), capacitive energy ($E_c = e^2/C_\Sigma$) and inductive energy ($E_L = \phi_0^2/(2L)$). The competition between Josephson energy and capacitive energy distinguishes two operational regimes in a circuit. Charge regime when $E_c \gg E_J$ which is relevant for charge biasing and phase regime $E_J \gg E_c$ for flux and current biasing. Moreover the ratio between the Josephson and inductive energies differentiates the flux and current biased circuits.

In the **charge biased scheme** the junction is coupled to a voltage source capacitively, See Fig. 2.3a. This architecture is also called a Cooper Pair Box (CPB). CPB has no excess inductive energy ($L \to \infty$) and its potential comes from the Josephson junction,

$$U(\phi) = -E_J \cos(\phi). \tag{2.41}$$

On the other hand, the kinetic energy of a CPB is modified with respect to a Josephson junction as follows (1) The charging energy is determined by the total capacitance C_Σ and (2) The voltage source induces a charge offset (or a displacement in momentum space). The CPB typically operates in the charging regime characterized by large capacitive energy. In this limit one can

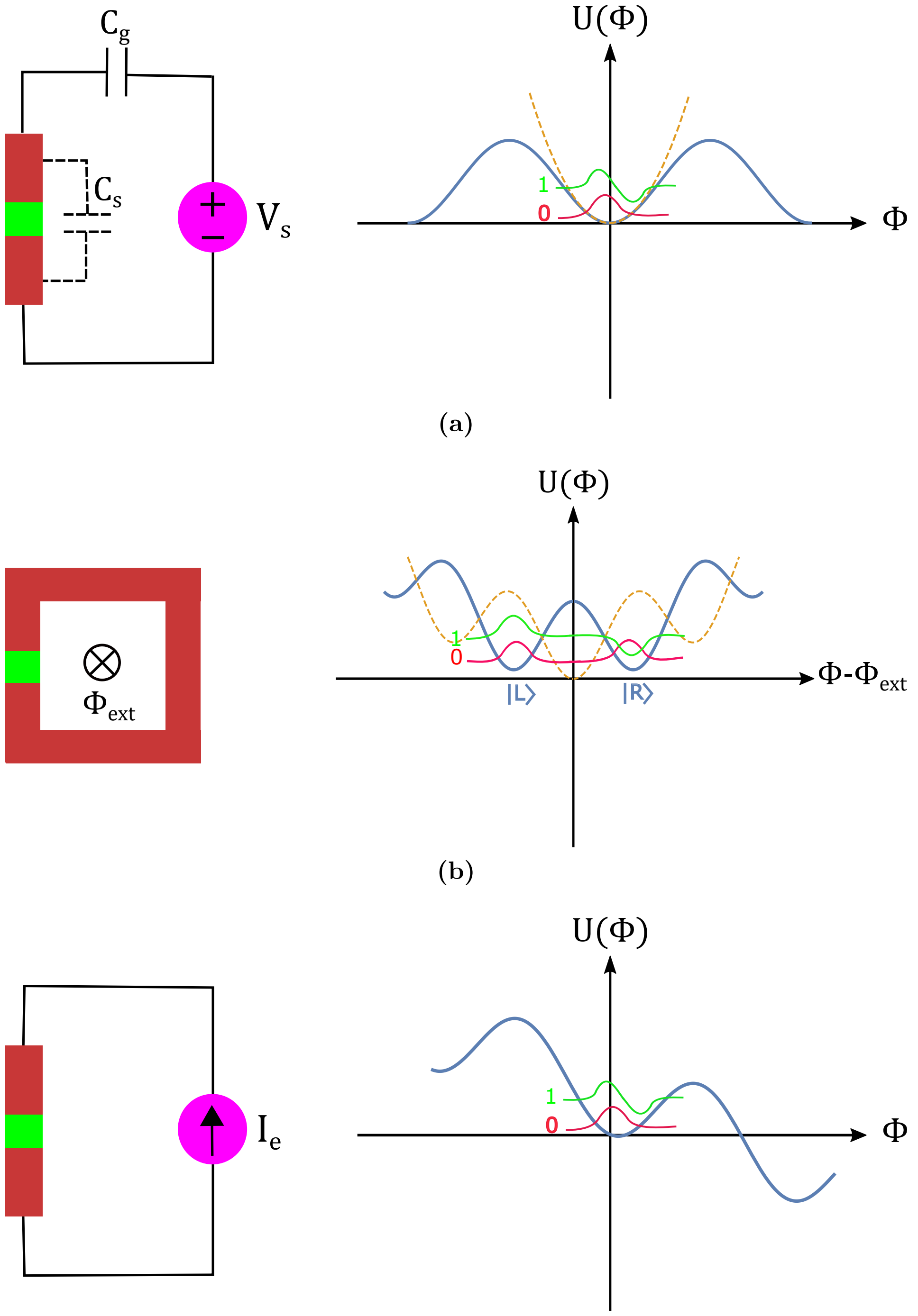

(a)

(b)

(c)

Figure 2.3: Basic biasing circuits for a Josephson junction and their corresponding potentials. The lowest two (local) eigenstates are shown in red and green. **a)** Charge-biased Josephson junction and its potential. The dashed line shows the linear harmonic potential. **b)** Flux-biased rf-SQUID and its potential when external flux has integer (dashed) or half-integer (solid) number of flux quanta. **c)** Current-biased Josephson junction and the *washboard* potential.

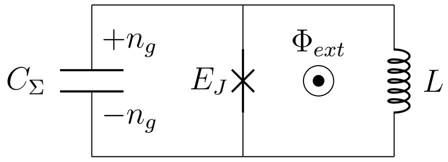

Figure 2.4: Equivalent circuit for all biasing schemes. L is the inductance of the superconducting loop in the flux and current biased circuits. In these circuits Φ_{ext} is used as a control "knob". For the charge biased circuit $L \to \infty$ and the induced charge n_g is the "knob" [26].

define a charge qubit from the charge states $|n = 0\rangle$ and $|n = 1\rangle$. The downside of a charge qubit is that it is vulnerable to charge noise. To alleviate this issue, the Josephson junction of CPB can be shunted by a capacitance C_s to reduce the charging energy of the circuit. For $E_J \sim E_c$, it is called a Quantronium [27]. A CPB with operates in a regime with $E_J \gg E_c$ is called a *transmon qubit*. In this work, we mainly work with transmon qubits and we analyse the CPB and transmon thoroughly in Sec. 2.4.1.

In the **flux-biased scheme**, an rf-SQUID is threaded by an external magnetic flux. The external flux in this case acts as a "knob" and similar to the role of a voltage source in charge biasing, it shifts the phase operator (or the position operator). The potential for the flux-biased circuit reads,

$$U(\phi) = -E_J \cos(\phi) + \frac{E_L}{2}(\phi - \phi_{ext})^2, \quad \phi_{ext} = \frac{\Phi_{ext}}{\phi_0}, \tag{2.42}$$

which has the shape of a parabola modulated by a cosine function. The potential in this case has a single minimum at $\phi_{ext} = n$ and two degenerate minima for $\phi_{ext} = n+1/2$, i.e. when the external flux has integer and half integer number of quantum flux Φ_0 respectively. A *flux qubit* [28] is defined for half-integer biasing when $E_J \gg E_c$. In the absence of tunneling between the wells, the (degenerate) ground state of the individual wells are the left and right circulating currents $|L\rangle$ and $|R\rangle$. The finite tunneling mixes these states and forms a tight two-level system, i.e. the lowest two levels of the double-well are the symmetric and anti-symmetric superpositions of $|L\rangle$ and $|R\rangle$. The level splitting of this two-level system is set by the tunneling rate while level spacing in individual wells is determined by the Josephson energy. Thus for large Josephson energy and comparably small tunneling rate, the two-level system can be used as a qubit. The realization of the double-well potential requires that the inductive energy of the superconducting loop E_L is of the order of Josephson energy E_J. In practice, it is more convenient to use a three-junction SQUID to boost the required inductive energy for the flux qubits [10, 29, 30].

A **current-biased junction** is shown in Fig. 2.3c. Here, a washboard potential profile is constructed by applying a current source to the junction,

$$U(\phi) = -E_J \cos(\phi) + I_e \phi. \tag{2.43}$$

A *phase qubit* [31, 32] can be defined from the lowest two states of a local minimum in $U(\phi)$. In a flux-driven rf-SQUID, the double-well potential is non-symmetric for $\phi_{ext} \neq 0.5$ and the system behaves as a phase qubit. Therefore flux and current biased schemes can be realized in an rf-SQUID circuit. The ratio E_J/E_c is typically higher for phase qubits while the ratio E_L/E_J is higher for flux qubits.

To improve the functionality of a qubit and taking advantage of opposite regimes, there are several qubits designed to operate in an intermediate regime. Quantronium and transmon qubits introduced earlier are of this kind. In the Fluxonium qubit, the junction is shunted by a very large effective inductor. The effective inductor is constructed from a series of Josephson junctions [17]. This architecture inherits features from both flux qubit and charge qubit. On the one hand, it is similar to the 3 junction flux-qubit when two junctions are replaced by many junctions. On the other hand, $E_J \sim E_c$ as in the case of Quantronium so the circuit does not operate in the phase regime. The charge fluctuation is also very small in this circuit as a result of a tiny capacitance. The C-shunt flux qubit [33–35] is a three junction flux qubit, shunted by a large capacitance. It can also be seen as a transmon with added inductive energy. As opposed to a flux qubit, the C-shut qubit has a single well potential yet compared to a transmon the potential well is flattened and has a larger nonlinearity. There are also a number of variants of the transmon qubit, e.g. Xmon and gmon are qubits from transmon family adapted for 2D structures [36–38]. In table 2.1, different qubits are classified according to their operating regime.

	E_L/E_J		
E_J/E_c	0	$\ll 1$	$\sim 0.3 - 0.5$
$\ll 1$	CPB		
~ 1	Quantronium	Fluxonium	
$\gg 1$	transmon		flux qubit, C-shunt
$\ggg 1$		phase qubit	

Table 2.1: The operating regimes of various qubits.

2.4.1 From Cooper pair box (CPB) to transmon

The first superconducting architecture that manifested a mesoscopic circuit could behave as an artificial two level atom was the Cooper Pair Box (CPB)[7, 8]. The theoretical description of a CPB is given in [9]. It consists of a Josephson junction which is connected to a voltage source V_s via a gate capacitance C_g, see Fig. 2.3a. This circuit has a single dynamical degree of freedom which we take to be the phase drop over the Josephson junction, denoted by $\phi = \Phi/\phi_0$. The voltage drop over the gate capacitance is $V_g = V_s - \dot{\Phi}$. The Lagrangian of the circuit reads,

$$\mathcal{L} = \frac{1}{2}C_J\phi_0^2\dot{\phi}^2 + \frac{1}{2}C_g(V_s - \phi_0\dot{\phi})^2 - E_J\cos(\phi), \tag{2.44}$$

which gives the conjugate momentum of ϕ,

$$\pi_\phi = \frac{\partial}{\partial\dot{\phi}}\mathcal{L} = C_\Sigma\phi_0^2\dot{\phi} - C_g\phi_0^2V_s = \phi_0 Q = \hbar n, \tag{2.45}$$

with $C_\Sigma = C_g + C_J$. Here Q is the net charge seen from the Josephson junction and n has the meaning of the number of Cooper pairs on the superconducting island connected to the gate capacitor. The Hamiltonian up to a constant term reads,

$$H = \pi_\phi\dot{\phi} - \mathcal{L} = 4E_c(n - n_g)^2 - E_J\cos(\phi), \tag{2.46}$$

where $E_c = \hbar^2/(8\phi_0^2 C_\Sigma) = e^2/(2C_\Sigma)$ is the charging energy of the circuit and $n_g = -\phi_0 C_g V_s$. $Q_g = 2en_g$ is the charge offset induced by the external voltage source. The ratio between the energy scales of the CPB defines two opposite operational limits: a charging regime for $E_c \gg E_J$ and a transmon regime for $E_c \ll E_J$. In the following, we show how to use the CPB as a qubit in each of these regimes.

Charging regime

Charge states $|n\rangle$ are the eigenstates of the capacitive part of the CPB Hamiltonian, in the absence of Josephson tunneling, the Hamiltonian of CPB is diagonal in charge basis with energies,

$$H_{CPB}(E_J \to 0)\,|n\rangle = 4E_c(n-n_g)^2\,|n\rangle\,. \tag{2.47}$$

There are specific values for the gate voltage (or equivalently n_g) for which the eigenenergies become degenerate, see Fig. 2.5. Let us take the two states $|n=0\rangle$ and $|n=1\rangle$. These states are degenerate at $n_g = 0.5$ with energies E_c. By switching on the Josephson energy, the degeneracy is lifted and turns into a two-level system. This two-level system has tiny admixture of other charge states since $E_c \ll E_J$. We can thus truncate the full Hamiltonian to states $|0\rangle$ and $|1\rangle$ and use the two-level system as a charge qubit. The Hamiltonian in the truncated basis reads,

$$H = \begin{pmatrix} 4E_c(1-n_g)^2 & -E_J \\ -E_J & 4E_c n_g^2, \end{pmatrix} \tag{2.48}$$

with eigenenergies $\epsilon = \pm\sqrt{E_c(1-2n_g)^2 + E_J^2/4}$.

Approximate solution for transmon regime

A CPB with $E_J \gg E_c$ operates in the transmon regime. By virtue of Eq. (2.10), we expect that the phase fluctuation is small in this regime. Thus we expand the cosine term in the Hamiltonian to the fourth order, $\cos(\phi) =$

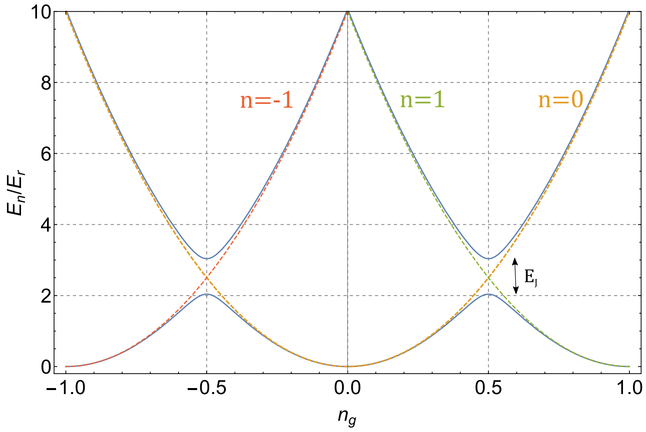

Figure 2.5: Eigenenergies of a CPB in the charging regime for $E_J/(4E_c) = 0.1$ (solid) and $E_J = 0$ (dashed). $E_r \approx E_J$ is the difference between the two lowest eigenvalues at $n_g = 0.5$.

$1 - \frac{1}{2!}\phi^2 + \frac{1}{4!}\phi^4 + O(\phi^6)$. The CPB Hamiltonian thus reads,

$$H_{CPB} \approx 4E_c(n - n_g)^2 + \frac{E_J}{2!}\phi^2 - \frac{E_J}{4!}\phi^4. \tag{2.49}$$

Let us first consider a case with $n_g = 0$. The quadratic terms of this Hamiltonian form a harmonic oscillator, while the quartic term adds a small nonlinearity on top of the harmonic oscillator since $\sqrt{\langle\phi^2\rangle} \ll 1$. The CPB in this regime is thus described by a *nonlinear harmonic oscillator* and the eigenstates of the harmonic oscillator should be suitable basis for a perturbation theory. In this case, the unperturbed harmonic oscillator frequency and zero-point fluctuation read,

$$\omega_0 = \frac{1}{\hbar}\sqrt{8E_J E_c}, \quad \overline{\phi} = (\frac{2E_C}{E_J})^{1/4}. \tag{2.50}$$

The nonlinear part is quantized using the ladder operators introduced for a harmonic oscillator, c.f. Eq. (2.9),

$$\frac{E_J}{4!}\phi^4 = \frac{E_J}{4!}\overline{\phi}^4(a + a^\dagger)^4 \to E_c a^\dagger a + \frac{E_c}{2}a^\dagger a^\dagger a a, \tag{2.51}$$

where we also discarded the terms which are not number-conserving. The quantized CPB Hamiltonian then reads,

$$H_{CPB} = \hbar\omega a^\dagger a - \frac{E_c}{2} a^\dagger a^\dagger a a, \tag{2.52}$$

with $\hbar\omega = \sqrt{8E_J E_c} - E_c$. The n^{th} eigenvalue of the CPB to the fourth order in ϕ is,

$$E_n = \langle n|H_{CPB}|n\rangle = \hbar n\omega - \frac{E_c}{2}(n^2 - n). \tag{2.53}$$

If $E_{n,n+1}$ is the transition energy between adjacent levels then $E_{0,1} = \hbar\omega$ and $E_{1,2} = \hbar\omega - E_c$. Therefore E_c is the nonlinearity of the CPB and the ratio of the nonlinearity to the transition frequency of the harmonic oscillator is $\sqrt{E_c/(8E_J)}$. The nonlinearity thus decreases by increasing the ratio E_J/E_c. Physically speaking, the particle swinging at the bottom of the potential well gets more and more localized in the well as this ratio increases and thus becomes more insensitive to the true shape of the cosine potential compared to a harmonic potential. This means that the particle feels less nonlinearity. Nevertheless, as far as the nonlinearity E_c is the largest energy scale compared to other *interaction* energy scale in a system, one can truncate the Hamiltonian to the lowest two states to define a transmon qubit,

$$H_{CPB} = \hbar\omega\sigma^+\sigma^-. \tag{2.54}$$

On the other hand, a particle which is localized in the phase space becomes completely delocalized in the charge space. It means that the transmon qubit is insensitive to the charge noise of the gate capacitance. We will see in the next section, the effect of excess charge n_g translates into a *twisted boundary condition*. Therefore the effect of n_g only enters through the event of a 2π rotation in the phase space in which the particle picks a n_g-dependent phase [14]. Insensitivity of the transmon to the charge noise can then be seen from the fact that in transmon regime, the particle cannot tunnel to another well of the cosine potential, i.e. does not make a full 2π rotation, so n_g can be gauged away for a single well.

Exact solutions for the CPB

We now start from the stationary Schrödinger equation for a CPB, $H\left|\psi_k\right\rangle = E_k\left|\psi_k\right\rangle$ where k labels the eigenstates and eigenenergies. To solve the Schrödinger equation, we represent the states in the phase basis $|\phi\rangle$ and denote the wavefunction by $\psi_k(\phi) = \langle\phi|\psi_k\rangle$. The Schrödinger is written in this basis as,

$$\left\{4E_c(-i\frac{\partial}{\partial\phi} - n_g)^2 - E_J\cos(\phi)\right\}\psi_k(\phi) = E_k\psi_k(\phi), \tag{2.55}$$

with periodic boundary condition $\psi(\phi + 2\pi) = \psi(\phi)$. In terms of a new wavefunction $\tilde{\psi}_k(\phi) = e^{in_g\phi}\psi_k(\phi)$, the explicit n_g-dependence is removed,

$$\left\{-4E_c\frac{\partial}{\partial\phi^2} - E_J\cos(\phi)\right\}\tilde{\psi}_k(\phi) = E_k\tilde{\psi}_k(\phi). \tag{2.56}$$

The function $\tilde{\psi}_k(\phi)$ satisfies a *twisted boundary condition*, $\tilde{\psi}_k(\phi+2\pi) = e^{in_g2\pi}\tilde{\psi}_k(\phi)$. This equation now has the form of a *Mathieu equation* [57, 58],

$$y''(z) + (a - 2q\cos(2z))y(z) = 0, \tag{2.57}$$

with $2z \equiv \phi$ as function variable and parameters $a \equiv E_k/E_c$ and $q \equiv -E_J/(2E_c)$. a is the characteristic value (eigenvalue) of the Mathieu equation. The solutions to Mathieu equation are even and odd functions $\mathcal{M}_C(a, q, z)$ and $\mathcal{M}_S(a, q, z)$. For $q = 0$ we have, $\mathcal{M}_C(a, q, z) = \cos(\sqrt{a}z)$ and $\mathcal{M}_S(a, q, z) = \sin(\sqrt{a}z)$. For a generic q Floquet theory states that these functions can be written as follows,

$$\begin{aligned} \mathcal{M}_S &= e^{-irz}ms(z), \\ \mathcal{M}_C &= e^{-irz}mc(z), \end{aligned} \tag{2.58}$$

where $r \equiv r(a, q)$ is called the characteristic exponent and $mc(z)$ and $ms(z)$ are π-periodic functions. Note that for integer or rational r, $\mathcal{M}_C$ and $\mathcal{M}_S$ are periodic.[2] The characteristic value a for these cases are denoted by $a = \mathcal{M}_A(r, q)$ for even solutions and by $a \equiv \mathcal{M}_B(r, q)$ for the odd solutions. For

---

[2] For integer r the even and odd solution are denoted by $ce_r(q, z)$ and $se_r(q, z)$.

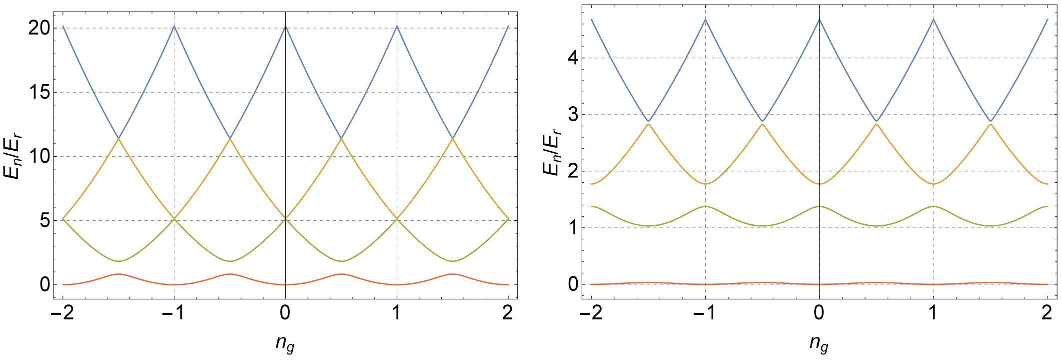

(a) $E_J/E_c = 0.2$ **(b)** $E_J/E_c = 1$

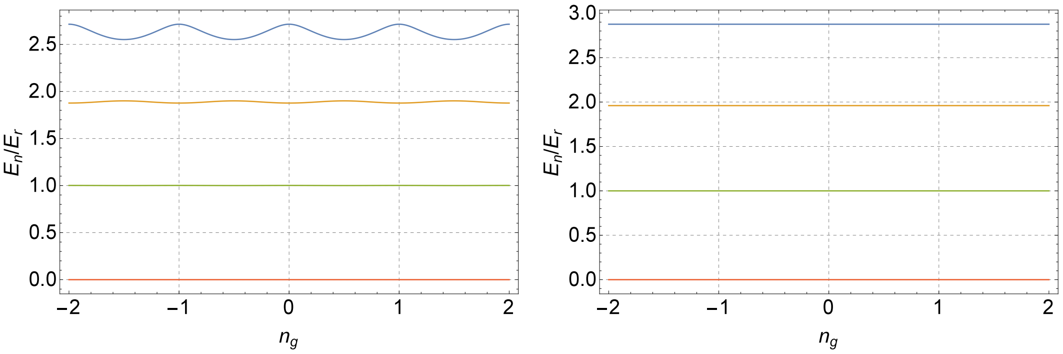

(c) $E_J/E_c = 5$ **(d)** $E_J/E_c = 25$

Figure 2.6: The lowest four eigenvalues of a CPB as a function of gate charge n_g for several values of the ratio E_J/E_c. As this ratio increases, the eigenvalues become insensitive to the gate charge. E_r is the difference between the two lowest eigenvalues at $n_g = 0.5$.

non-integer r (as is the case here), we have $\mathcal{M}_A(r,q) = \mathcal{M}_B(r,q)$. The solutions to the Schrödinger equation then read [12],

$$\psi_k(\phi) = \frac{e^{-in_g\phi}}{\sqrt{2\pi}}\left[\mathcal{M}_C\left(\frac{E_k}{E_c}, -\frac{E_J}{2E_c}, \phi\right) + i(-1)^{k+1}\mathcal{M}_S\left(\frac{E_k}{E_c}, -\frac{E_J}{2E_c}, \phi\right)\right]. \tag{2.59}$$

E_k is the eigenenergy corresponding to $\psi_k(\phi)$ which explicitly reads,

$$E_k = E_c\mathcal{M}_A(r_k, -\frac{E_J}{2E_c}) \text{ with } r_k = k + 1 - (k+1)[\text{mod}2] + 2n_g(-1)^k, \tag{2.60}$$

where r_k is the ordering parameter and is defined such that E_k increase with k [12]. The band dispersion d_k is defined as energy difference between the maximum (at $n_g = 0$) and minimum (at $n_g = 0.5$) in the k^{th} band [14],

$$\begin{aligned} d_k &= E_k(n_g = 0) - E_k(n_g = 0.5) \\ &\approx (-1)^k\sqrt{\frac{2}{\pi}}E_C\frac{2^{(4k+5)}}{k!}\left(\frac{E_J}{2E_c}\right)^{k/2+3/4}\exp\big(-\sqrt{8E_J/E_c}\big). \end{aligned} \tag{2.61}$$

The key feature is that the dispersion is suppressed *exponentially* in E_J/E_C, while as we discussed in the last section the nonlinearity decreases *algebraically* in E_J/E_C. The eigenenergies of the CPB can also be solved for numerically by expressing the Hamiltonian in charge basis and using $\cos(\phi) = \sum_m |m\rangle\langle m+1| + |m+1\rangle\langle m|$. The lowest four eigenenergies are shown in Fig. 2.6 for different ratios of E_J/E_C.

2.5 Circuit Quantum Electrodynamics (cQED)

In the previous sections, we introduced the basic building blocks of a superconducting circuit, namely resonators, superconducting qubits, dc-SQUIDs, etc.. From here on, we consider simple circuits composed of multiple blocks with practical applications. In this section, we discuss that a cavity QED system can be realized in microwave domain with superconducting circuits.

Cavity quantum electrodynamics (cavity QED) is the framework to study the phenomena related to the electromagnetic interaction between atoms enclosed in a cavity and the cavity mode(s) [40, 44]. In cavity QED, the cavity mode is modelled by a harmonic oscillator and the physics of a two-level atom coupled to a single cavity mode is captured by the Jaynes-Cummings Hamiltonian [39],

$$H^{JC} = \hbar\omega_c a^\dagger a + \frac{\hbar\omega_a}{2}\sigma^z + \hbar g(a\sigma^+ + a^\dagger\sigma^-), \tag{2.62}$$

where ω_c is the cavity mode frequency and ω_a is the transition frequency of the atom. The last term in the Hamiltonian is the coherent dipole interaction between the cavity and the atom (under a Rotating Wave Approximation where $a^\dagger\sigma^+ + \text{H.c.}$ can be discarded.[3]) and g is the strength of the dipole interaction. H^{JC} describes the coherent part of the atom-cavity interaction. In a realistic physical system, there are incoherent processes such as decay of cavity photons at rate κ due to imperfect cavity mirrors and decay of atom into other atomic states at rate γ, see Fig. 2.7a. In a cavity QED system [4], if $|g| \gg |\Delta| = |\omega_c - \omega_a|$, the cavity and atom are resonant and exchange excitations through Rabi oscillations. In the opposite limit where $|\Delta| = |\omega_c - \omega_a| \gg |g|$, there is no direct interaction between the atom and the resonator. This is the so-called *dispersive regime* of cavity QED. In this regime there is no substantial mixing between the atomic and photonic states and the two modes preserve their individual character, nonetheless depending on the ratio g/Δ, each mode is slightly dressed by the second mode. The phase diagram of a typical cavity QED system is given in Fig. 2.7b.

By placing a transmon qubit inside a coplanar waveguide (CPW) transmission line resonator, a circuit analogue of cavity QED can be implemented in the microwave regime [41]. The CPW hosts a standing wave between its ending nodes, the fundamental frequency ω_r of which is determined by the length of the CPW. The CPW is then readily described in terms of a harmonic oscillator (or a photon bus) [1] and plays the role of the cavity in cavity QED. This standing wave of the CPW induces a voltage difference between the islands of the transmon which gives rise to an effective dipole coupling. In principle, higher harmonics of the fundamental frequency can be formed

---

[3] The exact model which includes the rotating terms is known as Rabi model.

[4] We only talk abou strong coupling regime, where $|g|, |\Delta| \gg \kappa, \gamma$.

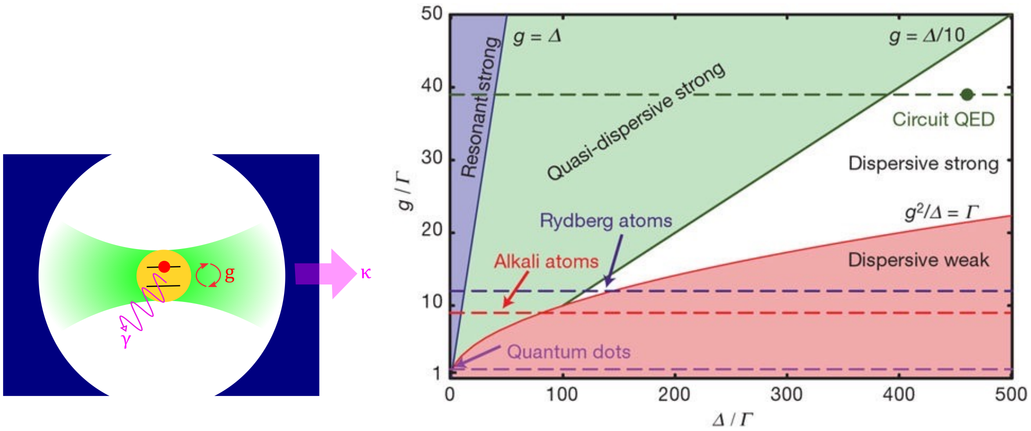

(a) (b)

Figure 2.7: **a)** Illustration of a simple cavity QED system. The atom and the cavity modes interact at rate g. The decay rates for atom and cavity are γ and κ respectively. **b)** Phase diagram of Jaynes-Cummings model with $\Gamma = \max\{\gamma, \kappa\}$ [43]. In the blue part the two modes are resonant. In the green part, the modes are off-resonance however each mode is dressed by more than 0.01 of the other mode. In the white part, the dressing is less than 0.01. In the red area, the linewidth is too large to distinguish single photons in the cavity.

inside CPW, however when the transition of the transmon is tuned close to the fundamental frequency, the CPW can be well approximated by a single harmonic oscillator. To derive the Hamiltonian of this circuit, we note that it has the same configuration as a Cooper pair box (with gate capacitance C_g and junction/shunt capacitance C_J) except that here the voltage is not induced by a classical voltage source as in the case of Cooper pair box but by a *quantum* voltage source, i.e. the harmonic oscillator. Therefore the residual charge $n_g = -\phi_0 C_g V_s$ in this system is a quantum variable and the Hamiltonian of the a circuit QED setup is given by replacing $V_s \to \hat{V}_s = V_{s0} + \delta\hat{V}_s$ in the Hamiltonian of a CPB, c.f. Eq. (2.46), where V_{s0} is a constant dc part and $\delta\hat{V}_s$ is the voltage operator of a harmonic oscillator, c.f. Eq. (2.15).

$$H = 4E_c(n - n_{g0})^2 - E_J\cos(\phi) + \hbar\omega_r a_r^\dagger a_r + 2e\beta V_{zpf} n(a_r - a_r^\dagger), \tag{2.63}$$

where $n_{g0} = -\phi_0 C_g V_{s0}$ and $\beta = C_g/(C_g+C_J)$. V_{zpf} is the zero point fluctuation

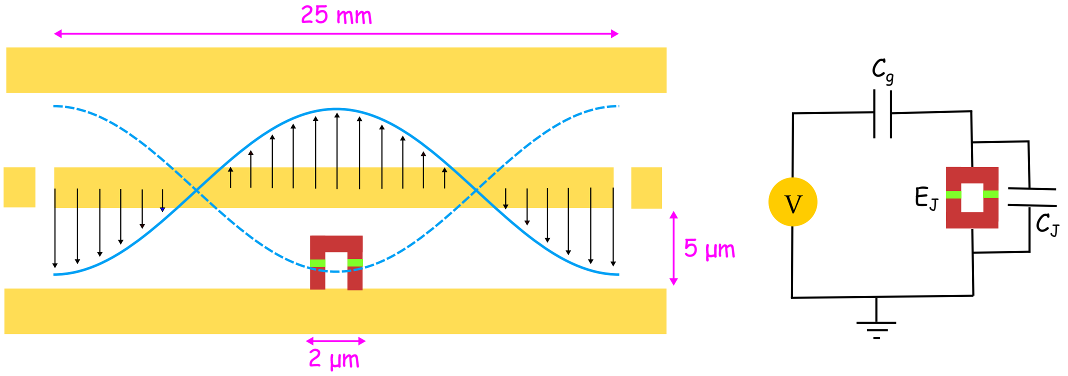

Figure 2.8: Left Architecture for circuit quantum electrodynamics. A transmon qubit is placed inside a coplanar waveguide (CPW) resonator where the standing wave of the CPW couples it to the transmon. **Right** The system is modelled by a quantum voltage source (i.e. the CPW) coupled capacitively to the transmon and described by the Jaynes-Cummings Hamiltonian (2.62).

of the voltage which in terms of the CPW capacitance and impedance reads,

$$V_{zpf} = \frac{-i}{C_r}\sqrt{\frac{\hbar}{2Z_r}}. \tag{2.64}$$

Now if the CPB operates in the transmon regime, the first two terms in this Hamiltonian describe a transmon qubit with $H_q = \hbar\omega_q\sigma^+\sigma^-$. In the last term, we express n in terms of qubit ladder operators (c.f. Eq. (2.9)) which leads to the cavity QED Hamiltonian (2.62) with interaction strength g between the qubit and the cavity mode as,

$$\hbar g = e\beta V_{zpf}(\frac{E_J}{2E_c})^{1/4}. \tag{2.65}$$

There are several interesting features about coupling a transmon to a CPW [42]. First, compared to other cavity QED systems, stronger couplings can be realized in circuit QED and regimes of cavity QED that are inaccessible in other implementations can be explored in circuit QED[43]. In particular, with circuit QED, it is possible to reach the so-called *ultrastrong coupling* regime where the coupling is of the order of transition frequencies of individual modes [55]. In this regime, the RWA no longer holds and the counter-rotating terms in the coupling should also be included in the model (i.e. Rabi model).

Another feature of circuit QED is that the cavity inhibits the coupling of the transmon to a continuum of spurious modes. This coupling is the cause of spontaneous emission and therefore in the dispersive limit the presence of cavity enhances the qubit lifetime through Purcell effect [47, 48]. Moreover, in circuit QED, the photon bus provides a way to manipulate and read-out qubits. By applying a microwave drive to the photon bus which is in resonance with a qubit, the qubit undergoes Rabi oscillations and single-qubit x and y rotations can be implemented [52, 53]. On the other hand, an off-resonant pulse would implement a z rotation through a Stark shift. A second approach for a z gate is to use the transmon flux to tune the qubit frequency. For a detailed discussion about single-qubit rotations the reader is referred to [51, 54]. In the dispersive regime of circuit QED, where $\Delta = |\omega_r - \omega_q| \gg |g|$, the qubit and the resonator do not exchange excitations. Nevertheless through virtual second-order processes the coupling gives rise to a frequency shift of the photonic mode conditional on the qubit state [14, 41],

$$H = \hbar(\omega_c + \sigma^z)a^\dagger a + \hbar(\omega_q + \frac{g^2}{\Delta})\frac{\sigma^z}{2}, \tag{2.66}$$

where $\Delta = \omega_r - \omega_q$. This conditional frequency shift is used to perform quantum non-demolition readout of the qubit state through transmission measurement on the CPW, see Sec. 2.7 [45, 46]. In this regime, virtual excitations also make it feasible to achieve qubit-qubit interaction when two or multiple transmons are placed inside the CPW [49–51]. We will come to this point when we discuss schemes for qubit-qubit interaction in Sec. 2.6.

2.6 Coupling schemes for transmon qubits

Any superconducting quantum computer or simulator necessarily includes several qubits and the first step to build a multi-qubit system is to develop architectures for qubit-qubit couplings. In this section we discuss common strategies for couplings between two transmon qubits [26]. Here subscripts 1 and 2 refer to the variables of the two qubits.

Direct capacitive coupling Two transmon qubits can be coupled directly via a capacitance (Fig. 2.9a). The coupling capacitance C_g contributes an additional term $C_g(\dot{\phi}_1 - \dot{\phi}_2)^2/2$ to the Lagrangian which gives rise to an interaction $n_1 n_2$ (or $\sigma_1^y \sigma_2^y$). The explicit form of the two-qubit Hamiltonian reads,

$$H = \hbar\omega_1 \sigma_1^z + \hbar\omega_2 \sigma_2^z + g_c \sigma_1^y \sigma_2^y, \tag{2.67}$$

where for $C_g \ll C_1, C_2$ the coupling strength is $g_c \approx e^2 C_g/(C_1 C_2 \overline{\phi}_1 \overline{\phi}_2)$.

Resonator coupling In Sec. 2.5, we discussed that the interaction between a transmon and a resonator (CPW) is described by the the Janeys-Cummings Hamiltonian. If two transmons are coupled through a common resonator, in the dispersive limit of JC model, the resonator mediates transmon-transmon interaction [56], see Fig. 2.9b. In this regime the resonator remains in the ground state and second-order perturbation theory leads to an effective interaction $g\sigma_1^+\sigma_2^- + \mathrm{H.c.}$ with,

$$g = g_1 g_2 \left(\frac{1}{\Delta_1} + \frac{1}{\Delta_2}\right), \tag{2.68}$$

where g_i is the coupling of each transmon to the CPW and $\Delta_i = \omega_r - \omega_{qi}$ is the detuning between the transmon and the CPW resonator [49]. When the transmons are tuned in resonance with each other, they swap excitations. On the other hand, when the transmons are detuned from each other, second-order perturbation on the swap Hamiltonian leads to an effective $g'\sigma_1^z\sigma_2^z$ interaction which is fourth-order in g_i,

$$g' = \frac{g_1^2 g_2^2}{\Delta_1^2 \Delta_2^2}(\Delta_1 + \Delta_2). \tag{2.69}$$

One can switch between the resonant and off-resonant regimes by changing the transition frequency of the transmons using the same approaches we mentioned earlier to perform z rotations. By letting different interactions operate for certain times, various types of two-qubit gates can be implemented [51].

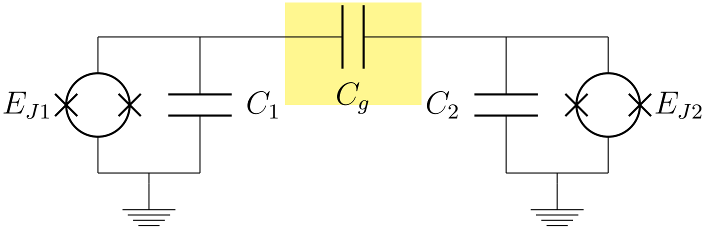

(a) Capacitive coupling

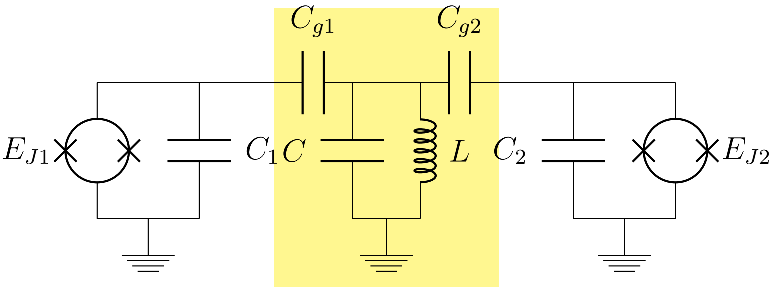

(b) Resonator coupling

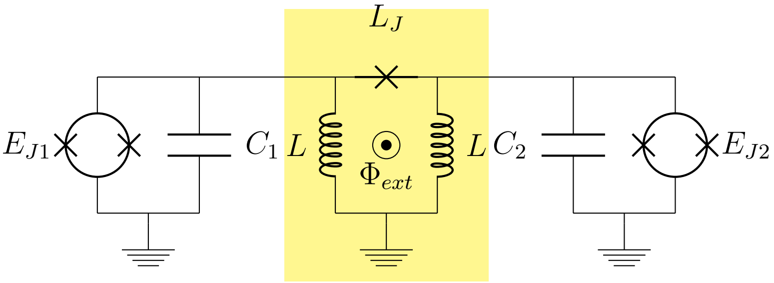

(c) Tunable inductive coupling

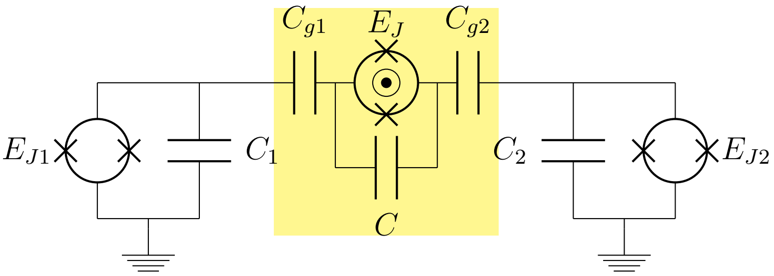

(d) Transmon-bus coupling

Figure 2.9: Examples of coupling schemes for transmon qubits. In **(a)**, two transmons are directly coupled via a capacitance. In **(b)**, an off-resonance resonator mediates interaction between two transmons. This is basically a circuit QED setup, where the transmons are placed inside a CPW. In **(c)**, the transmons are coupled using a Josephson junction which operates in the linear regime and can be tuned by an external flux. The transmons can also be coupled via a third transmon threaded by an external (oscillating) flux as shown in **(c)**.

Josephson junction coupling (inductive coupling) Transmons can be coupled using a Josephson junction. This type of coupling can be made tunable by applying a dc flux through an inductive loop (see Fig. 2.9c) and has recently been realized experimentally [59, 60]. In the limit that $L_J \gg L$, the nonlinearity of the transmons are highly ineffective. To the linear approximation, the coupling has the form of an inductive coupling $g\sigma_1^x\sigma_2^x$ with,

$$g \approx -\frac{\omega_0}{2}\frac{L^2}{(L_q+L)(2L+L_J/\cos\delta)}, \tag{2.70}$$

where we assumed identical qubits with transition frequency ω_0 and Josephson inductor $L_q = L_{qi} = \phi_0^2/E_{Ji}$. δ is the phase drop over the junction set by the external flux.
It is also possible to exploit the strong nonlinear regime of the Josephson junction to generate coupling between several qubits [61].

Transmon bus coupling A transmon circuit can be used to couple two transmons qubits, see Fig 2.9d. Here as well, the coupler can be tuned via an external flux through the dc-SQUID of the coupler. In case of detuned qubits, by parametrically modulating the central SQUID at qubit-qubit detuning, it is possible to implement swap interaction $XX + YY$ [62].

2.7 Measurement of transmon qubit

In this section we briefly discuss the measurement process for a transmon qubit. A detailed discussion can be found in [1, 67].

Quantum theory tells us that the measurement process inevitably exerts at least as much decoherence to the system as the amount of information extracted from the system. Thus one aspect of an ideal measurement is to optimize the information gain with respect to the induced decoherence. On the other hand, an ideal measurement needs to be non-demolition i.e. it should leave the system in a state corresponding to the measurement outcome. In this case, the state can still be manipulated further after the measurement.

Designing a measurement scheme for superconducting qubits needs to take into account their regime of operation. For qubits that operate deep into charge or phase regimes the natural basis for measurement are the charge and phase basis respectively [67]. For a charge qubit the two charge states $|0\rangle$ and $|1\rangle$ can be used to discriminate ground and excited states [63] while for a flux (or phase) qubit, the separation between the two wells is the key for state readout. As a transmon operates in the intermediate regime, it is not possible to use either charge or phase states. Unlike a charge qubit, the state of a transmon is distributed over many charge states and unlike a flux (or phase) qubit the potential of a transmon is periodic, hence one cannot distinguish well two phase states for a measurement. For a transmon qubit, one simple approach would be to directly measure the energy of the qubit. We can capacitively couple the transmon to a transmission line (TL) which is connected to an amplifier. The transmon can release its photon into the TL and it can be measured based on the amplitude of the outgoing photon, see Fig. 2.10a. The problem with this approach is that the signal to noise ratio (SNR) cannot exceed 2 [67]. To improve the SNR, one could employ a second wave to probe the qubit. In this scenario, the transmon is capacitively coupled to the TL and the probe wave is sent into the TL, see Fig. 2.11a. The scattered wave from the qubit, carries a different phase shift depending on whether the transmon is in the ground or excited state. This incurred phase shift can be measured in the output and is used to discriminate the ground state from the excited state. This configuration solves the problem with the SNR, however there is also a drawback associated with it. In order to obtain sufficiently large difference in the phase shift of the two possible outcomes, the spectroscopy on the qubit should be carried out at the frequency of the transmon. This means that the transmon actively interacts with the incoming wave during the process of measurement which lowers the fidelity of the outcome and also violates the non-demolition requirement for the measurement. A possible solution would be to incorporate a resonator into the system as shown in Fig. 2.10c. The resonator introduces a second mode in the system which we assume to be detuned from the transmon. The idea is to perform a spectroscopy on the circuit at the frequency of the resonator. At this frequency the qubit sees the resonator as a short circuit (ground) and therefore is barely affected by the measurement.

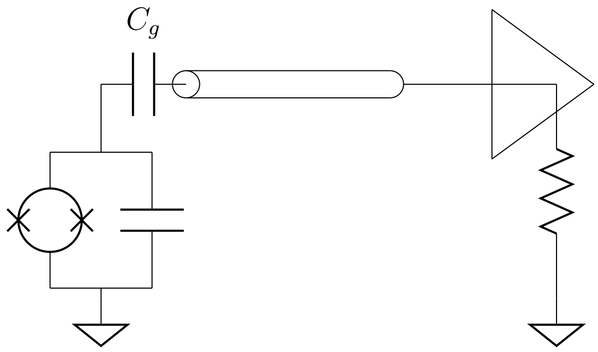

(a) Direct measurement of a transmon by coupling to transmission line.

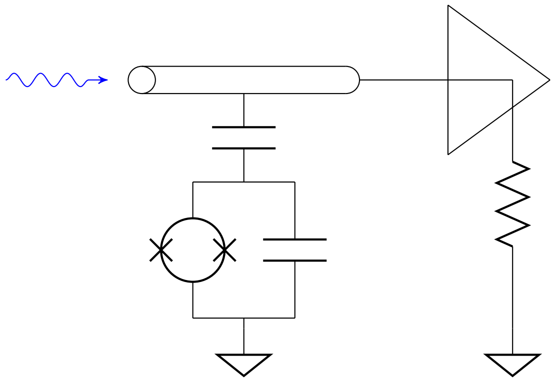

(b) Measurement of a transmon using a probe signal.

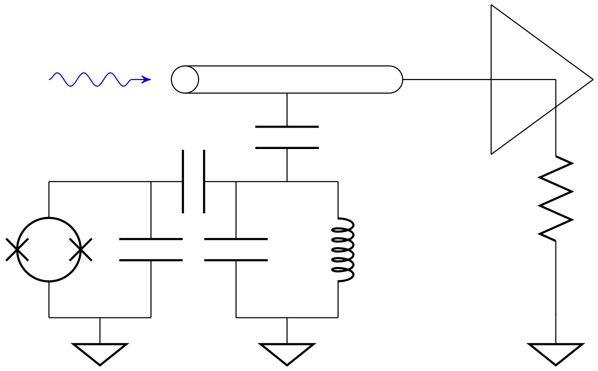

(c) Measurement using an auxiliary resonator

Figure 2.10: Basics of transmon measurement theory. In **(a)**, the measurement is based on energy of an outgoing wave provided by the transmon and therefore the measurement has a low SNR. In **(b)** the transmon is probed by a second wave (in blue) at the frequency of the qubit, which leads to an improved SNR but yet a low fidelity of the measurement. To solve this issue, an auxiliary resonator at a different frequency is coupled to the qubit and the circuit is probed at the frequency of the resonator. The state of the qubit is measured based on the phase shift of the outgoing signal.

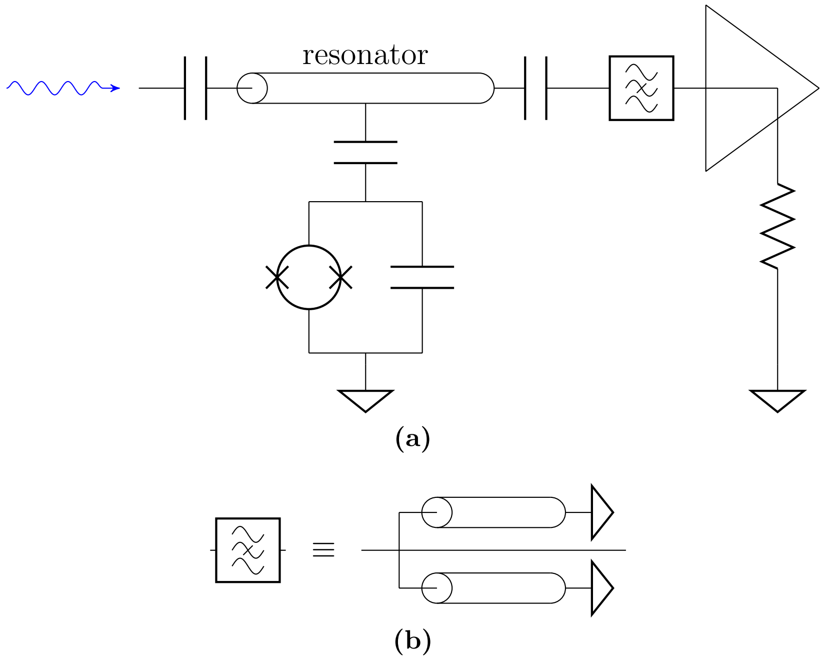

Figure 2.11: Illustration of a transmon qubit readout device with prolonged qubit lifetime. **(a)** The resonator is driven resonantly and the output is filtered at the frequency of the qubit.**(b)** The notch filter is constructed on-chip from a pair of $\lambda/4$ grounded waveguides [68].

Due to the resonance of the resonator mode, in the system the phase shift is still large enough to differentiate between the ground and excited states. This approach for the QND measurement of a transmon qubit has been dubbed *dispersive measurement*. A practical design introduced by the Yale group is shown in Fig. 2.11 [68]. Here, the resonator (CPW) is placed in series with the drive line and in order to increase the qubit lifetime a bandstop (notch) filter at the qubit frequency is connected to the output of the resonator. This filter disallows any energy leakage from the qubit. This setup has the same configuration as a circuit QED system. We argued in Sec. 2.5 that in the dispersive regime, the qubit induces a qubit state dependent frequency shift to the resonator,

$$\chi = \frac{g^2}{\Delta} \tag{2.71}$$

In the transmon measurement, the qubit's pull on the oscillator frequency is measured through spectroscopy on the resonator and there is a difference of

2χ in the measured shift for the two states of the transmon.

2.7.1 Joint readout of transmons

The idea of dispersive readout of a transmon can be generalized to several qubits [49, 66, 69–71]. For two transmons, the frequency shift of the resonator reads $\delta\omega_c = \chi_1\sigma_1^z + \chi_2\sigma_2^z$, where χ_i is defined in Eq. (2.71) and the output transmission amplitude $A(\sigma_1^z, \sigma_2^z)$ takes four possible values depending on the state of the qubits [1]. Therefore one can write,

$$A(\sigma_1^z, \sigma_2^z) = \beta_0 + \beta_1\sigma_1^z + \beta_2\sigma_2^z + \beta_{12}\sigma_1^z\sigma_2^z. \tag{2.72}$$

By ensemble averaging over many measurements one can deduce two-qubit correlations,

$$\langle\sigma_1^z\sigma_2^z\rangle = \frac{1}{4\beta_{12}}(\langle A(\sigma_1^z, \sigma_2^z)\rangle - \langle A(-\sigma_1^z, \sigma_2^z)\rangle - \langle A(\sigma_1^z, -\sigma_2^z)\rangle + \langle A(\sigma_1^z, \sigma_2^z)\rangle). \tag{2.73}$$

Other types of correlations e.g. $\langle\sigma_1^x\sigma_2^y\rangle$ can be measured in z basis, i.e. in terms of $\sigma_1^z\sigma_2^z$, by performing single qubit rotations before the measurement.

So far we considered the measurement using a harmonic oscillator. The readout procedure can be based on a nonlinear harmonic oscillator as well. Measurement schemes using Josephson bifurcation amplifiers [64] as the nonlinear element leads to a high-fidelity readout of a transmon [65]. These schemes make use of a *latching mechanism* in which depending on the qubit state the nonlinear mode latches into one of two possible states. This state remains latched even after the qubit decays, thus providing high signal-to-noise ratio.

2.8 Circuit network theory

In superconducting circuits we typically deal with two-point elements such as capacitors, inductors, Josephson junctions, etc.. An electric circuit of arbitrary size constructed from these elements defines a circuit network. In previous sections, we considered small circuit networks with one or two degrees of freedom

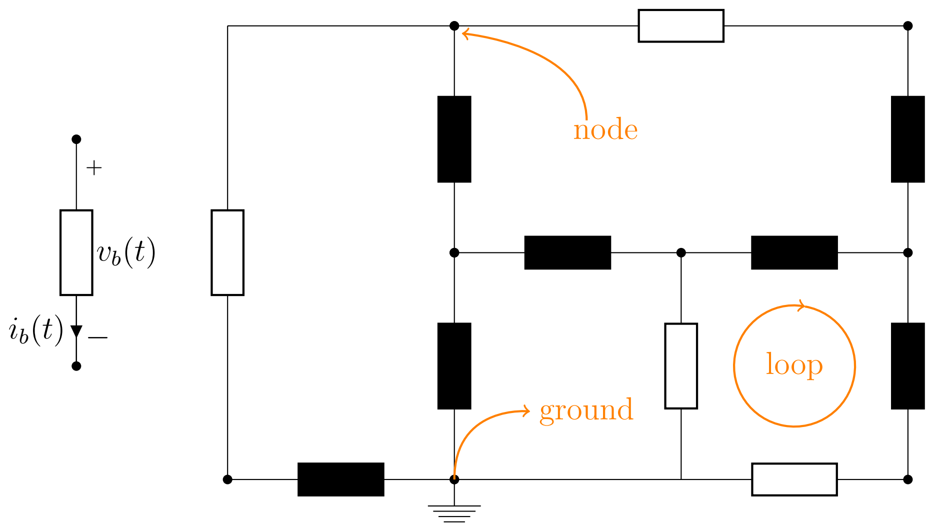

Figure 2.12: Left A generic two-point element in circuit is characterized by its voltage and current. Passive convention requires that the current enters the positive port. **Right** An example of a circuit network. Branches in black form a tree on the network.

(modes). In this section we explain how to derive - in a systematic way - the Hamiltonian description of a circuit network with many modes [72].

An example of a circuit network is shown in Fig. 2.12. On a circuit network, each of the elements is called a branch of the network. A node is defined as a point where two or more branches meet and a loop is a closed path formed by branches. Each branch of the network is characterized by the voltage $v_b(t)$ over the branch and the current $i_b(t)$ through the branch. These variables are related to each other by the characteristic equation for that branch. According to the *passive convention*, the current of a branch enters the node with a higher voltage (+ node).

The state of a circuit network at time t is known if we know the voltages (and hence currents) of all branches at that time. Not all of the branches can define a degree of freedom in a circuit. This is so because the topology of the network sets a number of constraints on the dynamics through Kirschhoff current and voltage law. In particular, the sum of branch voltages around a loop l should be zero and the sum of all branch currents arriving at a typical node i must also be zero. From the branch voltage and current, we define the branch flux and charge which prove convenient in quantum circuit theory, The branch flux and charges are defined as follows,

$$
\begin{aligned}
\Phi_b(t) &= \int_{-\infty}^{t} v_b(t)dt, \\
Q_b(t) &= \int_{-\infty}^{t} i_b(t)dt.
\end{aligned}
\tag{2.74}
$$

The Kirschhoff laws now cast into the form,

$$
\begin{aligned}
\sum_{b\in\text{loop } l} \Phi_b(t) &= \tilde{\Phi}_l, \\
\sum_{b\in\text{node } i} Q_b(t) &= \tilde{Q}_i,
\end{aligned}
\tag{2.75}
$$

where $\tilde{\Phi}_l$ and $\tilde{Q}_i$ are the external flux through the loop l and the residual charge at node i. In classical circuit theory, there are two dual approaches to derive the equations of motion to solve for the dynamics of a circuit [3]. In the node method, one introduces voltages at each node of the network and uses the Kirschhoff current law to write down a set of equations for conservation of currents at network nodes in terms of these *nodal voltages.* Conversely, in the loop method, the loops currents constitute the variable in terms of which a set of equations is written using the Kirschhoff voltage law. For superconducting circuits, we adopt the node method since it is more convenient to deal with phases (fluxes) for the Lagrangian. As in the classical theory, we define a *spanning tree (T).* To define a tree we first assign an arbitrary node of the circuit as the ground. T is a path on the network which contains the ground node and a set of branches that connect all other nodes to the ground such that the tree does not include a loop. We then assign the nodal phases ϕ_n to the nodes of the network. If the nodes of a branch b are denoted by i and $i+1$, the nodal phases ϕ_i and ϕ_{i+1} are related to the branch phase as follows,

$$
\begin{aligned}
\phi_b &= \phi_i - \phi_{i+1}, \quad \text{for } b \in T, \\
\phi_b &= \phi_i - \phi_{i+1} + \tilde{\phi}_l, \quad \text{for } b \notin T,
\end{aligned}
\tag{2.76}
$$

where $\phi_b = \Phi_b/\phi_0$ is the branch phase and $\tilde{\phi}_l = \tilde{\Phi}_l/\phi_0$. It is easy to see that for a network, if b is not a tree branch (i.e. $b \notin T$), it should form a loop (l) with some tree branches. Thus the choice for nodal phase ensures the Kirschhoff law for fluxes (phases). We now can explicitly write the contributions of individual branches in the Lagrangian. A capacitive branch b with end nodes i and $i+1$ and capacitance C_b has a kinetic energy of,

$$\mathcal{E}_b = \frac{\phi_0^2}{2} C_b (\dot{\phi}_i - \dot{\phi}_{i+1})^2. \tag{2.77}$$

The energy of an inductive branch with inductance L_b contributes to the total potential energy as,

$$\mathcal{E}_b = \frac{\phi_0^2}{2L_b} (\phi_i - \phi_{i+1})^2. \tag{2.78}$$

A Josephson junction branch with capacitance C_{Jb} and Josephson energy E_{Jb} has a combination of kinetic and potential energies,

$$\mathcal{E}_b = \frac{\phi_0^2}{2} C_{Jb} (\dot{\phi}_i - \dot{\phi}_{i+1})^2 - E_{Jb} \cos(\phi_i - \phi_{i+1}). \tag{2.79}$$

The total Lagrangian reads,

$$\mathcal{L} = \mathcal{K} - \mathcal{V}, \tag{2.80}$$

where $\mathcal{K}$ is the total kinetic energy of the capacitances and $\mathcal{V}$ is the total potential energy of inductances and junctions. To derive the Hamiltonian, we should first define the conjugate momenta of the nodal phases through the Lagrangian,

$$\pi_i = \frac{\partial \mathcal{L}}{\partial \dot{\phi}_i}. \tag{2.81}$$

π_i has the meaning of $\hbar$ times the number of Cooper pairs on the total capacitance connected to the node i. To see this we note that the conjugate momenta of the nodal fluxes are the total charges of the nodes,

$$Q_i = \frac{\partial \mathcal{L}}{\partial \dot{\Phi}_i}. \tag{2.82}$$

Therefore $\pi_i = \phi_0 Q_i = \hbar Q_i/(2e)$. Eq. (2.81) can also be written in a vector form as $\vec{\pi} = \phi_0^2[\mathbf{C}]\dot{\vec{\phi}}$ where $\vec{\phi} = [\phi_1 \quad \phi_2 \quad ...]^T$ and $\vec{\pi} = [\pi_1 \quad \pi_2 \quad ...]^T$. **C** is the capacitive matrix of the circuit network. From the definition (2.81) it is understood that the capacitive matrix has the following structure: the diagonal elements (C_{ii}) are the sum of capacitances connected to the node i and the off-diagonal elements C_{ij} are minus the total capacitance between the nodes i and j. The total kinetic energy reads:

$$\mathcal{K} = \phi_0^2 \dot{\vec{\phi}}^T[\mathbf{C}]\dot{\vec{\phi}} = \frac{1}{\phi_0^2}\vec{\pi}^T[\mathbf{C}^{-1}]\vec{\pi}. \tag{2.83}$$

Finally the Hamiltonian can be written as,

$$H = \sum_i \pi_i \dot{\phi}_i - \mathcal{L} = \vec{\pi}^T \dot{\vec{\phi}} - \mathcal{L} = \frac{1}{\phi_0^2}\vec{\pi}^T[\mathbf{C}^{-1}]\vec{\pi} + \mathcal{V}. \tag{2.84}$$

2.9 Summary

In this chapter, we explored some aspects of superconducting circuits. We derived the Hamiltonian of a quantum LC circuit and Josephson junction as the basic linear and nonlinear elements of superconducting circuits in detail and showed that a Josephson junction enables us to define several types of qubits. In particular, our discussion centered around a transmon qubit (or more generally Cooper pair box) which we will use as the qubit in our architectures in later chapters. We then considered simple transmon based configurations which can be employed as building blocks of larger circuits, i.e. circuit quantum electrodynamics (circuit QED) and static couplings between transmon qubits and also reviewed the process of measuring a transmon qubit. At the end of the chapter, we presented an approach to derive the Hamiltonian of an arbitrary superconducting circuit network with many degrees of freedom. This approach is specifically useful in Chap. 4, where we propose our circuit for quantum simulation of the toric code. In the next chapter, we introduce quantum simulation and discuss how superconducting circuits can be used as a platform for quantum simulation.

Chapter 3

Quantum simulation with superconducting circuits

In chapter 2, we discussed that superconducting circuits provide a platform with great potential to fabricate artificial quantum systems with multiple qubits. In this thesis our mission is to demostrate that this setting can efficiently be used to implement quantum simulators of interesting condensed matter spin models. Before undertaking this task, in this chapter, we briefly discuss the meaning and objectives of quantum simulation and approaches to implement a quantum simulator.

Simulation of a large quantum system on a classical computer is a formidable task. The reason for this is that the number of parameters that describes a state of a quantum system grows exponentially with the system's size. As an example, a chain of N spin 1/2 particles has 2^N spin configurations. To store the amplitudes of these configurations in an arbitrary state, one typically needs 32×2^N bits of memory (32 bits each coefficient). When N reaches 50, this amounts to almost 32000 TB of memory to store the data in a classical computer - which is definitely beyond the capabilities of a classical computer. Yet, performing computation on a $2^N \times 2^N$ Hamiltonian to calculate the time evolution or an observable demands for an additional memory and a computation time that scales exponentially with N. Looking from the opposite angle, this N-qubit quantum system can be seen as an extremely powerful computational resource which can outperform any classical computer. The central idea in quantum simulation and quantum computation is to use a quantum system for the tasks which is too cumbersome to ask classical computers for. If it is extraordinarily hard to simulate the equations that govern a quantum system on a classical computer, a simple solution is to bulid a quantum computer that operates according to those equations. In this way the quantum system itself computes and solves the problem! The concept of quantum simulation was initially put forward by Feynman in 1982 [73],

> *" Let the computer itself be built of quantum mechanical elements which obey quantum mechanical laws."*

In this chapter, we briefly discuss the basics of quantum simulation. The definition of quantum simulators is given in Sec. 3.1. In Secs. 3.2 and 3.3 we define the two approaches towards quantum simulation, i.e. digital and analog quantum simulation. In Sec. 3.4, we provide a set of criteria for quantum simulators. Finally a brief review of the current research on quantum simulation with superconducting circuits is provided in Sec. 3.5.

3.1 What is a quantum simulator?

A quantum simulator is a controllable quantum system designed to emulate the model of another quantum system which is difficult to study otherwise [74]. The goal of a quantum simulator is to reveal the features of a mathematical model that is believed to capture the most relevant properties of a real physical system it describes, e.g. how accurate the Fermi-Hubbard model describes the superconducting properties of a cuprate [76]. In addition to this, a quantum simulator is expected to offer the possibility of exploring the regimes of the model which are inaccessible in the real material or to modify the model (e.g. through perturbations) to investigate how this modification changes the corresponding properties [75]. In a quantum simulation, one prepares an initial state $|\Psi(t=0)\rangle$ corresponding to the initial state of the real system. The initial state is then evolved according to the mathematical model of interest until a final time t_f. The final state $|\Psi(t=t_f)\rangle$ is then measured and one can compare it to the expected final state of the real system. The simulation should be performed in a regime where there are available experimental data on the real physical system so a comparison to the outcome of the simulator is accomplishable. In quantum simulation, there are two approaches to replicate the time-evolution of the model i.e. $U = \exp(-iHt)$ where H is the target Hamiltonian. In the first approach the aim is to generate the time evolution operator effectively by a sequence of one or two-body gates. The quantum simulator in this approach is basically a quantum computer, i.e. the quantum counterpart of classical digital computers in which a series of logical gates and memories are employed to perform a computation. For this reason, this type of simulation is dubbed *digital quantum simulation*. It can also be thought as quantum engineering on the *software level*, since the basic elements of the simulator are universal gates and an arbitrary time evolution operator is constructed by applying them in an appropriate order. In *analog quantum simulation* one tries to directly implement the Hamiltonian of the model on the hardware level. In the next sections, we discuss in more details these two types of quantum simulators.

3.2 Digital quantum simulation

In 1996, Following Feynman's idea, Lloyd took the next step in this field by introducing digital quantum simulators [77]. His idea was that by discretizing the time-evolution operator of a local Hamiltonian in small time steps, each small step can be represented by a one- or two-body interaction. Therefore, the time-evolution is decomposed into a sequence of universal gates. These gates are the basic elements of a quantum circuit model, which is a well-known method in quantum computation to realize quantum algorithms[79]. A digital quantum simulator is then a quantum computer and quantum simulation can be seen as running a quantum algorithm on a quantum computer. Notwithstanding, the term quantum computer is usually used for more abstract mathematical functions, without a direct relevance to a physical system. Moreover, as the results of a quantum computer is taken as guaranteed without a further reference to a physical system, a quantum computer necessitates higher precision than a quantum simulator. The advent of error correction and fault-tolerant quantum computation, has improved the accuracy of quantum computers while it also entails more computational resources alongside. In contrast, the desired output from a quantum simulator includes physical properties such as correlation functions, order parameters, phase diagrams etc. which typically are robust observables. Thus, it could be possible to draw conclusions about the outcome of a quantum simulation e.g. about a phase transition even in the absence of high precision. On these grounds, although a digital quantum simulation can be run on a universal digital quantum computer, the efficiency of such operation is questionable, since quantum computers are more demanding devices than quantum simulators. Even with tens of qubits, one could already perform useful quantum simulations [80, 81], whereas thousands of qubits would be required for factorizing even modest numbers using of Shor's algorithm [75].

We now show the essence of how digital quantum simulation works. Let us take the Hamiltonian $H = \sum_{l=1}^{M} H_l$ where H_l is a few-body local term. Unless $[H_l, H_{l'}] = 0$ for all l and l', we have,

$$U \neq \Pi_l \exp(-iH_l t). \tag{3.1}$$

In order to make an approximation to the time-evolution, U can be split into N steps, where at each step the system evolves for a time δt such that $t = N\delta t$,

$$U = (\exp(-iH\delta t))^N. \tag{3.2}$$

For $\delta t \to 0$, we can use Eq. (3.1) to approximate the time evolution in each step since the error is of the order of $[H_l\delta t, H_{l'}\delta t] \propto (\delta t)^2$,

$$U(t \to t + \delta t) = \Pi_l \exp(H_l \delta t) + \mathcal{O}(\delta t^2). \tag{3.3}$$

When $N \to \infty$, the product gives the exact result. This decomposition is called the *Trotter decomposition*. Each infinitesimal time evolution can be implemented using a number of gates. The precision of a universal digital quantum simulation can be arbitrarily high, however at the cost of exponentially increasing number of gates. In practice, one can minimize the error by keeping higher-orders in the decomposition [80, 82].

3.3 Analog quantum simulation

A second approach to quantum simulation is analog quantum simulation. In an analog quantum simulation, the Hamiltonian of the desired model is directly mapped to the Hamiltonian of the simulator. This approach is closer to the initial idea proposed by Feynman: *... there is to be an exact simulation, that the computer will do exactly the same as nature* [73]. As opposed to the operation of a digital quantum simulation, which is based on discretization into many time steps, an analog quantum simulator operates continuously in time. Analog quantum simulators do not rely on the Trotter decomposition, nor do they suffer from the errors involved in that process. On the other hand, error correction protocols and fault tolerant schemes become meaningless for analog quantum simulation. The Hamiltonian of the simulator typically implements effective many-body terms and should allow for enough control over the parameters of the Hamiltonian. This is realized through externally applied control fields or ancilla degrees of freedom. The parameters of the Hamiltonian can locally or globally be tuned in situ. In addition, analog quantum simulators are purpose-oriented (non-universal) devices which are designed to test a specific model or a family of related models. This makes them much simpler in design than a universal digital quantum simulator. These devices typically are resilient to error sources up to a certain tolerance level, and thus do not impose high demands on the accuracy of the simulators.

3.4 Criteria for quantum simulators

The definition and expected functionality of a quantum simulator suggest the following criteria [76] for an ideal device,

1. **Controllability** Ideally a quantum simulator should be controllable in all stages of a simulation, namely in state preparation and initialization, time evolution and measurement. In addition to the control over the time

evolution of a simulator (e.g. parameters of the Hamiltonian), one should have enough control over the device to extract (measure) all required observables to test a proposed model. To validate a simulator, it is also necessary that it can be tuned to regimes where analytical or numerical results exist.

2. **Reliability** One needs to make sure that the measured output of a quantum simulator coincides with the actual value given by the mathematical model. But how do we know that the simulator represents the model then? [78]

   The first thing to check about a simulator is to see whether it gives the expected outcomes for cases with known results. Also often in experiments, there are observables that are bounded by a maximum or minimum value. Therefore one should also verify whether these bounded observables satisfy their expected limits. Sometimes in an experiment, changing a specific parameter, should result in a particular predictable change in the outcome. One could then run the simulator for a few values of that parameter to confirm whether that certain relationship is manifest in the measurement outcomes. For example, flipping the direction of the magnetic field in Ising model should result in flipping the spin component along the field. This then leads to a particular relationship between the measured quantities in two simulations with opposite direction of the field. Another way of testing a simulator, is to use a number of simulators with potentially different sources of error to compare their measurement outcomes. It is important to note that after all, passing these tests does not validate a simulator, but rather failing to pass invalidates it. In other words, to recognize the reliability of a simulator, we rely on its falsifiability or testability: We subject the simulator to different tests, and unless the simulator fails the test we say it is reliable.

3. **Efficiency** The simulator should aim at problems which is comparatively less expensive in terms of computational resources on a quantum simulator than a classical computer. This means that the resources for initialization, evolution and measurement should at most scale polyno-

mially with the size of the system on a quantum simulator, while the required resources scale exponentially on a classical computer.

3.5 Quantum simulation with superconducting circuits

The whole field of superconducting circuits is inspired, initiated and followed by the ultimate goal of building a quantum computer which is able address intricate problems for classical computers. Being less challenging devices to implement, quantum simulators are seen as more realistic goals to reach along the way towards the celebrated universal quantum computer. In this section, we briefly review the proposals and experiments for implementations of quantum simulators with superconducting circuits. A more comprehensive account of this subject can be found in [84, 85].

In Sec. 2.5, we discussed that the Jaynes-Cummings Hamiltonian is realized in a circuit QED setup where transmon qubits are coupled to coplanar waveguides (CPW). To study the physics of the Bose-Hubbard model, an analog quantum simulator could be built from an array of such circuit QED building blocks where the resonators are coupled together capacitively [83, 95–97]. This system is described by the so-called Jaynes-Cummings-Hubbard model,

$$H = \sum_j H_j^{JC} - \sum_j J(a_j^\dagger a_{j+1} + \text{H.c.}), \tag{3.4}$$

where H_j^{JC} is the Jaynes-Cummings Hamiltonian and the second term in Eq. (3.4) describes the hoppings between blocks. Since we consider an implementation with superconducting circuits, this model is further enriched by the existence of dissipation. As an example, dissipation-driven localization of a two-site system is being discussed in [86] and experimentally tested in [98]. The recent experimental results for a longer chain is presented in [99].

Moreover, there are regimes of cavity QED in which the coupling strength (g) is comparable to the energy of the cavity mode (ω_c). These are the so-called ultrastrong coupling (USC) and deep-strong coupling (DSC) regimes for

$g/\omega_c \leq 1$ and $g/\omega_c \geq 1$ respectively. The Jaynes-Cummings model is no longer valid for these coupling strengths, since the counter-rotating terms should be included for a correct modelling of the system. The Rabi model is given by adding the counter-rotating terms to the Jaynes-Cummings model,

$$H_{\text{Rabi}} = \hbar\omega_q \sigma^+\sigma^- + \hbar\omega_c a^\dagger a + g(a + a^\dagger)(\sigma^+ + \sigma^-). \tag{3.5}$$

While USC and DSC are difficult to reach in other physical implementations, they are comparably easier to realize in superconducting circuits, i.e. circuit QED. A digital quantum simulator for exploring USC/DSC regimes of Rabi model is proposed in [87, 88, 90, 105]. In the lab frame, the circuit operates in the intermediate coupling strength of $g/\omega_c \sim 10^{-3}$, however by transforming the Hamiltonian to rotating frames, the effective resonator frequency ω_c is made small such that effective ratio of $g/\omega_{eff} \sim 1$ is achievable. Note that analogous to JCH model, in the USC/DSC regimes one can define a Rabi-Hubbard model.

Digital quantum simulations of spin systems are discussed in [89, 93]. In [89], digital quantum simulation of Heisenberg and Ising spin Hamiltonians are realized in a circuit QED system experimentally. The isotropic Heisenberg Hamiltonian for N spins reads,

$$H = \sum_{i=1}^{N-1} J(\sigma_i^x \sigma_{i+1}^x + \sigma_i^y \sigma_{i+1}^y + \sigma_i^z \sigma_{i+1}^z) = \sum_{i=1}^{N-1} \frac{J}{2}(H_{i,i+1}^{XY} + H_{i,i+1}^{YZ} + H_{i,i+1}^{ZX}), \tag{3.6}$$

where $H_{i,j}^{\alpha\beta} = \sigma_i^\alpha \sigma_j^\alpha + \sigma_i^\beta \sigma_j^\beta$. Note that in a circuit QED setup, H_{12}^{XY} is the typical XY exchange interaction which is constructed via a dispersive coupling of transmons to a CPW, See Chap. 2. H_{12}^{YZ} and H_{12}^{ZX} can then be constructed from H_{12}^{XY} by a local rotation of the qubits. For a two spins the different terms of the Hamiltonian 3.6 commute with each other and as a consequence, the time evolution operator decomposes into the product of time evolutions corresponding to the individual terms. For three spins however, the individual terms do not commute with each other anymore, and the time-evolution should be performed in small time-steps to avoid Trotter decomposition errors.

Barends *et al.* investigated a range of Ising-type models in a four-qubit digital quantum simulator [38]. In their experiment, the initial Hamiltonian reads,

$$H_{\text{initial}} = -B_{x,I} \sum_i \sigma_i^z, \tag{3.7}$$

which describes non-interacting spins in an external field along the x-axis with the strength $B_{x,I}$. The final Hamiltonian in the rotating frame reads,

$$H_{\text{final}} = -\sum_i (B_{iz}\sigma_i^z + B_{ix}\sigma_i^x) - \sum_i (J_{zz}^{i,i+1}\sigma_i^z\sigma_{i+1}^z + J_{xx}^{i,i+1}\sigma_i^x\sigma_{i+1}^x), \tag{3.8}$$

and they perform an adiabatic sweep from the initial Hamiltonian to the final Hamiltonian,

$$H(\lambda) = (1-\lambda)H_{\text{initial}} + \lambda H_{\text{final}}. \tag{3.9}$$

In this way they could prepare 4 qubit GHZ state and also studied a frustrated Ising Hamiltonian with random X and Z field and random ZZ and XX couplings.

Superconducting circuits are bosonic systems by nature since their constituents are microwave photons. These circuits can thus be used as quantum simulators for other bosonic or spin models. Nonetheless to study the Fermi-Hubbard model, one can map these models onto a spin model via Jordan-Wigner transformation [91]. This approach for digital quantum simulation of the Fermi-Hubbard model is proposed theoretically in [92] and has also been realized experimentally [93]. Using Jordan-Wigner transformation, other fermionic models like Anderson and Kondo models would also be amenable to quantum simulators based on superconducting circuits [94].

Quantum simulation of lattice gauge theories [110, 117] is yet another research topic which is actively pursued in different physical platforms. In superconducting circuits, analog quantum simulation of $U(1)$ Abelian quantum link models in one- and two-dimensions have been proposed theoretically [101, 102]. Reference [100] provides a proposal for digital quantum simulation of a non-Abelian $SU(2)$ lattice gauge theory with superconducting circuits.

Quantum chemistry problems are also in the focus of intense research in the field of quantum simulators. Indeed, quantum chemistry is one of the most anticipated applications of quantum computing. Here the interesting problem to solve is to find the ground state energy of molecules [103]. As an example of the research in this area we can mention the experimental work on the ground state energy curve of the Hydrogen molecule [104].

3.6 Summary

In this chapter, we discussed the meaning and objectives of quantum simulation and two main approaches towards it, namely digital and analog quantum simulation. In the last part of the chapter, we gave a brief review of recent advances in quantum simulation with superconducting circuits. In the following chapter, we put forward a proposal for analog quantum simulation of a well-known many-body topological model, i.e. the toric code.

Chapter 4

Analog quantum simulation of the toric code

In this chapter, we present our approach for an analog quantum simulation of the toric code model [106, 107]. The toric code model lies at the border of topological phases of condensed matter physics [108, 109] and quantum-error correction in quantum information science [111]. From a condensed matter point of view, the toric code is an example of a $\mathbf{Z}_2$ lattice gauge theory [110] and is also a central model in the class of topologically-ordered quantum many-body systems. Topological order defies the contemporary characterization of phases of matter based on their symmetry-breaking properties and defines a new paradigm for classifying condensed matter systems. Topological order is characterized by degeneracy of the ground states on a surface with nontrivial topology (e.g. a torus), long-range entanglement and exotic quasi-particles which exhibit neither bosonic nor fermionic behaviour. It manifests itself in global properties rather than local ones, e.g. degenerate ground states of a topologically-ordered system are indistinguishable locally and they only can be identified via non-local operators. On the other hand, the toric code is closely tied with the stabilizer formalism for quantum error correction introduced by Daniel Gottesman [111]. Indeed the proposal of the toric code by Alexei Kitaev [106] was inspired by the work of Gottesman. Quantum error correction is an algorithmic approach to detect, control and correct errors while performing quantum computation. The idea is to choose a subspace $\mathcal{C}$ of the Hilbert space to store quantum information and carry out quantum computation, such that the action of possible errors (e.g. single qubit errors) would take the states in $\mathcal{C}$ out of this subspace. In the toric code as a Hamiltonian, the error correction is implemented at the hardware level, i.e. the error-correcting code space is the degenerate manifold of ground states of the Hamiltonian. This can also be regarded as a *passive error correction* since the generation of errors is suppressed at low temperatures due to an energy gap between the code space and the states out of this space. Hence provided temperature is low enough, taking the system out of the code space would require an energy that is not available. On the other hand, the toric code can also be implemented via an *active error-correction* at the software level by performing measurements on a fault-tolerant topological quantum memory, detect errors and correct them manually [115, 116].

For an implementation of the toric code on the hardware level, the Hamiltonian includes four-body interaction which are not typically realized in a physical system. For this reason, despite its intriguing perspectives for quantum information and condensed matter physics, progress towards its implementation has been inhibited. As we already discussed in the last chapter, implementation of multi-body terms through digital quantum simulation encounters Trotterization errors. Another approach to tackle this challenge, is to use the so-called *perturbative gadgets* to break a $k-$body term into two-body terms [112–114]. However in this method the number of constituent particles gets multiplied since each degree of freedom in a model is represented by several particles which introduces additional complexities for a physical implementation, control, etc. In contrast, in our scheme four-body terms are directly implemented via analog quantum simulation [107]. In our proposal, the Hamiltonian of the toric code is realized in the rotating frame of the qubits, thus temperature is irrelevant for the preparation of the ground state manifold and we instead use a adiabatic sweep approach to prepare the desired states. On the other hand, the prepared degenerate manifold is not protected against dissipative processes which are inherent in superconducting qubits. Therefore our toric code cannot be used as a long-lasting quantum memory, and we rather aim at preparing a topologically-ordered phase with microwave photons. We should also note that an implementation of multi-body interactions proves important for the quantum simulation of many other models e.g. lattice gauge theories [117].

This chapter is organized as follows: In Sec. 4.1, we briefly introduce the stabilizer formalism. In Sec. 4.2 we present the toric code model and its anyonic excitations following reference [118]. The superconducting circuit for our implementation is introduced in Sec. 4.3. We derive the Lagrangian and Hamiltonian of the proposed circuit in Sec. 4.4. Based on this Hamiltonian, we show how to derive an effective Hamiltonian description for the circuit in Sec. 4.5. In Sec. 4.6, we discuss our approach for generation of the toric code via engineering a time-dependent external flux. Finally, we propose a minimal circuit for a realistic experimental realization of the toric code and preparation of the ground states of the model in Secs. 4.7 and 4.8.

4.1 Stabilizer codes

A stabilizer $\mathbf{S}_n$ is a set of commuting Hermitian operators S_i with $i = 1...n$, i.e. $[S_i, S_j] = 0$ for all i, j. A particular example of a stabilizer can be defined from operators of the from,

$$S_i = O_1 \otimes O_2 \otimes .... \otimes O_n, \quad O_\alpha \in \{\sigma_\alpha^x, \sigma_\alpha^y, \sigma_\alpha^z, \mathbf{1}_\alpha\}, \tag{4.1}$$

acting on n qubits. Operators of this form of course do not all commute with each other, however to construct a stabilizer just a subset of n commuting operators is needed. Note that each S_i has 2^n eigenstates with eigenvalues ± 1. Since all operators in $\mathbf{S}_n$ commute with each other, they have 2^n joint eigenstates and each of these eigenstates can be uniquely identified by the pattern of n eigenvalues corresponding to n stabilizer operators S_i. Clearly there is just one joint eigenstate with eigenvalue $+1$ for all S_i. Now let $\mathbf{S}_c$ be a subset of $\mathbf{S}_n$ with s elements. The *code space* $\mathcal{C}$ is defined as the joint eigenstates of $S_i \in \mathbf{S}_c$ with eigenvalue $+1$,

$$|\Psi\rangle \in \mathcal{C} \Leftrightarrow S_i |\Psi\rangle = +1 |\Psi\rangle \text{ for all } S_i \in \mathbf{S}_c. \tag{4.2}$$

Note that states inside the code space can be distinguished by their eigenvalues corresponding to the stabilizer operators in $\mathbf{S}_n - \mathbf{S}_c$. The dimension of $\mathcal{C}$ is 2^{n-s}, and therefore the code space can be used to store $n-s$ qubits. Encoding quantum information in such a code space is beneficial to detect and correct errors. Consider an error operator that does not commute with $\mathbf{S}_c$. When acting on the code space, this error will necessarily change some of the eigenvalues with respect to $\mathbf{S}_c$ from $+1$ to -1. In other words, the resulting state does not belong to code space anymore. Thus by measuring $S_i \in \mathbf{S}_c$ and detecting -1 for some of S_i, it is realized that an error has occurred. This measurement is non-demolition since code space is invariant under $\mathbf{S}_c$. The error correction process requires finding an error-correcting operator, such that the combination of the occurred error and the error-correcting operator is the identity. By acting with such an error-correcting operator the original state is retrieved.

The *centralizer* $Z(\mathbf{S}_c)$ is defined as the maximal set of operators of the form (4.1) that commutes with $\mathbf{S}_c$. The action of operators in Z does not result in a state out of the code space. Since these operators transform states inside the code space $\mathcal{C}$, they can be used as logical operators to perform computation.

4.2 The toric code model

The toric code is based on the group $\mathbf{Z}_2$ acting on spin 1/2 degrees of freedom and is defined on a two-dimensional square lattice with spin 1/2 particles on each of the edges of the lattice, see Fig. 4.1a. There are two types of interaction terms in the toric code. Every four spins attached to a vertex s of the lattice form a star and the interaction between them is defined via a *star operator* A_s,

$$A_s = \Pi_{j \in star(s)} \sigma_j^x. \tag{4.3}$$

The spins sitting on the edges of a unit cell form a plaquette p and a *plaquette operator* B_p acts on them which is defined as,

$$B_p = \Pi_{j \in plaq(p)} \sigma_j^z. \tag{4.4}$$

We note that star and plaquette operators are both stabilizer operators of the form defined in Eq. (4.1). The Hamiltonian of the model is given by summing over all star and plaquette operators of the lattice with interaction strength J_s and J_p respectively,

$$\mathcal{H}_{TC} = -J_s \sum_s A_s - J_p \sum_p B_p. \tag{4.5}$$

Star and plaquette terms commute with the Hamiltonian and with each other, therefore the toric code is exactly solvable. Furthermore each interaction term squares to the identity, which means that the eigenvalues of individual terms are ± 1. The ground state $|\Psi_0\rangle$ of the Hamiltonian is the joint eigenstate of all star and plaquette terms with eigenvalue $+1$,

$$A_s |\Psi_0\rangle = +1 |\Psi_0\rangle, \quad B_p |\Psi_0\rangle = +1 |\Psi_0\rangle \quad \text{for all } s \text{ and } p. \tag{4.6}$$

The ground state of the plaquette part is $|000...0\rangle$ where $\sigma^z |0\rangle = +1 |0\rangle$. The ground state is given by projecting this state onto $+1$ sector of the star operators,

$$|\Psi_0\rangle = \Pi_s \frac{1}{\sqrt{2}}(1 + A_s) |000...0\rangle. \tag{4.7}$$

A stabilizer $\mathbf{S}_c$ can be defined from star and plaquette terms of the toric code. The ground state of the model is the code space for an error-correcting code $\mathcal{C}$ based on $\mathbf{S}_c$. On a lattice with N spins and open boundaries, the number of stabilizer terms is equal to the number of spins in the lattice. Consequently, there is just a single state that satisfies Eq. (4.6). On the other hand, on a lattice with periodic boundaries in both directions (i.e. a torus), there are constraints as follows,

$$\Pi_s A_s = \mathbf{1}, \quad \Pi_p B_p = \mathbf{1}. \tag{4.8}$$

This means that one of the stars and one of the plaquettes are dependent on the others and $\mathbf{S}_c$ has $N - 2$ independent terms. Based on the discussion on stabilizer codes in Sec. 4.1, one finds $\mathrm{Dim}(\mathcal{C}) = 4$, i.e. there are four states that satisfy Eq. (4.6). In other words, the ground state of the toric code on a torus is four-fold degenerate. There is a second approach to derive this degeneracy of the ground states based on topological properties of non-trivial loops on a torus. We will come to this point in the next section.

4.2.1 Excitations of the toric code

There are two types of excitation in the toric code called anyons: e-anyons (electric charges) and m-anyons (magnetic vortices), and the ground state of the toric code is the vacuum of all anyonic excitations.

Let us assume we have prepared the ground state of the model. If σ^z_j is applied to a spin j of the lattice, the measured value of the star operator A_s on two adjacent vertices of spin j becomes -1, since,

$$A_s(\sigma^z_j \left|\Psi_0\right>) = -\sigma^z_j A_s \left|\Psi_0\right> = -(\sigma^z_j \left|\Psi_0\right>), \tag{4.9}$$

where we used the fact that $j \in star(s)$, therefore $\{A_s, \sigma^z_j\} = 0$. An e-anyon (electric charge) on a vertex is associated with eigenvalue -1 of the star operator A_s acting on that vertex, see Fig. 4.2a. Therefore we can create two e-anyons on two vertices adjacent to spin j by applying σ^z_j to that spin.

The second type of excitation in the toric code is called *m-anyon*. Starting from the ground state, a pair of m-anyons are generated at two adjacent plaquettes of the lattice by applying σ^x operator on their common spin, see Fig 4.2b. The measurement of the B_p opeartor on the plaquettes with m-anyons leads to eigenvalue -1,

$$B_p(\sigma^x_j \left|\Psi_0\right>) = -(\sigma^x_j \left|\Psi_0\right>). \tag{4.10}$$

By applying $\sigma^z(\sigma^x)$ operators successively on a number of neighboring vertices (plaquettes), we can move the anyon along the path of applied operators, see Fig. 4.2a. This path can also be identified as a string. Therefore, if one creates excitation on the ground state of the toric code, the e- and m-anyons always appear in pairs which are placed at the ends of a string. As long as the final position of the anyons are fixed, the shape of the string along which the operators are applied is not important.

Now consider a case in which we create a pair of anyons from the ground

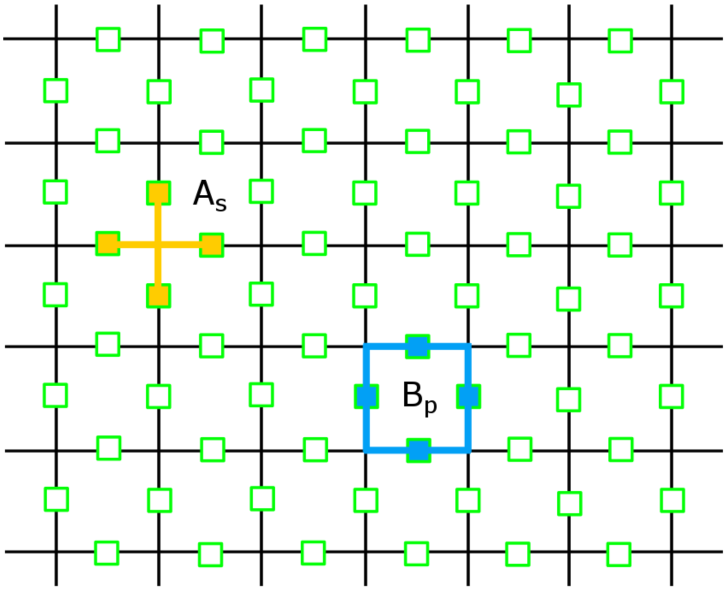

(a)

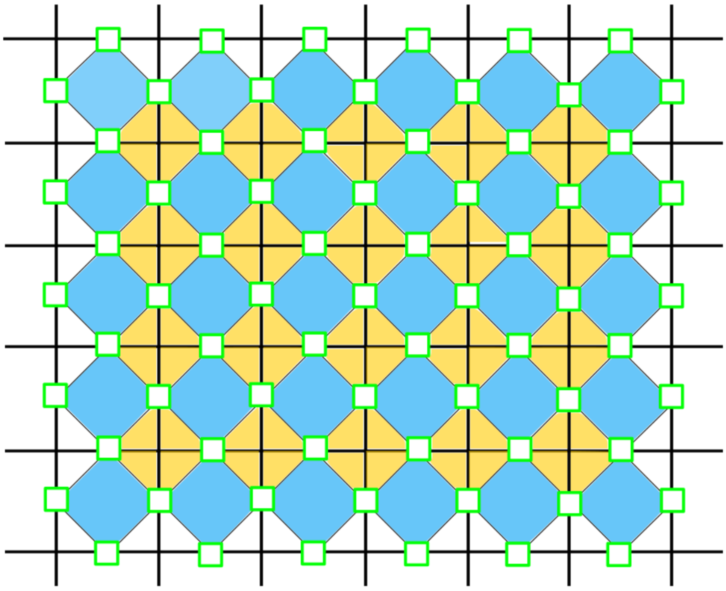

(b)

Figure 4.1: The toric code on a 2D square lattice. **a)** Spins are shown as green boxes at the edges of the lattice. An example of star and plaquette operators A_s and B_p are highlighted in yellow and blue respectively. **b)** The toric code can be visualize on a tilted lattice which is partitioned by star (yellow) and plaquette (blue) cells. The spins of each cell are associated with one stabilizer operator.

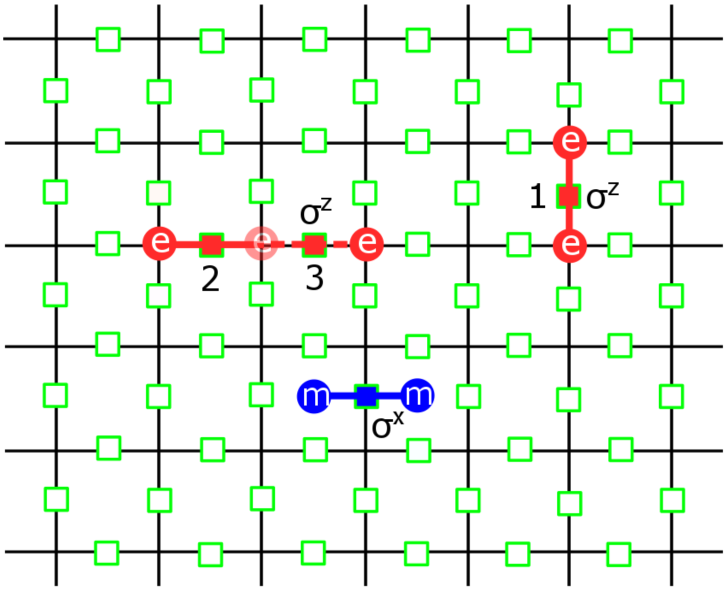

(a)

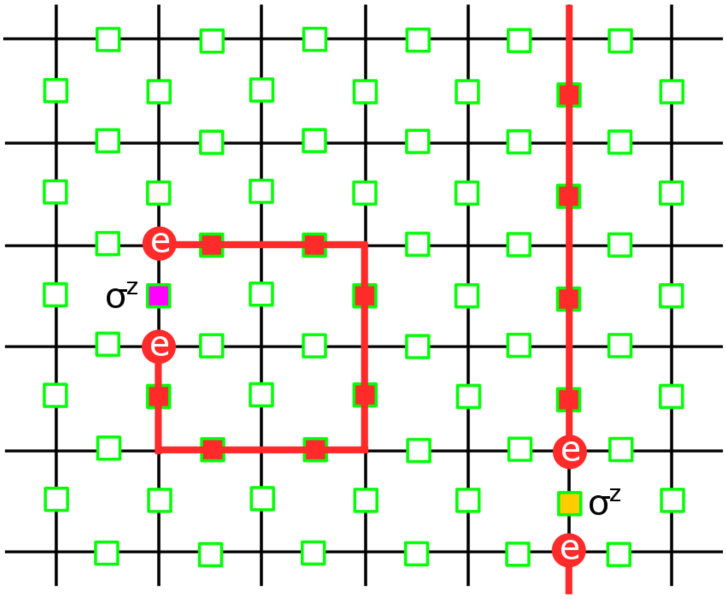

(b)

Figure 4.2: Anyons in the toric code. **a)** A pair of e-anyons (m-anyons) is created by applying σ^z (σ^x) to one spin. If the same operator applies to a spin adjacent to an anyon (e.g. spin 3), the anyon is moved. **b)** The e-anyons are moved around by operating with σ^z along a string. By applying σ^z to the pink or yellow spin the anyons are annihilated and a loop is formed. In this example, the left loop is trivial while the right one is non-trivial or non-contractible.

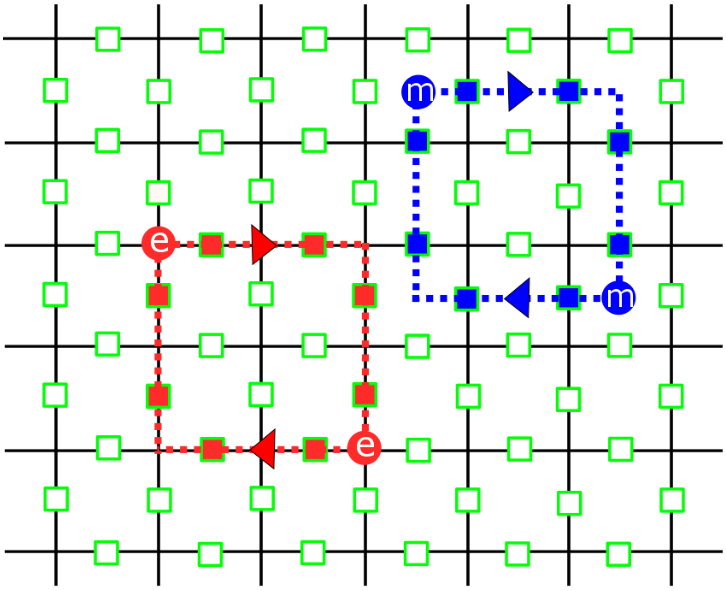

(a)

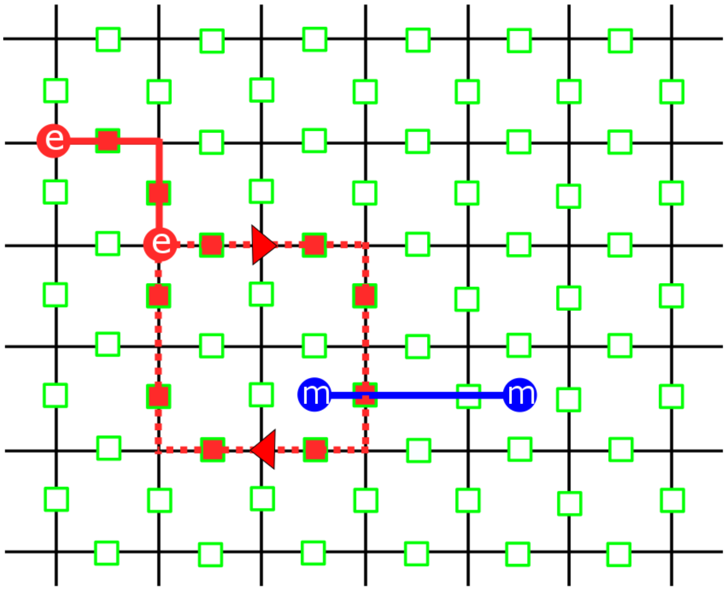

(b)

Figure 4.3: Statistics of anyons **a)** A pair of e- or m-anyons are exchanged by creating trivial loops. As the loops do not contain an anyon of the second type, their action on the state is trivial. This shows the bosonic nature of mutual statistics of a pair of e- or m- anyons. **b)** Braiding an e-anyon around a m-anyon. The e-anyon creates a loop which encircles the m-anyon and gives an extra -1 in the process. This factor indicates the anyonic nature of statistics between different types of anyons.

state and then move them around to form a loop, see Fig. 4.2b. In this case, the anyons annihilate each other and we should recover the ground state since the lattice is vacant of excitations. There are two type of loops on a torus: *Contractible loops* and *non-contractible loops.* Contractible loops can be smoothly deformed to reduce down to a point as opposed to the non-contractible loops. The application of contractible loops leave a ground state unchanged, i.e. it acts as an identity on that ground state [1]. In contrast, non-contractible loops should transform a ground state to another distinguishable ground state as the two states differ in their *winding numbers* around the torus. Since a torus possesses two *topologically different*[2] non-contractible loops, we can conclude that on this surface, the toric code has four degenerate ground states.

To study the mutual statistics of anyon excitations, we start from a state with a pair of e-anyons. To exchange the positions of the two e-anyons, one needs to make a (trivial) loop of σ^z operators, see Fig. 4.3a. Assuming this loop does not enclose a m-anyon, the final state should be the same as the initial one. A similar statement holds if two m-anyons are exchanged via a loop of σ^x operators which does not contain an e-anyon. The mutual statistics between a pair of e-anyons or a pair of m-anyons is then bosonic. Now let us consider a case with an pair of e-anyons and a pair of m-anyons, see Fig. 4.3b. Each pair should be located at the end points of a string connecting the two anyons. Since the e- and m-anyons are distinguishable, we cannot exchange their position but rather we should *braid* them. Braiding can be regarded as two successive exchanges and it means that we move one e-anyon [3] around the m-anyon and then bring it back to its initial position. The braiding results in a loop of σ^z operators which necessarily cuts the string of the second pair at one spin (string of σ^x). As $\{\sigma^z, \sigma^x\} = 0$, this results in a minus sign difference between the initial and final states. This -1 factor reveals a non-trivial statistics between the two type of excitations, so we can assign an imaginary i factor to the exchange of e- and m- anyons. Note that this behaviour is different from braiding (two exchanges) of bosonic or fermionic particles which results in a

---

[1] We assume the loop does not contain anyons.

[2] Topologically different loops cannot be smoothly deformed to each other.

[3] Equivalently one could move the m-anyon around the e-anyon.

+1 factor, and therefore it is called *anyonic statistics.*

4.3 Superconducting lattice for the toric code

To define a physical lattice for the toric code, it proves more convenient to visualize the toric code on a tilted lattice as shown in Fig. 4.1b. Each unit cell of this lattice contains four adjacent spins that interact via one stabilizer term in the model. Depending on the type of interaction between the spins of a cell, we call it a star or plaquette unit cell. The original lattice is then covered in a checkerboard pattern by star and plaquette cells. Furthermore, we make a rotation on the spins around the x-axis to re-define the B_p operators in terms of σ^y,

$$B_p = \Pi_{j \in plaq(p)} \sigma^y_j. \tag{4.11}$$

Note that these rotations leaves A_s operators intact,

In our implementation of the toric code model with superconducting circuits, spins define the nodes of the circuit and transmon qubits attached to the nodes represent spin degrees of freedom. We label the transmon nodes by a composite index $j \equiv (n, m)$ along the tilted lattice formed by the pattern of star and plaquette cells (or along the diagonals of the original lattice). n labels the diagonals from bottom left to top right and m labels the transmons along each diagonal [4]. Each star or plaquette cell then includes the nodes (n, m), $(n, m+1)$, $(n+1, m)$ and $(n+1, m+1)$ and can uniquely be labelled by $[j] = [n, m]$.

To generate the desired star and plaquette couplings, we introduce a coupler as shown in Fig. 4.4 between the four neighbouring spins sitting at the corners of a star or plaquette cell $[j]$. This coupler is composed of a dc-SQUID with a total Josephson energy $2E_J$ and a total capacitance $2C_J$, which is connected to the transmons of a star or plaquette cell via four inductors each with an inductance L. The dc-SQUID of the coupler in cell $[j] = [n, m]$ is threaded by a time-dependent external magnetic flux, $\Phi_{ext;j}(t) \equiv \Phi_{ext;n,m}(t)$. We should emphasize here that the coupler has the same circuit for star and plaquette

---

[4] Note that each diagonal has a different number of spins.

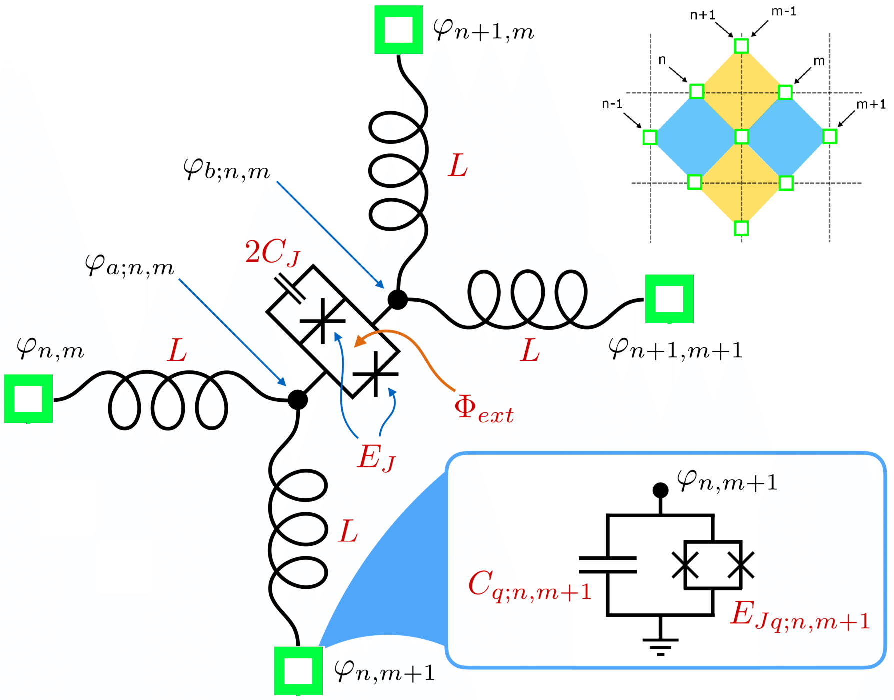

Figure 4.4: Coupling circuit within each star or plaquette cell. The coupler consists of a dc-SQUID which is connected to the four qubits of a cell by four inductors. The SQUID is modulated by an external flux Φ_{ext}. The inset shows a piece of the toric code lattice with labelled diagonals.

cells and the form of the interaction is engineered via the external flux as we will discuss later. Each coupler introduces two additional nodes (i.e. degrees of freedom) in a given cell $[j] = [n, m]$, namely the nodes of the dc-SQUID which are labelled by $(a; j) \equiv (a; n, m)$ and $(b; j) \equiv (b; n, m)$.

In the following section, we will show that the two degrees of freedom of a coupler SQUID can be re-defined in terms of center-of-mass and breathing modes. Whereas the center-of-mass mode is high-frequency and hence discarded, the breathing mode acts as an ancilla that mediates interactions between the adjacent transmons. In the operational regime we consider here, the breathing mode stays in the ground state and therefore we derive an effective Hamiltonian in which the breathing mode is adiabatically eliminated.

4.4 Lagrangian and Hamiltonian of the lattice

In this section, we present a detailed derivation of the Lagrangian and Hamiltonian of the lattice following the discussion in Sec. 2.8. To this end, we assign a phase $\phi_j \equiv \phi_{(n,m)}$ to the node $j = (n, m)$ of the circuit. The phases of the two nodes of a coupler inside cell $[j] = [n, m]$ are denoted by $\phi_{a;j} \equiv \phi_{a;n,m}$ and $\phi_{b;j} \equiv \phi_{b;n,m}$.

The contribution of the transmon qubits in the Lagrangian reads,

$$\mathcal{L}_q = \sum_{n,m=1}^{N,M} \left[\frac{1}{2}\phi_0^2 C_{q;n,m}\dot{\phi}_{n,m}^2 + E_{Jq;n,m}\cos(\phi_{n,m}) \right], \tag{4.12}$$

where $C_{q;n,m}$ is the capacitance of the transmon connected to the node (n, m) and $E_{Jq;n,m}$ is its effective Josephson energy, which can be tuned via a dc-flux. The contribution of the dc-SQUIDs of the coupler reads,

$$\begin{aligned}\mathcal{L}_S = \sum_{n,m=1}^{N,M} \Bigg[&\frac{1}{2}\phi_0^2 C_g \dot{\phi}_{a;n,m}^2 + \frac{1}{2}\phi_0^2 C_g \dot{\phi}_{b;n,m}^2 + \phi_0^2 C_J (\dot{\phi}_{a;n,m} - \dot{\phi}_{b;n,m})^2 \\ &+ 2E_J \cos(\phi_{ext;n,m}/2)\cos(\phi_{a;n,m} - \phi_{b;n,m}) \Bigg],\end{aligned} \tag{4.13}$$

where C_g is a tiny parasitic capacitance between SQUID nodes and the ground. The contribution of the inductors is,

$$\begin{aligned}\mathcal{L}_L = \sum_{n,m=1}^{N,M} \frac{\phi_0^2}{2L} \Bigg[&(\phi_{a;n,m} - \phi_{n,m})^2 + (\phi_{a;n,m} - \phi_{n,m+1})^2 + (\phi_{b;n,m} - \phi_{n+1,m})^2 \\ &+ (\phi_{b;n,m} - \phi_{b;n+1,m+1})^2 \Bigg].\end{aligned} \tag{4.14}$$

Therefore the entire Lagrangian of the lattice reads,

$$\mathcal{L} = \mathcal{L}_q + \mathcal{L}_S + \mathcal{L}_L = \mathcal{K} - \mathcal{V}, \tag{4.15}$$

where $\mathcal{K}$ is the kinetic energy of the circuit originated from the capacitors and

$\mathcal{V}$ is the potential energy of the inductors and junctions. As the dc-SQUID of a coupler only couples the differences of phases, we define the following center-of-mass (COM) and breathing modes,

$$\phi_{\pm;n,m} = \phi_{a;n,m} \pm \phi_{b;n,m}. \tag{4.16}$$

We call these modes " + " and " − " modes as well. In terms of the new variables the kinetic part of the Lagrangian is re-written as,

$$\mathcal{K} = \sum_{n,m} \frac{1}{2}\phi_0^2 \Big[C_{q;n,m}\dot{\phi}^2_{n,m} + (2C_J + \frac{C_g}{2})\dot{\phi}^2_{-;n,m} + \frac{C_g}{2}\dot{\phi}^2_{+;n,m} \Big]. \tag{4.17}$$

Note that in terms of the breathing and center-of-mass modes, the kinetic energy becomes the sum of two non-interacting modes. The conjugate momenta of nodal phases read [5],

$$\begin{aligned}
\pi_{n,m} &= \frac{\partial \mathcal{L}}{\partial \dot{\phi}_{n,m}} = \phi_0^2 C_{q;n,m}\dot{\phi}_{n,m}, \\
\pi_{-;n,m} &= \frac{\partial \mathcal{L}}{\partial \dot{\phi}_{-;n,m}} = \phi_0^2 (2C_J + C_g)\dot{\phi}_{-;n,m}, \\
\pi_{+;n,m} &= \frac{\partial \mathcal{L}}{\partial \dot{\phi}_{+;n,m}} = \phi_0^2 C_g \dot{\phi}_{+;n,m}.
\end{aligned} \tag{4.18}$$

Assuming that $C_g \ll C_J$, the kinetic energy thus reads,

$$\mathcal{K} = \sum \frac{\pi^2_{n,m}}{2\hbar\phi_0^2 C_{q;n,m}} + \frac{\pi^2_{+;n,m}}{4\hbar\phi_0^2 C_J} + \frac{\pi^2_{+;n,m}}{2\hbar\phi_0^2 C_g}. \tag{4.19}$$

---

[5] We can also use the number of Cooper pairs $n_{n,m} = \pi_{n,m}/\hbar$, etc. instead of momenta, however to avoid any confusion between the lattice index n and number operator, we prefer to use the momenta here.

The Hamiltonian thus reads,

$$
\begin{aligned}
\mathcal{H} &= \mathcal{H}_q + \mathcal{H}_+ + \mathcal{H}_- + \mathcal{H}_L, \\
\mathcal{H}_q &= \sum_j 4\frac{E_{C;j}}{\hbar^2}\pi_{q;j}^2 + 4E_L\phi_j^2 - E_{Jq;j}\cos(\phi_j), \\
\mathcal{H}_+ &= \sum_j 4\frac{E_{C+}}{\hbar^2}\pi_{+;j}^2 + E_L\phi_{+;j}^2, \\
\mathcal{H}_- &= \sum_j 4\frac{E_{C-}}{\hbar^2}\pi_{-;j}^2 + E_L\phi_{-;j}^2 - E_J\cos(\phi_{ext;j})\cos(\phi_{-;j}), \\
\mathcal{H}_L &= \sum_j E_L(\phi_{q+;j}\phi_{+;j} + \phi_{q-;j}\phi_{-;j}).
\end{aligned}
\tag{4.20}
$$

where we have define the variables $\phi_{q\pm;j} \equiv \phi_{q\pm;n,m} = \phi_{n,m} + \phi_{n,m+1} \pm \phi_{n+1,m} \pm \phi_{n+1,m+1}$. We have also introduced the inductive energy scale associated with one inductor and the charging energy scales of the transmons and the SQUID modes in the Hamiltonian as follows,

$$
\begin{aligned}
E_L &= \frac{\phi_0^2}{2L}, \\
E_{q;j} &= \frac{e^2}{2C_{q;j}}, \\
E_{C+} &= \frac{e^2}{C_g}, \\
E_{C-} &= \frac{e^2}{4C_J}.
\end{aligned}
\tag{4.21}
$$

In Eq. (4.20), $\mathcal{H}_q$ describes the Hamiltonian of transmon qubits. In particular, we note that the inductive energy of each transmon is added by the contribution of the four adjacent inductors. $\mathcal{H}_+$ and $\mathcal{H}_-$ are respectively the Hamiltonian of the SQUID's center-of-mass and breathing modes. Finally, $\mathcal{H}_L$ describes the interaction between the SQUID modes of a cell and the four transmons of that cell.

The Hamiltonian (4.20) is quantized in the standard way by imposing the canonical commutation relations,

$$[\phi_j, \pi_l] = i\hbar\delta_{j,l}, \quad [\phi_{\pm;j}, \pi_{\pm;l}] = i\hbar\delta_{j,l}. \tag{4.22}$$

4.5 Derivation of an effective Hamiltonian

4.5.1 Schrieffer-Wolff transformation

We are interested in a regime of the proposed circuit in which the frequencies of the qubits and applied oscillating flux strongly differ from the frequency of the SQUID. An example of the circuit parameters for this regime is given in Sec. 4.7. Under this condition, we expect that the SQUID-qubit couplings are ineffective and the SQUID modes remain in their ground states. An effective description of the low-energy sector of the system is obtained by applying a Schrieffer-Wolff (SW) transformation [119] with the following generator,

$$S = \frac{i}{2\hbar}\sum_j (\phi_{q+;j}\pi_{+;j} + \phi_{q-;j}\pi_{-;j}). \tag{4.23}$$

The transformed Hamiltonian under SW reads,

$$\begin{aligned}\tilde{\mathcal{H}} &= e^{S}\mathcal{H}e^{-S} \\ &= \mathcal{H} + [S,\mathcal{H}] + \frac{1}{2!}[S,[S,\mathcal{H}]] + \frac{1}{3!}[S,[S,[S,\mathcal{H}]]] + \frac{1}{4!}[S,[S,[S,[S,\mathcal{H}]]]] + ...\end{aligned} \tag{4.24}$$

S is chosen such that the Schrieffer-Wolff transformation removes the inductive couplings between the transmons and the SQUIDs (i.e. $\mathcal{H}_L$). However instead, it generates other residual couplings of different types. These include inductive qubit-qubit and qubit-SQUID interactions denoted respectively by $\tilde{\mathcal{H}}_{qI}$ and $\tilde{\mathcal{H}}_{qS}$. Explicit expressions for successive orders of the Schrieffer-Wolff transformation are given in Appendix A. The transformed Hamiltonian $\tilde{\mathcal{H}}$ can be recast into the form,

$$\tilde{\mathcal{H}} = \tilde{\mathcal{H}}_q + \tilde{\mathcal{H}}_+ + \tilde{\mathcal{H}}_- + \tilde{\mathcal{H}}_{qI} + \tilde{\mathcal{H}}_{qS}, \tag{4.25}$$

where $\tilde{\mathcal{H}}_q$ and $\tilde{\mathcal{H}}_\pm$ are renormalized Hamiltonians of the non-interacting qubits and SQUIDs respectively. The free Hamiltonian of the transmons reads,

$$\tilde{\mathcal{H}}_q = \sum_j \tilde{\mathcal{H}}_{q;j} = \sum_j 4\frac{E_{C;j}}{\hbar^2}\pi^2_{q;j} + 2E_L\phi_j^2 - E_{Jq;j}\cos(\phi_j), \tag{4.26}$$

where the inductive energy is renormalized. For the SQUID modes the charging energies are renormalized and the free Hamiltonians read,

$$\begin{aligned} \tilde{\mathcal{H}}_+ &= \sum_j \tilde{\mathcal{H}}_{+;j} = \sum_j 4\frac{\tilde{E}_{C+;j}}{\hbar^2}\pi^2_{+;j} + E_L\phi^2_{+;j}, \\ \tilde{\mathcal{H}}_- &= \sum_j \tilde{\mathcal{H}}_{-;j} = \sum_j 4\frac{\tilde{E}_{C-;j}}{\hbar^2} + E_L\phi^2_{-;j} - E_J\cos(\phi_{ext;j})\cos(\phi_{-;j}), \end{aligned} \tag{4.27}$$

where $\tilde{E}_{C\pm;j} \equiv \tilde{E}_{C\pm;n,m} = E_{C\pm;n,m} + (E_{q;n,m} + E_{q;n,m+1} + E_{q;n+1,m} + E_{q;n+1,m+1})/4$. The Hamiltonian of qubit-qubit interactions only couples the neighbouring qubits along diagonals and has the form,

$$\tilde{\mathcal{H}}_{qI} = -2E_L\sum_{n,m}\phi_{q;n,m}\phi_{q;n,m+1}. \tag{4.28}$$

Finally the Hamiltonian for SQUID-qubit interactions is,

$$\begin{aligned} \tilde{\mathcal{H}}_{qS} = &- 4\sum_{n,m}\frac{E_{Cq;n,m}}{\hbar^2}\pi_{n,m}(\pi_{S-;n,m} + \pi_{S+;n,m}) \\ &+ E_J\sum_{n,m}\cos(\phi_{ext;j})\sin(\phi_{-;n,m})\phi_{q-;n,m} \\ &+ \frac{1}{2!}\frac{E_J}{2}\sum_{n,m}\sin(\phi_{ext;j})\cos(\phi_{-;n,m})\phi^2_{q-;n,m} \\ &- \frac{1}{3!}\frac{E_J}{4}\sum_{n,m}\sin(\phi_{ext;j})\sin(\phi_{-;n,m})\phi^3_{q-;n,m} \\ &- \frac{1}{4!}\frac{E_J}{8}\sum_{n,m}\sin(\phi_{ext;j})\cos(\phi_{-;n,m})\phi^4_{q-;n,m}, \end{aligned} \tag{4.29}$$

where,

$$\pi_{S\pm;n,m} = \pi_{\pm;n,m} \pm \pi_{\pm;n-1,m} + \pi_{\pm;n,m-1} \pm \pi_{\pm;n-1,m-1}. \tag{4.30}$$

$\pi_{S-;m,n}$ ($\pi_{S+;m,n}$) is the sum of momenta of the breathing (COM) modes associated with the four SQUIDs adjacent to a transmon at node (n,m). $\tilde{\mathcal{H}}_{qS}$ contains a linear capacitive part (first line in Eq. (4.29)) which couples these modes to the momentum of the transmon. The other terms in Eq. (4.29) describe a nonlinear coupling between the phase of the breathing mode and the sum of the four qubit phases of each cell.

4.5.2 Second quantized form of the non-interacting theory

The free Hamiltonian of the circuit reads,

$$\tilde{\mathcal{H}}_0 = \sum_j (\tilde{\mathcal{H}}_{q;j} + \tilde{\mathcal{H}}_{+;j} + \tilde{\mathcal{H}}_{-;j}). \tag{4.31}$$

It is quantized by introducing the creation and annihilation operators $a_j^\dagger$ and a_j for transmon j,

$$\phi_j = \overline{\phi}_j (a_j + a_j^\dagger), \quad \pi_j = -\frac{i\hbar}{2\overline{\phi}_j}(a_j - a_j^\dagger), \tag{4.32}$$

in which $\overline{\phi}_j$ is the zero-point fluctuation amplitude,

$$\overline{\phi}_j = \left(\frac{2E_{Cq;j}}{E_{Jq;j} + 4E_L} \right)^{1/4}. \tag{4.33}$$

The second quantized form of the transmon qubit at node j reads,

$$\tilde{\mathcal{H}}_{q;j} = \hbar\omega_j a_j^\dagger a_j + \hbar U a_j^\dagger a_j^\dagger a_j a_j, \tag{4.34}$$

where the transition frequency and nonlinearity are given as follows,

$$\hbar\omega_j = \sqrt{8E_{Cq;j}(E_{Jq;j} + 4E_L)}, \quad \hbar U_j = E_{Cq;j} \frac{E_{Jq;j}}{2E_{Jq;j} + 8E_L}. \tag{4.35}$$

The SQUID modes are in turn quantized by introducing ladder operators $(s^\dagger_{-;j}, s_{-;j})$ and $(s^\dagger_{+;j}, s_{+;j})$ for the breathing and COM modes respectively,

$$\tilde{\mathcal{H}}_{\pm;j} = \hbar\omega_\pm s^\dagger_{\pm;j} s_{\pm;j}. \tag{4.36}$$

The transition frequencies and zero-point fluctuations of these modes read,

$$\hbar\omega_\pm = 4\sqrt{\tilde{E}_{C\pm} E_L}, \quad \overline{\phi}_\pm = (\tilde{E}_{C\pm}/E_L)^{1/4}. \tag{4.37}$$

Comment on the truncation of the SW transformation Here we estimate the amplitude of the generator S of the SW transformation to justify truncating the expansion (4.24) to the fourth order in S. In terms of the zero-point fluctuations of the qubits and the SQUID modes this amplitude is given by,

$$||S|| = \frac{\overline{\phi}_j}{4\overline{\phi}_-}. \tag{4.38}$$

For our implementation, our typical parameters are $\overline{\phi}_j \lesssim 0.7$ and $\overline{\phi}_- \gtrsim 1.1$ therefore $||S|| \lesssim 0.3$. Note that in our approach the fourth-order is engineered to be the dominant term in the rotating frame of qubits, i.e. the strength of four-body terms are larger than the effective interaction strength of the other terms in expansion (4.24). This justifies the truncation of the effective Hamiltonian $\tilde{H}$ at fourth-order.

4.5.3 Adiabatic elimination of the SQUID modes

The SQUID's COM mode is a harmonic oscillator and its the frequency is determined by the parasitic capacitance C_g between the SQUID nodes and the ground, i.e. $\omega_+ \propto C_g^{-1/2}$. Since $C_J \gg C_g$, we expect that the frequency of the COM mode is at least one order of magnitude larger than the frequency of the breathing mode. For example if $C_g = 10^{-2}$fF [6], $C_J = 1$fF and the frequency of breathing mode is $\omega_- \sim 8$GHz then $\omega_+ \sim 80$GHz which is larger than the superconducting gap! Therefore to a very good approximation this mode is in its ground state $|0_+\rangle$.

---

[6] This is still rather a large value for the parasitic capacitance.

On the other hand the breathing mode is a nonlinear mode, c.f. Eq. (4.27). In our design, however, we take the following form for the external flux applied to the coupling SQUID of cell $[j]$,

$$\phi_{ext;j} = \phi_{dc} + \phi_{ac} F_j(t), \tag{4.39}$$

where $\phi_{dc} = \pi \gg \phi_{ac}$ and $F_j(t)$ is an oscillating function, which is chosen to trigger four-body interaction within a cell. We will discuss the specific form of this drive in the next section. The choice of ϕ_{dc} however suppresses the dc part of the critical current of the SQUID and hence the nonlinear contributions vanishes in the static Hamiltonian. This mode is then a harmonic oscillator which is perturbed by a driven nonlinear Hamiltonian.

By carefully choosing the parameters of the circuit, the breathing modes are detuned with respect to all possible processes that could generate excitations of these modes, e.g. driving on resonance via external modulation or interactions with adjacent qubits. For this reason the breathing modes can be approximated to remain in their corresponding ground states $|0_{-;j}\rangle$. While the breathing modes are adiabatically eliminated and hence do not define dynamical degrees of freedom in the circuit, they can still mediate interactions within their cells.

To the leading order of adiabatic elimination, the effective Hamiltonian is given by projecting the Hamiltonian (4.25) onto the ground states of the SQUID modes $|0_-, 0_+\rangle = \Pi_j |0_{-;j}, 0_{+;j}\rangle$.

$$\mathcal{H}^{(0)} = \langle 0_-, 0_+ | \tilde{\mathcal{H}} | 0_-, 0_+ \rangle \,. \tag{4.40}$$

We note that under this adiabatic elimination, the Hamiltonians of the SQUID modes ($\tilde{\mathcal{H}}_{\pm}$, c.f. Eq. (4.27)) give irrelevant constants. Moreover $\tilde{\mathcal{H}}_q$ and $\tilde{\mathcal{H}}_{qI}$ are unaffected, since they do not contain the SQUID modes. Therefore we get,

$$\mathcal{H}^{(0)} = \tilde{\mathcal{H}}_q + \tilde{\mathcal{H}}_{qI} + \tilde{\mathcal{H}}_{qS}^{(0)}, \tag{4.41}$$

where,

$$\begin{aligned}\tilde{\mathcal{H}}^{(0)}_{qS} &= \tilde{\mathcal{H}}^{(0)}_{qS,s} + \tilde{\mathcal{H}}^{(0)}_{qS,f},\\ \tilde{\mathcal{H}}^{(0)}_{qS,s} &= -\frac{1}{8}\tilde{E}_J F(t)\sum_j \phi^2_{q-;j},\\ \tilde{\mathcal{H}}^{(0)}_{qS,f} &= \frac{1}{16}\frac{1}{4!}\tilde{E}_J\sum_j \phi^4_{q-;j},\end{aligned} \tag{4.42}$$

with,

$$\chi = \chi_j = \exp\bigg(-\frac{\overline{\phi}_-^2}{2}\bigg), \quad \tilde{E}_J = \chi\phi_{ac}E_J. \tag{4.43}$$

In deriving Eq. (4.42), we have used the following matrix elements [7],

$$\begin{aligned}&\langle 0_{-;j}|\cos(\phi_{-;j})|0_{-;j}\rangle = \chi,\\ &\langle 0_{-;j}|\sin(\phi_{-;j})|0_{-;j}\rangle = 0,\\ &\langle 0_{-;j}|\pi_{-;j}|0_{-;j}\rangle = 0.\end{aligned} \tag{4.44}$$

The local leading order correction to the projected Hamiltonian (4.42) is given by second-order processes in which the breathing mode e.g. of cell $[j]$ is virtually excited to its first excited level $|1_{-;j}\rangle$, while the high-frequency COM-mode remains in the ground state. This local correction is proportional to,

$$\mathcal{H}_{corr;j} \propto \langle 0_-, 0_+|\tilde{\mathcal{H}}|1_{-;j}, 0_+\rangle\, \langle 1_{-;j}, 0_+|\tilde{\mathcal{H}}|0_-, 0_+\rangle\,. \tag{4.45}$$

We explicitly calculate the contribution of $\mathcal{H}_{corr;j}$ in Sec. 4.6.2, where we discuss perturbations and will conclude that it leads to frequency shifts of the transmons and the SQUID modes and therefore we can neglect it in the following discussions [8]. Here, we just identify the relevant Hamiltonian for a

---

[7] The zero-point fluctuation of the breathing mode ($\overline{\phi}_-$) is not necessarily smaller than 1, therefore we use the exact value rather than expanding and truncating in $\overline{\phi}_-$.

[8] The explicit form of $\mathcal{H}_{corr;j}$ depends on the detuning between the ground state and the virtual states. As the Hamiltonian is time-dependent, we cannot identify this detuning before introducing the explicit time-dependency of $F(t)$.

later reference. Note that the correction is non-zero if,

$$\langle 1_{-;j}, 0_{+;j}|\tilde{\mathcal{H}}|0_{-;j}, 0_{+;j}\rangle \neq 0. \tag{4.46}$$

By virtue of the relations,

$$\begin{aligned}
&\langle 1_{-;j}|\cos(\phi_{-;j})|0_{-;j}\rangle = 0,\\
&\langle 1_{-;j}|\sin(\phi_{-;j})|0_{-;j}\rangle = \chi\overline{\phi}_{-},\\
&\langle 1_{-;j}|\pi_{-;j}|0_{-;j}\rangle = \frac{i\hbar}{2\overline{\phi}_{-}},
\end{aligned} \tag{4.47}$$

we find that the relevant part of the Hamiltonian (4.29) for leading order corrections is,

$$\begin{aligned}
\tilde{\mathcal{H}}^{(1)}_{qS} =& -4\sum_j \frac{E_{Cq;j}}{\hbar^2}\pi_j \pi_{S-;j}\\
&+ E_J \sum_j \cos(\phi_{ext;j})\sin(\phi_{-;j})\phi_{q-;j}\\
&- \frac{1}{3!}E_J \sum_j \sin(\phi_{ext;j})\sin(\phi_{-;j})\phi^3_{q-;j}.
\end{aligned} \tag{4.48}$$

We can neglect the cubic term in $\mathcal{H}^{(1)}_{qS}$, since it is by a factor of $\overline{\phi}^2_j/24 \ll 1$ smaller than the linear term in $\phi_{q-;j}$ [9]. We thus find,

$$\begin{aligned}
\tilde{\mathcal{H}}^{(1)}_{qS} \approx& -4\sum_j \frac{E_{Cq;j}}{\hbar^2}\pi_j \pi_{S-;j}\\
&- \frac{1}{2}\tilde{E}_J F(t)\sum_j \phi_{-;j}\phi_{q-;j},
\end{aligned} \tag{4.49}$$

where we have approximated $\sin(\phi_{-;j}) \approx \frac{\chi}{\overline{\phi}_{-}}\phi_{-;j}$, in accordance with Eq. (4.47) and also used Eqs. (5.96) and (4.43).

---

[9] Note that the correction is yet second order in this Hamiltonian

4.6 Engineering the time-dependent Hamiltonian

We define $\mathcal{U}$ as a rotating frame in which the qubits and SQUID modes rotate at their corresponding frequencies,

$$\mathcal{U} = \exp\bigg(-\frac{i}{\hbar}\big(\tilde{\mathcal{H}}_q + \tilde{\mathcal{H}}_-\big)t\bigg). \tag{4.50}$$

In this rotating frame, the ladder operators of the qubits transform as follows,

$$\begin{aligned} a_j &\to a_j(t) = \mathcal{U}^\dagger a_j \mathcal{U} = e^{-i\omega_j t} a_j, \\ a_j^\dagger &\to a_j^\dagger(t) = \mathcal{U}^\dagger a_j^\dagger \mathcal{U} = e^{i\omega_j t} a_j^\dagger, \\ \phi_{q;j} &\to \phi_{q;j}(t) = \overline{\phi}_j\big(a_j(t) + a_j^\dagger(t)\big). \end{aligned} \tag{4.51}$$

For the breathing modes of SQUIDs, the transformation leads to the following substitutions [10],

$$\begin{aligned} s_{-;j} &\to s_{-;j}(t) = \mathcal{U}^\dagger s_{-;j} \mathcal{U} = e^{-i\omega_- t} s_{-;j}, \\ s_{-;j}^\dagger &\to s_{-;j}^\dagger(t) = \mathcal{U}^\dagger s_{-;j}^\dagger \mathcal{U} = e^{i\omega_- t} s_{-;j}^\dagger, \\ \phi_{-;j} &\to \phi_{-;j}(t) = \overline{\phi}_-\big(s_{-;j}(t) + s_{-;j}^\dagger(t)\big). \end{aligned} \tag{4.52}$$

The transformed Hamiltonian under $\mathcal{U}$ reads,

$$\mathcal{H}_{rot.} = \mathcal{U}^\dagger \mathcal{H}^{(0)} \mathcal{U} - \frac{i}{\hbar}\dot{\mathcal{U}}\mathcal{U} = \tilde{\mathcal{H}}_{qS}^{(0)}(t) + \tilde{\mathcal{H}}_{qI}(t), \tag{4.53}$$

where the two terms on the r.h.s., i.e. $\tilde{\mathcal{H}}_{qS}^{(0)}(t)$ and $\tilde{\mathcal{H}}_{qI}(t)$, are given by applying the substitutions (4.51) to the corresponding Hamiltonians $\tilde{\mathcal{H}}_{qS}^{(0)}$ and $\tilde{\mathcal{H}}_{qI}$, c.f. (4.42) and (4.28).

In the next section, we use the fourth-order term $\mathcal{H}_{qS,f}^{(0)}(t)$ contained in $\mathcal{H}_{qS}^{(0)}(t)$ (c.f. Eq. (4.42)) to engineer the toric code Hamiltonian in the rotating

---

[10] It might seem irrelevant to include the SQUID “ − ” mode in the definition of the rotating frame, as we eliminate this mode, however to deal with the corrections of the adiabatic elimination we should still retain this mode.

frame and will show by suitably driving the lattice we have,

$$\mathcal{H}^{(0)}_{qS,f}(t) \approx \mathcal{H}_{TC}, \tag{4.54}$$

which becomes the dominant part of the Hamiltonian $\mathcal{H}_{rot.}$ On the other hand the second-order term $\mathcal{H}^{(0)}_{qS,s}(t)$ and $\tilde{\mathcal{H}}_{qI}(t)$ are treated as perturbations to the toric code Hamiltonian in Sec. 4.6.2.

4.6.1 Generation of stabilizer interactions

In this section, we show how to generate the stabilizer interactions using the four-body terms in $\mathcal{H}^{(0)}_{qS,f}$. To simplify the explanation, we restrict the discussion to a single cell and label the indices of a typical unit cell as $(n, m) \to 1$, $(n+1, m) \to 2$, $(n+1, m+1) \to 3$ and $(n, m+1) \to 4$, see Fig. 4.4. The Hamiltonian $\mathcal{H}^{(0)}_{qS,f}$ for one cell can be split into two parts,

$$H_{cell} \equiv \mathcal{H}^{(0)}_{qS,f}\bigg|_{cell} = H_{\text{stb}} + H_{\text{pert}}, \tag{4.55}$$

where,

$$\begin{aligned} H_{\text{stb}} &= \frac{1}{16}\tilde{E}_J F(t)\phi_1(t)\phi_2(t)\phi_3(t)\phi_4(t), \\ H_{\text{pert}} &= -\tilde{E}_J F(t)\sum_{(ijkl)} C_{ijkl}\phi_i(t)\phi_j(t)\phi_k(t)\phi_l(t). \end{aligned} \tag{4.56}$$

Here the notation $\sum_{(ijkl)}$ means that at least two of the indices are the same. The coefficients C_{ijkl} have the values $C_{ijkl} = \pm 1/32$ for terms of the form $\phi_j^2\phi_k\phi_l$ with $j \neq k$, $j \neq l$ and $l \neq k$, $C_{ijkl} = \pm 1/64$ for terms of the form $\phi_j^2\phi_k^2$ with $j \neq k$, $C_{ijkl} = \pm 1/96$ for terms of the form $\phi_j^3\phi_k$ with $j \neq k$ and $C_{ijkl} = \pm 1/384$ for terms of the form ϕ_j^4.

Let us first consider H_{stb}. Due to the nonlinearity of the transmon qubits, we truncate the ladder operators associated with nodal modes to the two low-energy states and thus replace $a_i(a_i^\dagger)$ with $\sigma_i^-(\sigma_i^+)$. The nodal phases in the rotating frame read (c.f. Eq. (4.51)),

$$\phi_j(t) = \overline{\phi}_j(e^{-i\omega_j t}\sigma_j^- + e^{+i\omega_j t}\sigma_j^+). \tag{4.57}$$

Therefore $\phi_1(t)\phi_2(t)\phi_3(t)\phi_4(t)$ has 16 terms (8 terms plus their Hermitian conjugate) of the form $e^{i\nu_j t}\sigma_1^a\sigma_2^b\sigma_3^c\sigma_4^d$ with $j = 1...16$, where $\{a, b, c, d\} \in \{+, -\}$ and $\nu_j \equiv \nu(a, b, c, d) = a\omega_1 + b\omega_2 + c\omega_3 + d\omega_4$. These 16 terms and the corresponding rotating frequencies are listed in Tab. 4.1.

To generate the star and plaquette interactions we first notice that,

$$\sigma_j^x = \sigma_j^+ + \sigma_j^-, \quad \sigma_j^y = -i(\sigma_j^+ - \sigma_j^-). \tag{4.58}$$

Simple algebra tells us that the star interaction $\sigma_1^x\sigma_2^x\sigma_3^x\sigma_4^x$ is given by the sum of all terms listed in the table, while for the plaquette interaction $\sigma_1^y\sigma_2^y\sigma_3^y\sigma_4^y$ we need to sum all terms in the orange rows (i.e. with even number of σ_j^+) and subtract from that the sum of all terms in the blue rows (i.e. with odd number of σ_j^+).

	term	frequency		term	frequency
🟧 1	$\sigma_1^+\sigma_2^+\sigma_3^+\sigma_4^+$	$\nu_1 = \omega_1 + \omega_2 + \omega_3 + \omega_4$	🟧 9	$\sigma_1^-\sigma_2^-\sigma_3^-\sigma_4^-$	$-\nu_1$
🟧 2	$\sigma_1^+\sigma_2^+\sigma_3^-\sigma_4^-$	$\nu_6 = \omega_1 + \omega_2 - \omega_3 - \omega_4$	🟧 10	$\sigma_1^-\sigma_2^-\sigma_3^+\sigma_4^+$	$-\nu_6$
🟧 3	$\sigma_1^+\sigma_2^-\sigma_3^+\sigma_4^-$	$\nu_7 = \omega_1 - \omega_2 + \omega_3 - \omega_4$	🟧 11	$\sigma_1^-\sigma_2^+\sigma_3^-\sigma_4^+$	$-\nu_7$
🟧 4	$\sigma_1^-\sigma_2^+\sigma_3^-\sigma_4^+$	$\nu_8 = -\omega_1 + \omega_2 + \omega_3 - \omega_4$	🟧 12	$\sigma_1^+\sigma_2^-\sigma_3^-\sigma_4^+$	$-\nu_8$
🟦 5	$\sigma_1^+\sigma_2^+\sigma_3^+\sigma_4^-$	$\nu_2 = \omega_1 + \omega_2 + \omega_3 - \omega_4$	🟦 13	$\sigma_1^-\sigma_2^-\sigma_3^-\sigma_4^+$	$-\nu_2$
🟦 6	$\sigma_1^+\sigma_2^+\sigma_3^-\sigma_4^+$	$\nu_3 = \omega_1 + \omega_2 - \omega_3 + \omega_4$	🟦 14	$\sigma_1^-\sigma_2^-\sigma_3^+\sigma_4^-$	$-\nu_3$
🟦 7	$\sigma_1^+\sigma_2^-\sigma_3^+\sigma_4^+$	$\nu_4 = \omega_1 - \omega_2 + \omega_3 + \omega_4$	🟦 15	$\sigma_1^-\sigma_2^+\sigma_3^-\sigma_4^-$	$-\nu_4$
🟦 8	$\sigma_1^-\sigma_2^+\sigma_3^+\sigma_4^+$	$\nu_5 = -\omega_1 + \omega_2 + \omega_3 + \omega_4$	🟦 16	$\sigma_1^+\sigma_2^-\sigma_3^-\sigma_4^-$	$-\nu_5$

Table 4.1: All four-body terms contained in $H_{\rm stb}$ and their rotation frequencies in the frame defined by $\mathcal{U}$.

Motivated by this, we propose the following forms for time-dependent drive $F(t)$ which cancels out the rotation of each term and also takes care of the proper signs of the terms to generate a static star or plaquette term,

$$\begin{aligned} F_X(t) &= f_{1,1,1,1} + f_{1,1,-1,-1} + f_{1,-1,1,-1} + f_{-1,1,1,-1}, \\ F_Y(t) &= f_{1,1,1,-1} + f_{1,1,-1,1} + f_{1,-1,1,1} + f_{-1,1,1,1}, \end{aligned} \tag{4.59}$$

where $f_{a,b,c,d} = \cos\big[(a\omega_1 + b\omega_2 + c\omega_3 + d\omega_4)t\big]$. Each of the four terms in F_X brings one orange term and its H.c. into resonance, i.e. makes those terms non-rotating. Likewise each term in F_Y takes care of the blue four-body terms to cancel out their rotating prefactor $e^{i\nu_j t}$.

Note that each term in F_X or F_Y acts on all 16 terms, however the parameters are chosen such that apart from the two non-rotating terms, all other 14 terms become rotating. As the strength of these four-body terms are weak ($\sim 1-2$ MHZ), even with a small rotating prefactor those 14 terms are discarded under a rotating wave approximation (RWA). For our parameters, the rotation frequencies are $\sim$ 0.4 GHz so neglecting the rotating terms under RWA are well justified. A similar argument applies to H_{pert}: The individual contributions in H_{pert} are at least by a factor of 1/2 smaller than H_{stb}. On the other hand, the terms in this Hamiltonian have the same frequency as rotating two-body terms. We will consider the requirements for the two-body terms to be fast-rotating in the next section. As the strengths of the terms in H_{pert} (at most$\sim$ 0.5MHz) are much smaller than the two-body terms, we can neglect this Hamiltonian as well.

It is now easily verified that an external oscillating field $F_s = F_X + F_Y$ gives rise to a star term and a field F_p leads to a plaquette term,

$$\begin{aligned} H_{\text{stb}}\big|_{F=F_s} &\approx J_s \sigma_1^x \sigma_2^x \sigma_3^x \sigma_4^x, \\ H_{\text{stb}}\big|_{F=F_p} &\approx J_p \sigma_1^y \sigma_2^y \sigma_3^y \sigma_4^y. \end{aligned} \tag{4.60}$$

The strength of these terms reads,

$$J_s = J_p = \frac{1}{16}\tilde{E}_J \Pi_{j=1}^4 \overline{\phi}_j. \tag{4.61}$$

In addition to the engineered stabilizer terms there are a number of spurious terms with a wide range of interaction strength, from strong two-body interactions to weak fourth-order terms. While we have argued that the third-order terms (from adiabatic elimination) and fourth-order terms (e.g. in H_{pert}) are negligible, we are still to determine the effect of unsought second-order terms. We now turn to this discussion in the following section.

4.6.2 Perturbations

In the previous sections, we started from the Hamiltonian of the circuit and showed that by modulating lattice cells via driving fields $F_s(t)$ and $F_p(t)$, one can engineer the toric code Hamiltonian. Along the way, we also encountered several sources of second-order perturbations:

1. Inductive couplings between nearest-neighbors along the diagonals, $\mathcal{H}_{Iq}$, c.f. Eq. (4.28).
2. Qubit-qubit interactions within a cell mediated by the SQUIDs, $\mathcal{H}_{qS}^{(0)}$, c.f. Eq. (4.42).
3. Leading-order corrections to the adiabatic elimination due to $\mathcal{H}_{qS}^{(1)}$, c.f. Eq. (4.49).

The Hamiltonian of the circuit can then be written in a compact form as follows,

$$\mathcal{H}_{rot.} = \mathcal{H}_{TC} + \sum_{\alpha} \hbar h_\alpha e^{i\Omega_\alpha t}, \tag{4.62}$$

where $\mathcal{H}_{TC}$ is the engineered toric code Hamiltonian and h_α accounts for perturbation terms which rotate at Ω_α in the rotating frame. Here h_α is time-independent and all time-dependency of a perturbation term - including the rotating frequency of the operator and possibly the oscillating field $F(t)$ - is encapsulated in $e^{i\Omega_\alpha t}$. As $\mathcal{H}_{rot.}$ is Hermitian, both $\Omega_\alpha > 0$ and $\Omega_\alpha < 0$ contribute in Eq. (4.62). To validate treating h_α as a perturbation, we also require that $||h_\alpha|| \ll \Omega_\alpha$. Following approaches outlined in the [120–122], the dynamics generated in this regime can be approximated by a time-independent Hamiltonian as an expansion in powers of interaction strength over oscillation frequency,

$$H_{eff} = H_{eff,0} + H_{eff,1} + H_{eff,2} + H_{eff,3} + ... \tag{4.63}$$

where,

$$H_{eff,0} = \mathcal{H}_{TC}, \tag{4.64a}$$

$$H_{eff,1} = \sum_{\alpha,\beta} \frac{\delta(\Omega_\alpha + \Omega_\beta)}{2\Omega_\alpha}[h_\alpha, h_\beta], \tag{4.64b}$$

$$H_{eff,2} = \sum_{\alpha,\beta} \frac{\delta(\Omega_\alpha + \Omega_\beta)}{2\Omega_\alpha\Omega_\beta}[[\mathcal{H}_{TC}, h_\alpha], h_\beta] + \sum_{\alpha,\beta,\gamma} \frac{\delta(\Omega_\alpha + \Omega_\beta + \Omega_\gamma)}{3\Omega_\beta\Omega_\gamma}[[h_\alpha, h_\beta], h_\gamma], \tag{4.64c}$$

$$H_{eff,3} = \sum_{\alpha,\beta,\gamma} \frac{\delta(\Omega_\alpha + \Omega_\beta + \Omega_\gamma)}{3\Omega_\alpha\Omega_\beta\Omega_\gamma}[[[\mathcal{H}_{TC}, h_\alpha], h_\beta], h_\gamma] + \sum_{\alpha,\beta,\gamma,\kappa} \frac{\delta(\Omega_\alpha + \Omega_\beta + \Omega_\gamma + \Omega_\kappa)}{4\Omega_\beta\Omega_\gamma\Omega_\kappa}[[[h_\alpha, h_\beta], h_\gamma], h_\kappa] \tag{4.64d}$$

and $\delta(\Omega)$ is the Dirac delta-function. Since $||h_\alpha|| \ll \Omega_\alpha$, the terms in $H_{eff,2}$ and $H_{eff,3}$ which include $\mathcal{H}_{TC}$ are at least two orders of magnitude smaller than $\mathcal{H}_{TC}$ as they contain two or more h_α and can thus be discarded. We now discuss the other perturbative terms in the following. Since there are several types of perturbations, we replace α in Eq. (4.62) by a composite index and denote the perturbations by $h_\alpha \equiv h_{T;n,m}$ or $h_\alpha \equiv h_{T;j,l}$ where T indicates the type of a perturbation and n, m, j, l denote the qubits involved in that perturbation. As for derivations, we will come across the following commutation relations in many cases,

$$[a_i a_j^\dagger, a_i^\dagger a_j] = (1 - \delta_{i,j})(a_j^\dagger a_j - a_i^\dagger a_i), \tag{4.65a}$$

$$[a_i a_j, a_i^\dagger a_j^\dagger] = (1 + \delta_{i,j})(a_j^\dagger a_j + a_i^\dagger a_i + 1), \tag{4.65b}$$

$$[a_i a_j, a_i a_j^\dagger] = (1 + \delta_{i,j}) a_j a_j, , \tag{4.65c}$$

$$[a_i a_j^\dagger, a_i^\dagger a_j^\dagger] = (1 + \delta_{i,j}) a_j^\dagger a_i^\dagger, . \tag{4.65d}$$

$$\tag{4.65e}$$

4.6.3 Perturbations in $\mathcal{H}_{Iq}$

The Hamiltonian $\mathcal{H}_{Iq}$ describes the residual inductive coupling between two transmons on a diagonal. In the rotating frame $\mathcal{U}$, this Hamiltonian reads (c.f. Eqs. (4.28) and (4.53)),

$$\mathcal{H}_{Iq}(t) = \sum_{n,m} \big(h_{1;n,m} e^{i\Omega_{1;n,m}t} + h_{2;n,m} e^{i\Omega_{2;n,m}t} + \text{H.c.}\big), \tag{4.66}$$

where,

$$\begin{aligned} h_{1;n,m} &= -2E_L \overline{\phi}_{n,m} \overline{\phi}_{n,m+1} a^\dagger_{n,m} a_{n,m+1}, \quad & \Omega_{1;n,m} &= \omega_{n,m} - \omega_{n,m+1}, \\ h_{2;n,m} &= -2E_L \overline{\phi}_{n,m} \overline{\phi}_{n,m+1} a^\dagger_{n,m} a^\dagger_{n,m+1}, \quad & \Omega_{2;n,m} &= \omega_{n,m} + \omega_{n,m+1}. \end{aligned} \tag{4.67}$$

$h_{2;n,m}$ describes a squeezing process in the absence of any driving. We can simply drop this term since $||h_{2;n,m}|| \lll \Omega_{2;n,m}$. For the hopping terms, we require that $||h_{1;n,m}|| \ll \Omega_{1;n,m}$, i.e. nearest neighbors on a diagonal should be sufficiently detuned such that the residual inductive coupling is ineffective. According to Eq. (4.64b), the hopping term $h_{1;n,m}$ leads to a frequency shift $\Delta^1_{(n,m)}$ of the transmon at node (n, m) due to non-zero commutators $[h_{1;n,m}, h^\dagger_{1;n,m}]$ and $[h_{1;n,m-1}, h^\dagger_{1;n,m-1}]$. This frequency shift explicitly reads,

$$\Delta^{(1)}_{(n,m)} = \frac{4E_L^2 \overline{\phi}^2_{n,m} \overline{\phi}^2_{n,m+1}}{\hbar^2(\omega_{n,m} - \omega_{n,m-1})} + \frac{4E_L^2 \overline{\phi}^2_{n,m} \overline{\phi}^2_{n,m-1}}{\hbar^2(\omega_{n,m} - \omega_{n,m-1})} \tag{4.68}$$

Furthermore on a diagonal n, the transmon (n, m) can mediate interaction between its nearest-neighbors, transmons $(n, m-1)$ and $(n, m+1)$, through a second-order interaction due to a commutator $[h_{1;n,m-1}, h^\dagger_{1;n,m}]$, the strength of which is $\sim \Delta_1/2$. Therefore to suppress long-range hoppings, we require that the next-nearest neighbors on a diagonal are detuned at least by one order of magnitude larger than $\Delta_1/2$. Note that the detuning between next-next -nearest neighbors e.g. $(n, m-1)$ and $(n, m+2)$ is of the order of the detuning between nearest neighbors, which means that the hopping between them is strongly suppressed as well.

4.6.4 Perturbations in $\mathcal{H}^{(0)}_{qS,s}$

The Hamiltonian $\mathcal{H}^{(0)}_{qS,s}$ is defined in Eq. (4.42). For simplicity, we just write the Hamiltonian for one unit cell and again use the notation $(n, m) \to 1$, $(n + 1, m) \to 2$, $(n + 1, m + 1) \to 3$ and $(n, m + 1) \to 4$, see Fig. 4.4. In the rotating frame this Hamiltonian reads,

$$\begin{aligned} \mathcal{H}^{(0)}_{qS,s}(t)\bigg|_{cell} = \sum_{k=1}^{8}\sum_{j,l=1}^{4} & h_{3;jl}e^{i\Omega^{(+)}_{3;jlk}t} + h_{3;jl}e^{i\Omega^{(-)}_{3;jlk}t} \\ & + h_{4;jl}e^{i\Omega^{(+)}_{4;jlk}t} + h_{4;jl}e^{i\Omega^{(-)}_{4;jlk}t} + \text{H.c.}, \end{aligned} \tag{4.69}$$

where,

$$\begin{aligned} h_{3;jl} &= \pm\frac{\tilde{E}_J\overline{\phi}_j\overline{\phi}_l}{8}a^\dagger_j a_l, \quad \Omega^{(\pm)}_{3;jlk} = \omega_j - \omega_l \pm \nu_k, \\ h_{4;jl} &= \pm\frac{\tilde{E}_J\overline{\phi}_j\overline{\phi}_l}{8}a^\dagger_j a^\dagger_l, \quad \Omega^{(\pm)}_{4;jlk} = \omega_j + \omega_l \pm \nu_k. \end{aligned} \tag{4.70}$$

In the definition for $h_{3;jl}$ and $h_{4;jl}$, the "$-$" sign is relevant for $(j, l) = (1, 4)$ or $(2, 3)$ and the "+" is relevant otherwise. For this Hamiltonian the perturbation theory is applicable if,

$$\left|\frac{\tilde{E}_J\phi_j\phi_l}{8\hbar\Omega^{(\pm)}_{d;jlk}}\right| \ll 1 \quad \text{for } d = 3, 4. \tag{4.71}$$

Under this condition, the second-order term of the effective Hamiltonian gives a frequency shift of the transmon at node j which explicitly reads,

$$\begin{aligned} \Delta^{(2)}_j = & -\frac{\tilde{E}_J^2}{32}\sum_{[c]\in\mathcal{N}_j}\sum_{l\in[c]}\sum_{k_c=1}^{8}\overline{\phi}_j^2\overline{\phi}_l^2\frac{\omega_j+\omega_l}{\Omega^+_{3;jlk_c}\Omega^-_{3;jlk_c}} \\ & + \frac{\tilde{E}_J^2}{32}\sum_{[c]\in\mathcal{N}_j}\sum_{l\in[c]}\sum_{k_c=1}^{8}\overline{\phi}_j^2\overline{\phi}_l^2\frac{\omega_j-\omega_l}{\Omega^+_{4;jlk_c}\Omega^-_{4;jlk_c}}. \end{aligned} \tag{4.72}$$

Here $\mathcal{N}_j$ refers to the four neighboring cells of the transmon at j, hence $\sum_{[c]}$ runs over those cells, $\sum_{l\in[c]}$ denotes the sum over transmons of the cell $[c]$

including j, and k_c enumerates the 8 frequency components applied to cell $[c]$. Transmons that are shared by multiple cells should be counted once per cell (i.e. multiple times). For example j is counted four times since it appears in all its four neighboring cells.

4.6.5 Corrections to adiabatic elimination: perturbations from $\mathcal{H}_{qS}^{(1)}$

There are corrections to the adiabatic elimination process due to the Hamiltonian $\mathcal{H}_{qS}^{(1)}$ defined in Eq. (4.49),

$$\begin{aligned}\tilde{\mathcal{H}}_{qS}^{(1)} \approx &-4\sum_j \frac{E_{Cq;j}}{\hbar^2}\pi_j\pi_{S-;j}\\ &-\frac{1}{2}\tilde{E}_J F(t)\sum_j \phi_{-;j}\phi_{q-;j}.\end{aligned} \tag{4.73}$$

This Hamiltonian contains two contributions: The capacitive coupling of a transmon to the breathing mode of the four adjacent cells (denoted by $\mathcal{H}_{cap}$) and a Josephson coupling of the breathing mode of a cell to all transmons of that cell (denoted by $\mathcal{H}_{Jos.}$). For these two Hamiltonians, we derive the effective contribution based on the perturbation theory and then project the result to the ground state of the SQUID modes, $\langle 0_-|\mathcal{H}_{eff}|0_-\rangle$.

Capacitive coupling between breathing mode and transmon

In the rotating frame of the qubits and SQUID mode the capacitive part of the Hamiltonian reads,

$$\mathcal{H}_{cap} = \sum_j \sum_{[l]\in\mathcal{N}(j)} h_{5;jl}e^{i\Omega_{5;j}t} + h_{6;jl}e^{i\Omega_{6;j}t} + \text{H.c.}, \tag{4.74}$$

where again $\mathcal{N}(j)$ refers to the four adjacent cells of a transmon j, $\sum_{[l]}$ runs over the cells adjacent to the transmon j and the Hamiltonian couples the breathing mode of cell $[l]$ to the transmons as follows,

$$\begin{aligned} h_{5;j,l} &= -\frac{E_{Cq;j}}{\hbar^2} a_j^\dagger s_{-;l}, \quad \Omega_{5;j} = \omega_j - \omega_-, \\ h_{6;j,l} &= -\frac{E_{Cq;j}}{\hbar^2} a_j^\dagger s_{-;l}^\dagger, \quad \Omega_{6;j} = \omega_j + \omega_-, \end{aligned} \tag{4.75}$$

where $(s_{-;l}, s_{-,l}^\dagger$ are the ladder operators of the SQUID mode in $[l]$ and $\omega_-)$ is its frequency. To be eligible to apply the perturbation theory, we require,

$$\left| \frac{\tilde{E}_{Cq;j}}{\hbar \Omega_{d;j} \overline{\phi}_j \overline{\phi}_-} \right| \ll 1, \quad d = 5, 6. \tag{4.76}$$

With this assumption, $\mathcal{H}_{cap}$ gives rise to a frequency shift of the transmon as,

$$\Delta_j^{(3)} = \frac{4E_{Cq;j}}{\hbar^2(\omega_j - \omega_-)\overline{\phi}_j^2 \overline{\phi}_-^2} + \frac{4E_{Cq;j}}{\hbar^2(\omega_- + \omega_j)\overline{\phi}_j^2 \overline{\phi}_-^2}. \tag{4.77}$$

There are other possible second-order processes constructed from commutators like $[h_{5;j,l}, h_{5;k,l}^\dagger]$ in which the SQUID of a cell mediates hopping interaction[11] between two transmons of the cell. For our parameters, these processes have a strength of ∼ 70MHz, but nearest-neighbor transmons of a cell are detuned by at least 700MHz.

Physically the third order processes (contained in $\mathcal{H}_{eff,2}$) describe hoppings between transmons and a nearest/next-nearest neighbor SQUIDs. Each hopping process is mediated by one SQUID and one transmon and always includes a single $s_-/s_-^\dagger$. Therefore for these hoppings we have,

$$\langle 0_- | \mathcal{H}_{eff,2} | 0_- \rangle = 0. \tag{4.78}$$

In the same way that second-order processes generate hopping interactions between the transmons of a cell, fourth order processes (in $\mathcal{H}_{eff,3}$) could cause hoppings between two transmons of neighboring cells (next-nearest neighbors). These interactions have a strength of ∼ 0.5MHz and therefore it is ineffective due to the detuning between next-nearest transmons which is ∼ 100MHz.

---

[11] There are squeezing processes a well, but they are strongly suppressed since the coupling is second-order or higher.

Residual Josephson coupling in $\mathcal{H}_{qS}^{(1)}$

The second contribution in the Hamiltonian (4.49) is a Josephson coupling between a transmon and the SQUID which explicitly reads,

$$\begin{aligned}\mathcal{H}_J = \sum_j \sum_{[l]\in\mathcal{N}(j)} \sum_{k_l=1}^{8} \Big(& h_{7;jl} e^{i\Omega^{(+)}_{7;jk_l} t} + h_{7;j,l} e^{i\Omega^{(-)}_{7;jk_l} t} \\ & + h_{8;jl} e^{i\Omega^{(+)}_{8;jk_l} t} + h_{8;jlk_l} e^{i\Omega^{(-)}_{8;jk_l} t} + \text{H.c.} \Big),\end{aligned} \tag{4.79}$$

where,

$$\begin{aligned} h_{7;jl} &= \frac{\tilde{E}_J}{2} \overline{\phi}_j \overline{\phi}_- a_j^\dagger s_{-;l}, \quad \Omega^{(\pm)}_{7;jk} = \omega_j - \omega_- \pm \nu_k, \\ h_{8;jl} &= \frac{\tilde{E}_J}{2} \overline{\phi}_j \overline{\phi}_- a_j^\dagger s_{-;l}^\dagger, \quad \Omega^{(\pm)}_{8;jk} = \omega_j + \omega_- \pm \nu_k. \end{aligned} \tag{4.80}$$

In Eq. (4.79), k_l runs over the frequency components of the drive applied to the cell $[l]$. Analogous to the discussion we had so far, we can treat this Hamiltonian as a perturbation if,

$$\left| \frac{\tilde{E}_J \overline{\phi}_j \overline{\phi}_-}{2\hbar \Omega^{(\pm)}_{d;jk}} \right| \ll 1, \quad d = 7, 8. \tag{4.81}$$

Under this condition, the Hamiltonian (4.79) leads to the following frequency shift on a typical transmon,

$$\Delta_j^{(4)} = \frac{\tilde{E}_J^2 \overline{\phi}_j^2 \overline{\phi}_-^2}{\hbar^2} \sum_{k=1}^{8} \left[\frac{\Omega^{(+)}_{7;jk} + \Omega^{(-)}_{7;jk}}{\Omega^{(+)}_{7;jk} \Omega^{(-)}_{7;jk}} + \frac{\Omega^{(+)}_{8;jk} + \Omega^{(-)}_{8;jk}}{\Omega^{(+)}_{8;jk} \Omega^{(-)}_{8;jk}} \right]. \tag{4.82}$$

We can then conclude that the effect of perturbations leads to local frequency shifts of the transmon qubits. Collecting all terms from Eqs. (4.68), (4.72), (4.77) and (4.82), we get an overall frequency shift for the transmon at node j as,

$$\Delta_j = \Delta_j^{(1)} + \Delta_j^{(2)} + \Delta_j^{(3)} + \Delta_j^{(4)}. \tag{4.83}$$

4.7 Towards experimental implementation

In this section, we discuss the details of a realistic implementation of the toric code based on an eight-qubit lattice. The lattice for a minimal realization of the model on a torus is shown in Fig. 4.5, where the numbering refers to eight transmons and the coloring indicates different transition frequencies of the transmons. The qubits with different filling colors are mutually detuned at least by ~ 600MHz. The qubits with the same fillings but different frame colors (e.g. qubits 3 and 8) are detuned by ~ 100MHz with respect to each other to suppress next-nearest neighbor interactions. Therefore we can identify four principal transition frequencies (e.g. 1, 3, 4 and 5) and four others (2, 6, 7 and 8) which are slightly (~ 100MHz) detuned from the principal ones. A working example for the transition frequencies is presented in Tab. 4.2. One possible approach to choose this frequency pattern is as follows: We first fix the detunings between qubits and their next-nearest neighbors (with different frame colors in Fig. 4.5). With these, we just need to determine the four principal frequencies (filling colors in Fig. 4.5) and from those the other four frequencies are deduced. We then run a code over the four principal transition frequencies of transmons in the frequency range $3-15$GHz in steps of 100MHz. For each set of frequencies, we construct the drive frequencies for all cells and check whether the set of driving frequencies results in an unwanted resonant process inside a cell or between adjacent cells. A set of transition frequencies is acceptable if the rotating frequencies of all unwanted interactions are much larger (e.g. at least one order of magnitude) than the corresponding interaction strengths.

For the given example the Josephson energies of the transmon qubits vary between $E_{Jq,j} \approx h \times 4.9$GHz and $E_{Jq,j} \approx h \times 94$GHz which can be controlled via the dc-flux bias point of the qubits. The capacitances of the qubits lie in the range 50 fF $\leq C_{q;j} \leq$ 75 fF. For the coupling SQUID, we choose a Josephson energy $E_J \sim h \times 10$ GHz and a capacitance $C_J \sim 3.5$ fF. The transition frequency of the SQUID " $-$ " mode is $\omega_-/(2\pi) \sim 8.5$ GHz. For the coupling inductors it is required that they should be large enough so the resulting coupling terms are weak compared to the nonlinearities of the qubits and a

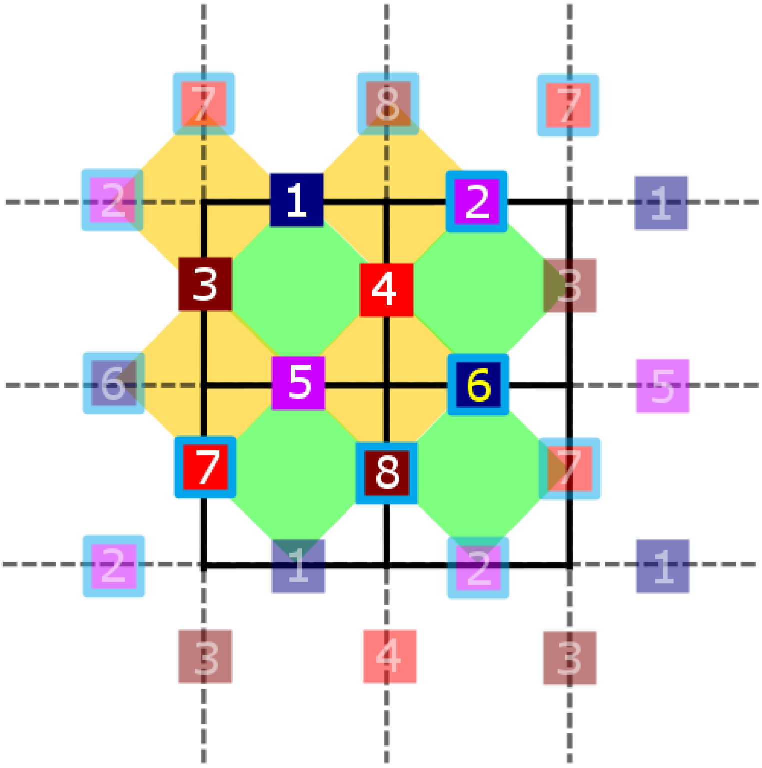

Figure 4.5: A minimal toric code lattice where the eight qubits are labelled by numbers. Four colors of qubits 1, 3, 4 and 5 show the principal qubit frequencies. The qubit pairs (1,6), (4,7), (5,2) and (3,8) are slightly ($\sim$ 100MHz) detuned to suppress next-nearest neighbor interactions. This detuning is indicated by the border color. The blurred repetition of a number shows periodic boundary condition.

truncation to the lowest two-states is valid. We therefore choose inductances of about 100 nH, which can be built from superinductors [123, 124] or using high inductance superconducting nanowires [125]. For an oscillating field amplitude $\phi_{ac} = 0.1$, we get a stabilizer interaction strength of $\sim$ 1 MHz, which is at least one order of magnitude larger than the typical dissipation rates of transmon qubits.

For these parameters, except for the four-body terms which contribute to building stabilizers, all other terms become rotating. In particular, for all

Qubit	Transition frequency $\omega_j/(2\pi)$	Qubit	Transition frequency $\omega_j/(2\pi)$
1	13.8 GHz	5	13.1 GHz
2	13.0 GHz	6	13.7 GHz
3	3.5 GHz	7	4.2 GHz
4	4.1 GHz	8	3.4 GHz

Table 4.2: An example of the transition frequencies of eight transmons (in natural frequency units) in a minimal lattice implementation of the toric code.

remaining two-body terms, the total oscillation frequency is at least $10-30$ times larger than the corresponding coupling strength. As we discussed in the previous section, to leading order, these terms give rise to frequency shifts of the qubits which can be compensated for by a modification of the drive frequencies [12]. All interaction terms contained in higher-order corrections are negligible compared to the four-body interactions forming the stabilizers.

The toric code can also be simulated on larger lattices as shown in Fig. 4.6. For a generic lattice, one needs 16 different transition frequencies for the qubits shown in the gray diamond in the figure. This set of frequencies is periodically repeated in both directions. Similar to the eight qubit lattice, one again needs 4 principal transition frequencies which are largely detuned with respect to each other to suppress strong nearest-neighbor interactions. These principal frequencies are indicated by different filling colors (blue, brown, red and purple) in the figure. The other 12 frequencies are detuned from the principal ones by ~ 100 MHz to ensure that there are no effective interactions between next-nearest neighbors. Different detunings are indicated by different colored frames (orange, green and light blue) in Fig. 4.6. Using this pattern of frequencies, all unwanted interactions between the qubits are suppressed. Note that the long-range interaction between two qubits with a same transition frequency (e.g two red squares) is much smaller than the star and plaquette interactions and hence can be safely neglected.

---

[12] Note that these frequency shifts are also reabsorbed in the definition of the rotating frame

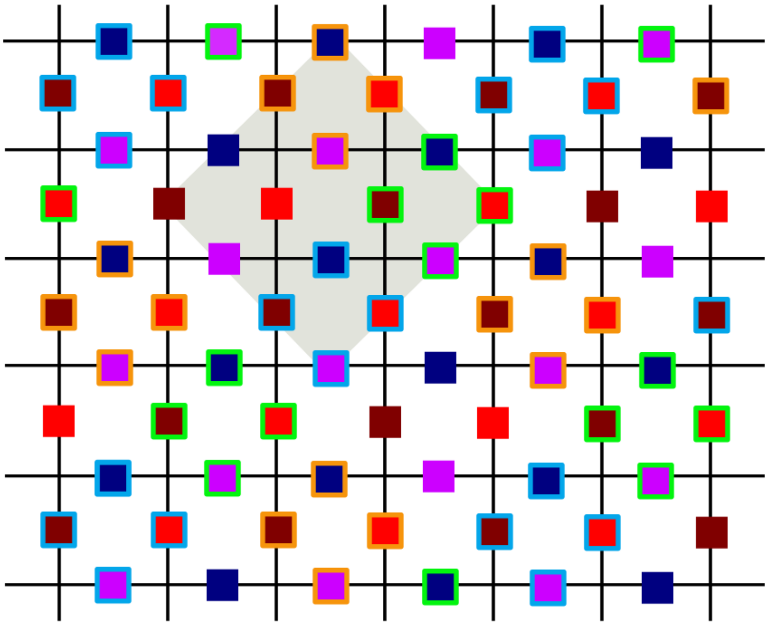

Figure 4.6: Transition frequency pattern for an arbitrary large lattice. It includes 16 different transition frequencies highlighted by the gray diamond which is repeated throughout the lattice. The diamond includes 4 principal frequencies (indicated by 4 filling colors) and 12 frequencies which are slightly detuned from the principal ones (indicated by frame colors). This choice for the frequency pattern ensures that interactions between next-nearest qubits are negligible.

4.8 Adiabatic preparation of topological order

The ground state of the toric code model on a torus is a four-fold degenerate topologically ordered manifold, denoted by $|\Psi_\alpha\rangle$, for $\alpha = 1, ..., 4$. A state inside this manifold can be prepared either through a measurement-based state preparation scheme [126] or via an adiabatic sweep from an initial trivial state, e.g. a product state [127]. In this section, we adapt the adiabatic approach proposed in [127] for our circuit. In our approach, we start from the ground state of the circuit when the external oscillating fluxes are turned off, i.e. $\phi_{ac} = 0$. In the absence of driving, we expect that there is no thermal excitations due to the cryogenic enviroment and thus all transmons are in their ground state. The initial state of the circuit is a product state $|\Psi_{in}\rangle = \Pi_j |0_j\rangle$, where

$|0_j\rangle$ is the ground state of a single transmon at j. Furthermore, the transition frequencies of the transmons are initially blue-detuned with respect to their final values, ω_j. This initial detuning is denoted by Δ.

The adiabatic sweep involves two simultaneous processes:

1. The amplitudes of the oscillating fields are gradually increased from zero to their final value (e.g. $\phi_{ac} = 0.1$) according to $\phi_{ac}(t) = \lambda(t)\phi_{ac}$,
2. The detuning of the transmons are decreased from Δ to zero according to $\Delta_j(t) = \Delta(1 - \lambda(t))$.

Here $\lambda(t)$ is a function that controls the process of adiabatic sweep and has fixed initial and final values $\lambda(t = 0) = 0$ and $\lambda(t = T_S) = 1$, where T_S is the duration of the process. In our scheme, $\lambda(t)$ is defined as $\lambda(t) = (1 + \zeta)(t/T_s)^6/(1 + \zeta(t/T_s)^6)$ with $\zeta = 100$.

The Hamiltonian for the adiabatic process is written as follows,

$$\mathcal{H}(\lambda) = \sum_j (1-\lambda)\frac{\Delta}{2}\sigma_j^z - \lambda\left(J_s\sum_s A_s + J_p\sum_p B_p\right) \tag{4.84}$$

At $t = 0$, the Hamiltonian reads $\mathcal{H}(\lambda = 0) = \sum_j \frac{\Delta}{2}\sigma_j^z$ which has a unique ground state $|\Psi_{in}\rangle$, i.e. the vacuum with no excitations. The final Hamiltonian at $t = T_S$ is the targeted toric code Hamiltonian $\mathcal{H}(\lambda = 1) = \mathcal{H}_{TC}$, c.f. Eq. (4.5).

The eigenvalues of an eight-qubit toric code as a function of tuning parameter λ is sketched in Fig. 4.7. For this lattice, there is a finite gap of size $\sim J_p, J_s$ for every λ.

To test the validity and fidelity of the adiabatic preparation, we numerically simulate the dynamics of the model, including qubit dissipative and dephasing processes, which is described by the following master equation,

$$\dot{\rho} = \frac{-i}{\hbar}[\mathcal{H}(\lambda), \rho] + \mathcal{D}_r[\rho] + \mathcal{D}_d[\rho]. \tag{4.85}$$

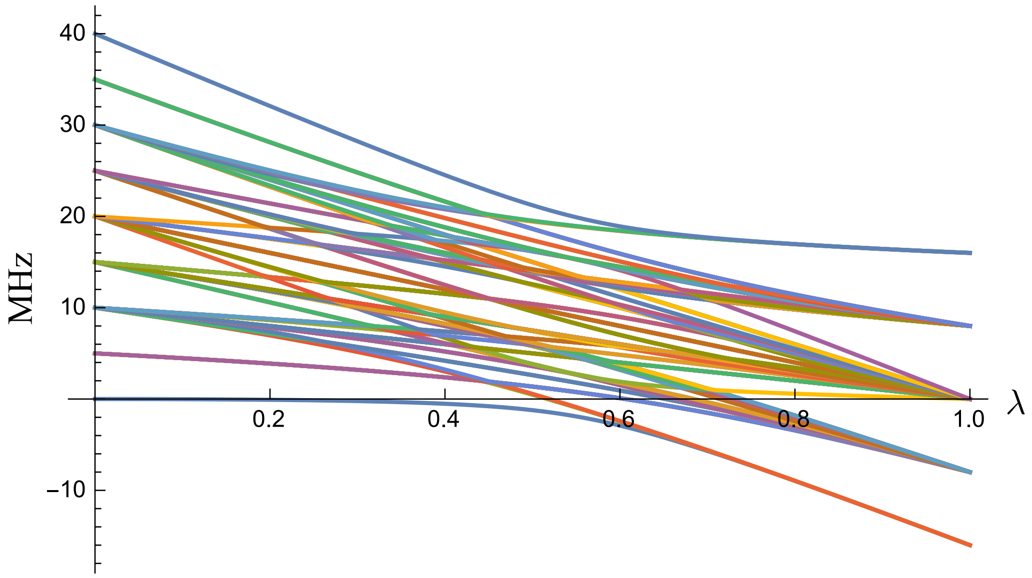

Figure 4.7: Spectrum of the Hamiltonian (4.84) for the eight-qubit lattice as a function of λ ($\Delta = 5$ MHz).

Here ρ is the density matrix of the circuit,

$$\mathcal{D}_r[\rho] = (\kappa/2) \sum_j \left(2\sigma_j^- \rho \sigma_j^+ - \sigma_j^+ \sigma_j^- \rho - \rho \sigma_j^+ \sigma_j^-\right), \tag{4.86}$$

accounts for qubit relaxation processes at a rate κ and

$$\mathcal{D}_d[\rho] = \kappa_d \sum_j \left(2\sigma_j^z \rho \sigma_j^z - \rho\right), \tag{4.87}$$

describes dephasing processes at a rate κ_d. Note that $\mathcal{D}_r[\rho]$ and $\mathcal{D}_d[\rho]$ are invariant under transformation to the rotating frame of the qubits. The fidelity F of preparing the state in the topologically-ordered manifold at time $t = T_S$ is defined as,

$$F = \sum_{\alpha=1}^{4} \langle \Psi_\alpha | \rho(T_S) | \Psi_\alpha \rangle \,. \tag{4.88}$$

Moreover, we also define a purity measure $P = \mathrm{Tr}(\rho^2)$ to quantify the effect of unavoidable dissipative processes on the purity of the prepared state. The results for F and P as a function of preparation time T_S and initial detuning

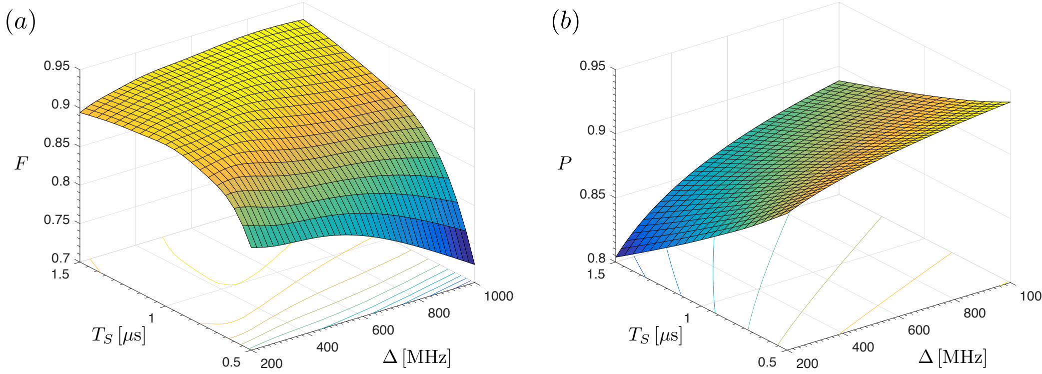

Figure 4.8: Fidelity and purity of the adiabatic preparation of the ground state as a function of intitial detuning Δ and preparation time T_S.

Δ are shown in Fig. 4.8, where we have taken the following values for the parameters: $J_s = J_p = 2$ MHz, $T_1 = \kappa^{-1} = 50\mu$s and $T_2 = \kappa_d^{-1} = 50\mu$s. As we stated in the introduction, the topological protection is not resilient to dissipation since the fidelity of preparation diminishes at longer times. The prepared topologically-ordered state cannot be used as a quantum memory with a long lifetime. Note that here the aim is to demonstrate the preparation of the topologically-ordered state of photons and for that reason it is enough to prepare one of the states inside the degenerate manifold as the four states are equivalent. Therefore it doesn't matter which of them or which superposition one prepares and we just tested whether the adiabatic sweep ends up in the ground state manifold. However, after preparation, we can transform one state to the other and also distinguish between those using nontrivial loops as explained in the next section.

4.9 Expected measurement outcomes

Once we have prepared the ground state of the model, we can test the topological properties by measuring the state of individual qubits as well as correlations $\langle \Pi_{j\in \text{loop}} \sigma_j^x \rangle$ along a non-contractible loop of the lattice. For our minimal 8 qubit lattice, a non-trivial loop includes two spins. One could then transform one ground state $|\psi_\alpha\rangle$ to the other state $|\psi_\beta\rangle$ by applying a non-trivial loop of σ^y, $\Pi_{j\in \text{ loop}} \sigma_j^y$. While the state of the individual qubits should be the same for the two states (i.e. the reduced density matrices of the qubits are totally mixed), they can be distinguished by non-trivial correlation functions. In Tab. 4.2, the measurement outcomes of correlations along non-trivial loops are shown for ground state manifold of the eight-qubit toric code. One ground state is defined to be,

$$|\psi_1\rangle = \frac{1}{4\sqrt{2}}(\mathbf{1}+\sigma_1^y\sigma_4^y\sigma_5^y\sigma_3^y)(\mathbf{1}+\sigma_2^y\sigma_3^y\sigma_6^y\sigma_4^y)(\mathbf{1}+\sigma_5^y\sigma_8^y\sigma_1^y\sigma_7^y)(\mathbf{1}+\sigma_6^y\sigma_7^y\sigma_2^y\sigma_8^y)\prod_{j=1}^{8}|+_j\rangle\,, \tag{4.89}$$

where $|+_j\rangle$ is the eigenstate of σ_j^x with eigenvalue 1, $\sigma_j^x|+_j\rangle = |+_j\rangle$. The other three ground states can be found by applying the loop operators $\sigma_5^y\sigma_6^y$, $\sigma_4^y\sigma_8^y$ and $\sigma_4^y\sigma_8^y\sigma_5^y\sigma_6^y$,

$$|\psi_2\rangle = \sigma_5^y\sigma_6^y|\psi_1\rangle\,,\quad |\psi_3\rangle = \sigma_4^y\sigma_8^y|\psi_1\rangle\,,\quad |\psi_4\rangle = \sigma_4^y\sigma_8^y\sigma_5^y\sigma_6^y|\psi_1\rangle\,. \tag{4.90}$$

	$\langle\sigma_1^x\sigma_2^x\rangle$	$\langle\sigma_3^x\sigma_4^x\rangle$	$\langle\sigma_5^x\sigma_6^x\rangle$	$\langle\sigma_7^x\sigma_8^x\rangle$	$\langle\sigma_3^x\sigma_7^x\rangle$	$\langle\sigma_1^x\sigma_5^x\rangle$	$\langle\sigma_4^x\sigma_8^x\rangle$	$\langle\sigma_2^x\sigma_6^x\rangle$
$\lvert\psi_1\rangle$	0	1	0	1	0	1	0	1
$\lvert\psi_2\rangle$	0	1	0	1	0	-1	0	-1
$\lvert\psi_3\rangle$	0	-1	0	-1	0	1	0	1
$\lvert\psi_4\rangle$	0	-1	0	-1	0	-1	0	-1

Table 4.3: Two-qubit correlations along non-contractible loops for the 4 ground states of the toric code on an 8-qubit lattice.

4.10 Summary

In this chapter, we introduced the toric code, a central 2D model in the class of many-body models with topological order and proposed a multi-mode driven superconducting circuits to implement the Hamiltonian of model. We demonstrated that the two types of four-body interactions in the toric code, namely the star and plaquette interactions, can be realized via a same circuitry with different modulations. The coupling circuit is embedded within each cell of the lattice and composed of a dc-SQUID which is inductively coupled to four adjacent transmons. We argued that by modulating the SQUID with suitable engineered fluxes with eight frequency components, the toric code Hamiltonian is the leading order of the effective Hamiltonian of the driven circuit. We provided an example of the parameters for a realistic implementation on a minimal lattice with eight qubits and examined the adiabatic preparation of the topologically-ordered state via an adiabatic approach as well as the measurement and detection of the prepared state.

In this chapter, the effective Hamiltonian was derived directly in the time-domain using of the Schrieffer-Wolff transformation. In the following chapter, we turn to an alternative approach and propose a time-independent setting to engineer the effective Hamiltonian of coupled transmons. Making use of the Floquet formalism, we will show that a complete set of spin-spin interactions can effectively be constructed in transmon circuits with linear and nonlinear couplings.

Chapter 5

Floquet engineering of arbitrary spin-spin interactions

As we discussed in chapter 3 controllability is one of the criteria for a quantum simulator. For an analog quantum simulator, controllability means that the simulator is supplied with tunable couplings which enables it to realize a wide range of models and explore different regimes of a certain model. In the language of digital quantum simulators, this translates into an implementation of a complete set of quantum gates. In superconducting circuits tunability can be achieved through a number of techniques. In chapter 2, we introduced some architectures for tunable couplings. In transmon-based superconducting circuits with fixed couplings, the external flux through the qubit SQUID can be used as a simple knob to tune qubits into and out of resonance with each other. Also in circuit QED, it is possible to design a tunable resonator [128, 129], e.g. by placing a dc-SQUID in the middle of the coplanar waveguide (CPW), and then tune the resonator in resonance with different qubits to implement an effective interaction between them. These approaches come with their own shortcomings. For example a flux tunable transmon is susceptible to flux noise or a tunable resonator could face frequency crowding i.e. crossing unwanted resonances. Note that these schemes result in a simple exchange (hopping) interaction, therefore yet an implementation of a complete set of gates requires a digital approach i.e. combining this interaction with one-body rotations, etc.

Another possibility to implement qubit-qubit interactions in superconducting circuits, which is the subject of this chapter, is to use microwave driving. In a general context, driven time-dependent quantum systems can exhibit properties which are absent in their static counterparts. In recent years there has been a surge of research on the possibility of manipulating and shaping the behaviour of static systems through designing appropriate external modulations [130–133]. As the Floquet theory lays the foundations of studying such systems, these approaches are known as *Floquet engineering* in the literature. In superconducting circuits, the scope of employing engineered microwave driving to implement interactions has been explored in a number of works [134–141] Here the idea is to open spectral gaps in an engineered manner and close them by means of external modulations. In this chapter, we propose a unified toolbox based on this idea to generate arbitrary qubit-qubit interactions with superconducting qubits. In our case, we consider two transmon qubits with linear and nonlinear couplings which are driven by single-mode and bimodal drives. The advantage of such a toolbox is that it can be systematically generalized to other two-qubit circuits or to architectures with multiple qubits. Also the effective interactions can be derived beyond a Rotating Wave Approximation (RWA) to higher orders of a perturbation theory. The structure of this chapter is as follows: In Sec. 5.1, we give a rather mathematical introduction to the Floquet theory applied to driven quantum systems. In Sec. 5.2, we will show how to derive an effective description of the system based on Floquet theory. We then apply this method to two types of coupled-qubit superconducting circuits. In Sec. 5.3, we consider two-driven qubits with a linear capacitive coupling between them. In Sec. 5.4, we consider two-qubits with a driven SQUID coupler. We will show that one can implement various qubit-qubit couplings in such circuits by suitable driving functions.

5.1 Basic elements of Floquet theory

Floquet theory provides a versatile framework to study quantum systems which are symmetric under discrete translations in time [142]. In this section, we first discuss the implications of the Floquet theory for Hamiltonians that are periodic in time, and later we will show that the results for a periodic Hamiltonian can be generalized to systems with quasi-periodic driving, i.e. systems including multiple periodic drives. We will show that in both periodic and quasi-periodic cases, there is an infinite-dimensional time-independent representation of the time-dependent Hamiltonian. In Sec. 5.2, we use this result to derive an effective time-independent Hamiltonian which describes the driven system on slow time-scales. The advantage of Floquet formalism is that it avoids secular terms in all levels of approximation in contrast with other time-dependent perturbations theories.

We assume that $H(t)$ is a T-periodic Hamiltonian defined on a Hilbert space $\mathscr{H}$ such that,

$$H(t+T) = H(t). \tag{5.1}$$

Floquet theory [143] states that for this Hamiltonian, the solutions of the time-dependent Schrödinger equation,

$$i\partial_t \left|\psi(t)\right\rangle = H(t) \left|\psi(t)\right\rangle \tag{5.2}$$

is given by *Floquet states* which acquire the following generic form,

$$\left|\psi_\alpha(t)\right\rangle = \exp(-i\epsilon_\alpha t) \left|u_\alpha(t)\right\rangle, \tag{5.3}$$

where $\left|u_\alpha(t)\right\rangle$ is T-periodic state called *Floquet mode*, i.e. $\left|u_\alpha(t+T)\right\rangle = \left|u_\alpha(t)\right\rangle$ and ϵ_α is the Floquet characteristic exponent or the *quasienergy*. Quasienergies characterize the Floquet states of a time-periodic system in the same way that quasimomenta characterize Bloch states in a quantum system with a spatially periodic potential. Indeed, by recasting the Schrödinger equation in terms of the Floquet modes, the quasienergies become the eigenvalues of the new Hamiltonian operator,

$$\tilde{H}(t) \left|u_\alpha(t)\right\rangle \equiv \big(H(t) - i\partial_t\big) \left|u_\alpha(t)\right\rangle = \epsilon_\alpha \left|u_\alpha(t)\right\rangle. \tag{5.4}$$

We denote the frequency of the Hamiltonian by ω_d,

$$\omega_d = \frac{2\pi}{T}. \tag{5.5}$$

It is easy to verify that the Floquet mode,

$$\left|u_{\alpha,n}(t)\right\rangle \equiv \left|u_\alpha(t)\right\rangle e^{in\omega_d t}, \quad n \in \mathbf{Z}, \tag{5.6}$$

yields an identical solution to that in Eq. (5.2), but with a shifted quasienergy $\epsilon_{\alpha,n} = \epsilon_\alpha + n\omega_d$,

$$\left|\psi_\alpha(t)\right\rangle = \exp\left(-i\epsilon_{\alpha,n}t\right)\left|u_{\alpha,n}\right\rangle = \exp\left(-i\epsilon_\alpha t\right)\left|u_\alpha\right\rangle. \tag{5.7}$$

The index α characterizes a whole class of solutions $\left|u_{\alpha,n}\right\rangle$ with quasienergies $\epsilon_{\alpha,n}$. Note that $\epsilon_\alpha = \epsilon_{\alpha,n}$. Analogous to quasimomenta in Bloch theory, one can restrict the definition of quasienergies to a first *Brillouin zone* such that $-\hbar\omega_d/2 \leq \epsilon_\alpha < \hbar\omega_d/2$.

5.1.1 Time-independent representation

In a seminal work J. Shirley showed that by expressing a time-periodic Hamiltonian in terms of its Fourier components, one can derive an equivalent exact time-independent representation of the system in an infinite-dimensional composite (extended) space $\mathscr{H}_c = \mathscr{H} \otimes \mathscr{T}$ [144, 145]. Here $\mathscr{T}$ is the space of square integrable T-periodic functions, which is spanned by an orthonormal set of Fourier states $|n\rangle$ with $n = 0, \pm1, \pm2, ...$, the temporal representation of which reads, $\langle t|n\rangle = \exp\left(in\omega_d t\right), n = 0, \pm1, \pm2, ...$ In this representation time is treated as a coordinate with periodic boundary conditions. A complete orthonormal basis for the composite Hilbert space $\mathscr{H}_c$ is denoted by $|\alpha, n\rangle\rangle = |\alpha\rangle \otimes |n\rangle$, where $|\alpha\rangle$ represents a basis for $\mathscr{H}$. Projected back to the time-domain, this composite state reads,

$$\langle t|\alpha, n\rangle\rangle = |\alpha\rangle\, e^{-in\omega_d t}. \tag{5.8}$$

A Floquet mode $|u_{\alpha,n}(t)\rangle$ is denoted by $|u_{\alpha,n}\rangle\rangle$ in the composite space, where,

$$\langle t|u_{\alpha,n}\rangle\rangle = |u_\alpha(t)\rangle\, e^{-in\omega_d t}. \tag{5.9}$$

For two T-periodic functions $u_\alpha(t)$ and $u_\beta(t)$, the inner product in $\mathscr{H}_c$ reads,

$$\langle\langle u_\alpha|u_\beta\rangle\rangle = \frac{1}{T}\int_0^T dt\, \langle u_\alpha(t)|u_\beta(t)\rangle\,. \tag{5.10}$$

The next step is to find the representation of the Hamiltonian $H(t)$ in the extended space. We denote this representation by $\mathcal{H}_F$.Since $H(t)$ is T-periodic, we can decompose it to the Fourier components,

$$H(t) = \sum_{n=-\infty}^{\infty} e^{in\omega_d t} H^{(n)}, \tag{5.11}$$

where,

$$H^{(n)} = \frac{1}{T}\int_0^T dt e^{-in\omega_d t} H(t). \tag{5.12}$$

Note that $H^{(0)}$ is the static part of the Hamiltonian. The matrix elements of $\mathcal{H}_F$ can be derived as follows,

$$\begin{aligned} \langle\langle \alpha, n|\mathcal{H}_F|\beta, m\rangle\rangle &= \frac{1}{T}\int_0^T dt e^{-in\omega_d t}\, \langle\alpha|H(t) - i\frac{d}{dt}|\beta\rangle\, e^{im\omega_d t} \\ &= \langle\alpha|H^{(n-m)}|\beta\rangle + \delta_{nm}\delta_{\alpha\beta} m\omega_d. \end{aligned} \tag{5.13}$$

In a matrix form, the Floquet Hamiltonian $\mathcal{H}_F$ has the following structure,

$$\begin{array}{c|c|c|c|c|c|c|c}
 & \downarrow m & -2 & -1 & 0 & +1 & +2 & \\
\hline
\rightarrow n & \ddots & \vdots & \vdots & \vdots & \vdots & \iddots & \\
\hline
-2 & \dots & H^{(0)} - 2\omega_d\mathbf{1} & H^{(-1)} & H^{(-2)} & H^{(-3)} & H^{(-4)} & \dots \\
\hline
-1 & \dots & H^{(1)} & H^{(0)} - \omega_d\mathbf{1} & H^{(-1)} & H^{(-2)} & H^{(-3)} & \dots \\
\hline
0 & \dots & H^{(2)} & H^{(1)} & H^{(0)} & H^{(-1)} & H^{(-2)} & \dots \\
\hline
+1 & \dots & H^{(3)} & H^{(2)} & H^{(1)} & H^{(0)} + \omega_d\mathbf{1} & H^{(-1)} & \dots \\
\hline
+2 & \dots & H^{(4)} & H^{(3)} & H^{(2)} & H^{(1)} & H^{(0)} + 2\omega_d\mathbf{1} & \dots \\
\hline
 & \iddots & \vdots & \vdots & \vdots & \vdots & \vdots & \ddots
\end{array} \tag{5.14}$$

This matrix is divided into sectors which can be labelled by Fourier (photon) indices n and m, where each sector is of the dimension of the Hilbert space $\mathscr{H}$. The diagonal is composed of copies of the static Hamiltonian $H^{(0)}$ shifted by the energy of the photons that label each diagonal sector, i.e. $n\omega_d\mathbf{1}$.The construction of Floquet matrix is facilitated by introducing operators F_n and N in the Fourier space $\mathscr{T}$,

$$\begin{aligned} \langle m'|F_n|m\rangle &= \delta_{m'-m,n}, \\ \langle m'|N|m\rangle &= m\delta_{m',m}. \end{aligned} \tag{5.15}$$

In terms of these operators the Floquet Hamiltonian reads,

$$\mathcal{H}_F = \sum_n H^{(n)} \otimes F_n + \omega_d\mathbf{1} \otimes N. \tag{5.16}$$

In the extended space $\mathscr{H}_c$, the Schrödinger Eq. (5.4) leads to the following eigenvalue equation,

$$\mathcal{H}_F\, |u_{\alpha,n}\rangle\rangle = \epsilon_{\alpha,n}\, |u_{\alpha,n}\rangle\rangle\,. \tag{5.17}$$

The eigenstates $|u_{\alpha,n}\rangle\rangle$ of $\mathcal{H}_F$ are Floquet modes $|u_{\alpha,n}(t)\rangle$ represented in the extended space, and their corresponding quasienergies are $\epsilon_{\alpha,n}$. In particular, we note that this eigenvalue equation incorporates the redundancy of the solutions i.e. *all* solutions of the problem appear as eigenstates and not just the representative solution $|u_\alpha(t)\rangle$. Equivalently one can write,

$$\mathcal{H}_F = \sum_{\alpha,n} \epsilon_{\alpha,n} \left|u_{\alpha,n}\rangle\rangle \langle\langle u_{\alpha,n}\right| , \tag{5.18}$$

We can define a time-evolution operator for the Floquet Hamiltonian in the composite space,

$$\mathcal{U}_F(t,t_0) = e^{-i\mathcal{H}_F(t-t_0)}. \tag{5.19}$$

The matrix elements of this operator are connected to the matrix elements of the time-evolution operator $U(t,t_0)$ as follows,

$$\langle\langle\beta, m|\mathcal{U}_F|\alpha, n\rangle\rangle = \frac{1}{T}\int_0^T dt e^{i(n-m)\omega_d t} \langle\alpha|U(t,t_0)|\beta\rangle . \tag{5.20}$$

Note that this matrix elements are invariant under a constant shift in the photon indices,

$$\langle\langle\beta, m|\mathcal{U}_F|\alpha, n\rangle\rangle = \langle\langle\beta, m+k|\mathcal{U}_F|\alpha, n+k\rangle\rangle . \tag{5.21}$$

Conversely, $U(t,t_0)$ can be written in terms of matrix elements of $\mathcal{U}_F$,

$$\langle\beta|U(t,t_0)|\alpha\rangle = \sum_n \langle\langle\beta, n|\mathcal{U}_F(t-t_0)|\alpha, 0\rangle\rangle e^{in\omega t}. \tag{5.22}$$

Using the time-evolution operator, we can calculate the transition probability from an initial state $|\alpha\rangle$ at time t_0 to a final state $|\beta\rangle$ at t,

$$\begin{aligned} P_{\alpha\to\beta}(t,t_0) &= |\langle\beta|U(t,t_0)|\alpha\rangle|^2 \\ &= \sum_{n,m} e^{im\omega t_0} \langle\langle\alpha, m|\exp(-i\mathcal{H}_F(t-t_0))|\beta, n\rangle\rangle \times \\ &\qquad\qquad \langle\langle\beta, n|\exp(-i\mathcal{H}_F(t-t_0))|\alpha, 0\rangle\rangle . \end{aligned} \tag{5.23}$$

Averaged over the initial time t_0 while keeping the elapsed time $\Delta t = t - t_0$ constant, the transition probability as a function of Δt reads,[1]

$$\overline{P}_{\alpha\to\beta}(t-t_0) = \sum_n |\, \langle\langle \beta, n|\exp(-i\mathcal{H}_F(t-t_0))|\alpha, 0\rangle\rangle\, |^2. \tag{5.24}$$

The time-averaged transition probability $\overline{\overline{P}}$ is given by averaging $\overline{P}(\Delta t)$ over Δt,

$$\overline{\overline{P}}_{\alpha\to\beta} = \sum_n \sum_{\gamma m} |\, \langle\langle \beta, n|u_{\gamma,m}\rangle\rangle\, \langle\langle u_{\gamma,m}|\alpha, 0\rangle\rangle\, |^2. \tag{5.25}$$

5.1.2 Generalization to many-mode Floquet theory

Thanks to the Shirley's time-independent formalism of a Floquet system, the results of the single-mode Floquet theory can be easily generalized to a multi-mode driven system, i.e. a system which is modulated by several time-periodic functions with incommensurate periodicities [146–148]. Here, we present the results for a bimodally driven system which we consider in the subsequent sections. Nevertheless a generalization to higher number of modes is straight forward and should be clear from our discussion.

Let us assume $H(t)$ is the Hamiltonian of a quantum system which can be split into two time-periodic parts with periodicities T_1 and T_2. For this quasiperiodic Hamiltonian, there is a time-independent representation $\mathcal{H}_F$ in the composite Hilbert space $\mathscr{H}_c = \mathscr{H} \otimes \mathscr{T}_1 \otimes \mathscr{T}_2$, where $\mathscr{T}_j$, $j = 1, 2$ is the space of the functions with periodicity $T_j = \frac{2\pi}{\omega_{dj}}$. Fourier states $\{|n_j\rangle\, | n_j \in \mathbb{Z}\}$ constitute a basis for $\mathscr{T}_j$ such that $\langle t|n_j\rangle = \exp(-in_j\omega_{dj}t)$.

To derive this result, we decompose $H(t)$ in terms of its Fourier components $H^{(n_1,n_2)}$, see Eq. (5.11),

$$H(t) = \sum_{n_1,n_2=-\infty}^{+\infty} H^{(n_1,n_2)} \exp\left[i(n_1\omega_{d1} + n_2\omega_{d2})t\right]. \tag{5.26}$$

---

[1] It refers to a random switching time and measurement after a constant elapsed time.

The matrix elements of $\mathcal{H}_F$ are now given as follows,

$$\begin{aligned}&\langle\langle\alpha, n_1, n_2|\mathcal{H}_F|\beta, m_1, m_2\rangle\rangle \\ &= \langle\alpha|H^{(n_1-m_1,n_2-m_2)}|\beta\rangle + \delta_{n_1m_1}\delta_{n_2m_2}\delta_{\alpha\beta}(n_1\omega_{d1} + n_2\omega_{d2}).\end{aligned} \tag{5.27}$$

This Floquet matrix explicitly reads,

$$\begin{array}{c|c|c|c|c|c}
 & \downarrow m_2 & -1 & 0 & +1 & \\
\hline
\rightarrow n_2 & \ddots & \vdots & \vdots & \vdots & \iddots \\
\hline
-1 & \dots & H^{(\Delta_1,0)} - \omega_{d2}\mathbf{1} & H^{(\Delta_1,-1)} & H^{(\Delta_1,-2)} & \dots \\
\hline
0 & \dots & H^{(\Delta_1,1)} & H^{(\Delta_1,0)} & H^{(\Delta_1,-1)} & \dots \\
\hline
+1 & \dots & H^{(\Delta_1,2)} & H^{(\Delta_1,1)} & H^{(\Delta_1,0)} + \omega_{d2}\mathbf{1} & \dots \\
\hline
 & \iddots & \vdots & \vdots & \vdots & \ddots
\end{array} \tag{5.28}$$

where $\Delta_1 = n_1 - m_1$ and $\mathbf{1}$ is the identity operator in the composite space $\mathscr{H} \otimes \mathscr{T}_1$. Each of the blocks in the bimodal Floquet matrix (5.28) is a matrix of the following form,

$$\begin{array}{c|c|c|c|c|c}
 & \downarrow m_1 & -1 & 0 & +1 & \\
\hline
\rightarrow n_1 & \ddots & \vdots & \vdots & \vdots & \iddots \\
\hline
-1 & \dots & H^{(0,\overline{\Delta}_2)} - \omega_{d1}\mathbf{1} & H^{(-1,\overline{\Delta}_2)} & H^{(-2,\overline{\Delta}_2)} & \dots \\
\hline
0 & \dots & H^{(1,\overline{\Delta}_2)} & H^{(0,\overline{\Delta}_2)} & H^{(-1,\overline{\Delta}_2)} & \dots \\
\hline
+1 & \dots & H^{(2,\overline{\Delta}_2)} & H^{(1,\overline{\Delta}_2)} & H^{(0,\overline{\Delta}_2)} + \omega_{d1}\mathbf{1} & \dots \\
\hline
 & \iddots & \vdots & \vdots & \vdots & \ddots
\end{array} \tag{5.29}$$

Note that this matrix has exactly the same structure as Eq. (5.14) and $\mathbf{1}$ is the identity in $\mathscr{H}$. The representation of the bimodal Floquet matrix, Eq. (5.28), is indeed perceived as a nested matrix and each diagonal sector of this matrix can be labelled by the photon indices n_1 and n_2, where n_j is the number of photons exchanged between the static system and the j^{th} drive. In this representation, the photon numbers shift the energies of the diagonal sectors and hence the explicit form of a diagonal sector which lives in the Hilbert space

$\mathscr{H}$ reads,

$$H^{(0,0)} + n_1\omega_{d1}\mathbf{1} + n_2\omega_{d2}\mathbf{1}. \tag{5.30}$$

The Floquet matrix can also be written in a compact form using of the operators F_n and N, c.f. Eq. (5.15),

$$\mathcal{H}_F = \sum_{(n_1,n_2)} H^{(n_1,n_2)} \otimes F_{n_1} \otimes F_{n_2} + \omega_{d1}\mathbf{1} \otimes \mathbf{1} \otimes N + \omega_{d2}\mathbf{1} \otimes N \otimes \mathbf{1}. \tag{5.31}$$

The eigenstates of $\mathcal{H}_F$ are the bimodal Floquet modes $|u_{\alpha,n_1,n_2}\rangle\rangle$ and the corresponding quasienergies are denoted by $\epsilon_{\alpha,n_1,n_2}$,

$$\mathcal{H}_F\,|u_{\alpha,n_1,n_2}\rangle\rangle = \epsilon_{\alpha,n_1,n_2}\,|u_{\alpha,n_1,n_2}\rangle\rangle\,. \tag{5.32}$$

The quasienergies satisfy the following periodic structure,

$$\epsilon_{\alpha,n_1,n_2} = \epsilon_{\alpha,0,0} + n_1\omega_{d1} + n_2\omega_{d2}, \tag{5.33}$$

where $\epsilon_{\alpha,0,0}$ lies in the first Brillouin zone $-\omega_{dj}/2 \leq \epsilon_{\alpha,0,0} \leq \omega_{dj}/2$ for $j = 1, 2$. For simplicity it is denoted by ϵ_α. The time-evolution $\mathcal{U}_F$ for the bimodal system in the extended space is defined in a same form as for a single-mode system, c.f. Eq. (5.19). From $\mathcal{U}_F$, one can calculate the probability of a transition from $|\alpha(t_0)\rangle$ to $|\beta(t)\rangle$,

$$\begin{aligned} P_{\alpha\to\beta}(t,t_0) &= |\,\langle\beta|U(t,t_0)|\alpha\rangle\,|^2 \\ &= \sum_{n_1,n_2}\sum_{m_1,m_2} e^{i(m_1\omega_{d1}+m_2\omega_{d2})t_0}\,\langle\langle\alpha,m_1,m_2|e^{-i\mathcal{H}_F(t-t_0)}|\beta,n_1,n_2\rangle\rangle\,\times \\ &\qquad\qquad \langle\langle\beta,n_1,n_2|e^{-i\mathcal{H}_F(t-t_0)}|\alpha,0,0\rangle\rangle\,. \end{aligned} \tag{5.34}$$

Once averaged over the initial time t_0, the transition probability as a function of the elapsed time $t - t_0$ reads,

$$\begin{aligned} \overline{P}_{\alpha\to\beta}(t-t_0) &= |\,\langle\beta|U(t,t_0)|\alpha\rangle\,|^2 \\ &= \sum_{n_1,n_2} |\,\langle\langle\beta,n_1,n_2|\exp(-i\mathcal{H}_F(t-t_0))|\alpha,0,0\rangle\rangle\,|^2. \end{aligned} \tag{5.35}$$

If we further average over the elapsed time as well, we arrive at the time-averaged transition probability $\overline{\overline{P}}$,

$$\overline{\overline{P}}_{\alpha\to\beta} = \sum_{n_1 n_2} \sum_{\gamma m_1 m_2} | \langle\langle \beta, n_1, n_2 | u_{\gamma,m_1,m_2} \rangle\rangle \langle\langle u_{\gamma,m_1,m_2} | \alpha, 0, 0 \rangle\rangle |^2. \tag{5.36}$$

5.2 Effective description of Floquet Hamiltonian

Having introduced the mathematical description of single-mode and bimodal driven systems based on Floquet theory, in this section we present our approach to obtain an effective low-energy description of the system. This will also provide us with a transparent view towards engineering the low-energy subspace and implementing a target Hamiltonian. In a regime where the modulation frequency is the largest energy scale of the system, or alternatively such a statement holds in a rotating frame, we expect that two time-scales govern the dynamics of the system: on short-time scales the behaviour of the system is determined by the high-energy manifold due to high-frequency driving, while the the slow and long-term dynamics is dominated by the low-energy manifold. In the literature, the short-term behaviour, which concerns the details of dynamics within a cycle of driving, is referred to as *micromotion*. The long-term low-energy dynamics on the other hand can be *approximately* described in terms of an effective Hamiltonian H_{eff} in $\mathscr{H}$. In the previous section, we argued that a periodic or quasiperiodic Hamiltonian $H(t)$ can be represented *exactly* by the time-independent Hamiltonian $\mathcal{H}_F$ in the extended space $\mathscr{H}_c$ where time is treated as a coordinate. Whereas we outlined how to construct the equivalent Hamiltonian $\mathcal{H}_F$ in the extended space in Sec. 5.1.1, we are yet to determine how the effective Hamiltonian H_{eff} can be deduced from $\mathcal{H}_F$. The aim of this section is to build up the connection between these two descriptions. As pointed out in the previous section, the static part of the time-dependent system is encoded in a redundant way on the diagonal of the Floquet Hamiltonian. For the single-mode system, each diagonal block is labelled by a drive photon number n since it contains the static Hamiltonian $H^{(0)}$

shifted by the energies of n photons, c.f. Eq. (5.14). The time-periodic part of the Hamiltonian, on the other hand, appears in the off-diagonal blocks of the Floquet Hamiltonian and couples the diagonal blocks. The diagonal blocks n and m are coupled via Fourier components $H^{(n-m)}$ and $H^{(m-n)}$. Physically, this coupling describes a process in which there is a transition between the states of the system enabled by exchanging $|n-m|$ photons with the drive.

For the bimodal system, a diagonal block which contains n_1 photon from the first drive and n_2 photons from the second drive is labelled by these indices and the energies of these photons are added to the static Hamiltonian, i.e. the explicit form of such a block reads, $H^{(0,0)} + n_1\omega_{d1}\mathbf{1} + n_2\omega_{d2}\mathbf{1}$. A diagonal block which labelled by n_1 and n_2 is coupled to a second diagonal block labelled by m_1 and m_2 through the following Fourier components which appear as off-diagonal blocks of the Floquet matrix,

$$H^{(n_1-m_1,n_2-m_2)}, \quad H^{(m_1-n_1,m_2-n_2)}, \quad H^{(n_1-m_1,m_2-n_2)}, \quad H^{(m_1-n_1,n_2-m_2)}. \tag{5.37}$$

These processes involve $|n_1 - m_1|$ photons from the first drive and $|n_2 - m_2|$ photons from the second drive.

Depending on the frequency of the modulation, one can distinguish two operational regimes in a Floquet system. In these regimes, the structure of the Floquet matrix takes on different forms in terms of the spacing between the quasienergy levels. In *the high frequency regime*, the modulation frequency (frequencies) is (are) much larger than the internal energy spacings of the static system [130, 132], while in *the resonant regime*, the applied frequencies coincide with the internal energies of the static system. In this chapter, we are interested in the resonant Floquet engineering. Hence in the following, we first briefly discuss the case with high-frequency modulation and then turn to a detailed discussion of resonant modulation.

5.2.1 High-frequency regime

In this regime, for a single-mode driven system we have $\omega_d \gg ||H^{(n)}||$ with $n \in \mathbb{Z}$, where ω_d is the modulation frequency. The modulation therefore generates a wide spectral gap between the blocks of the Floquet Hamiltonian $\mathcal{H}_F$

and the block with $n = 0$, i.e. with no drive photons, is the low energy subspace of the Floquet Hamiltonian, c.f. Eq. (5.14). This low-energy subspace is coupled to higher energy subspaces via off-diagonal blocks. The effective Hamiltonian is then given by block-diagonalizing the Floquet matrix with respect to photon index n such that off-diagonal blocks (i.e. couplings) are removed. Since we assume that the coupling between the blocks is weak compared to the modulation amplitude, the off-diagonal blocks can be treated as a perturbation. The block-diagonalization can be performed using Van Vleck perturbation theory [149, 151, 154] and the result has the form,

$$\begin{array}{c|c|c|c|c|c|c|c}
 & \downarrow m & +2 & +1 & 0 & -1 & -2 & \\
\hline
\rightarrow n & \ddots & \vdots & \vdots & \vdots & \vdots & \iddots & \\
\hline
+2 & \dots & H_{eff}+2\omega_d\mathbf{1} & 0 & 0 & 0 & 0 & \dots \\
\hline
+1 & \dots & 0 & H_{eff}+\omega_d\mathbf{1} & 0 & 0 & 0 & \dots \\
\hline
0 & \dots & 0 & 0 & H_{eff} & 0 & 0 & \dots \\
\hline
-1 & \dots & 0 & 0 & 0 & H_{eff}-\omega_d\mathbf{1} & 0 & \dots \\
\hline
-2 & \dots & 0 & 0 & 0 & 0 & H_{eff}-2\omega_d\mathbf{1} & \dots \\
\hline
 & \iddots & \vdots & \vdots & \vdots & \vdots & \vdots & \ddots
\end{array} \tag{5.38}$$

The block-diagonalized Hamiltonian has copies of the effective Hamiltonian H_{eff} on its diagonal and this Hamiltonian is simply given by projecting the result onto $n = 0$ sector.

The discussion for a many-mode Floquet system is similar to the single-mode case [120], except that the block-diagonalized Hamiltonian should eventually be projected to the subspace with zero photons from both drives, i.e. $n_1 = 0$ and $n_2 = 0$.

5.2.2 Resonant regime

In case of resonant modulation, the Floquet states of two blocks are coupled via the external driving, which leads to a degeneracy of the coupled states. These degenerate states define a manifold $\mathcal{S}$ which determines the low-energy dynamics of the system, and hence the effective Hamiltonian is given in terms of this manifold. In particular, note that the dynamics is no longer given by the zero photon sector of the Floquet Hamiltonian. Since non-zero sectors of the Floquet Hamiltonian also contribute to the dynamics of the Floquet Hamiltonian, the effective Hamiltonian is realized in a *suitable* rotating frame of the Hilbert space $\mathscr{H}$. Therefore the "slow" dynamics should be interpreted with respect to this rotating frame.

In this chapter, our aim is to use Floquet engineering to implement certain two-body couplings. Hence the set of states that constitutes the degenerate manifold depends on the type of interaction we seek to engineer. Indeed to implement a certain interaction term, we perform an inverse engineering and first identify the states that build $\mathcal{S}$. Then we design an external driving such that desired states form the degenerate manifold. Note that due to a zero detuning between Flouqet states in $\mathcal{S}$, perturbation theory cannot be applied as in high-frequency Floquet engineering as it would result in divergencies. In some cases, it is possible to *a priori* find a rotating frame in which the problem transforms into the high-frequency regime with large detunings and comparably smaller couplings and thus one can apply the results of that regime [153]. However, finding such a rotating frame could be non-trivial or transforming to such a rotating frame could result in an even more involved problem e.g. when a resonance occurs at higher orders of the perturbation theory. Generally speaking, one should then apply a degenerate perturbation theory to this case. Note that in our approach, we consider two subspaces, namely fast and slow ones, and we could apply the Van Vleck perturbation theory [149, 154]. However, we take a different path towards derivation the effective Hamiltonian and apply the (nearly) degenerate perturbation theory of Salwen [150, 152]. With this approach, one can go to arbitrary higher orders in perturbation theory numerically or analytically.

We now show how to derive an effective Hamiltonian in this regime for single-mode and bimodal driven systems.

Resonant Floquet engineering in single-mode systems

Here and in the following sections, we choose the basis of the Hilbert space $\mathscr{H}$, i.e. $|\alpha\rangle$, to be eigenstates of the static Hamiltonian in the absence of any couplings. The corresponding eigenenergies are denoted by $E_\alpha^{(0)}$. Subsequently, the Floquet Hamiltonian $\mathcal{H}_F$ is decomposed into a free part $\mathcal{H}_{F0}$ and an interaction part $\mathcal{V}$ such that,

$$\mathcal{H}_F = \mathcal{H}_{F0} + \mathcal{V}, \tag{5.39}$$

where we assume that $\mathcal{V}$ can be treated as a perturbation to $\mathcal{H}_{F0}$. For single-mode systems, the Floquet states $|\alpha, n\rangle\rangle$ are the eigenstates of $\mathcal{H}_{F0}$ with eigenenergies

$$\epsilon_{\alpha,n}^{(0)} = E_\alpha^{(0)} + n\omega_d. \tag{5.40}$$

The eigenstates of $\mathcal{H}_F$ corresponding to the bare states $|\alpha, n\rangle\rangle$ are denoted by $|u_{\alpha,n}\rangle\rangle$ and their quasienergies by $\epsilon_{\alpha,n}$, c.f. Eq. (5.17).

The degenerate manifold $\mathcal{S}$ is constructed from a set of eigenstates of $\mathcal{H}_{F0}$ that oscillate at zero frequency in a proper rotating frame. This manifold is separated by a gap from higher energy eigenstates of $\mathcal{H}_{F0}$. Therefore, by turning on the interaction part $\mathcal{V}$, which is weak compared to the energy gap, we expect that $\mathcal{S}$ mainly determines the dynamics of the interacting Floquet Hamiltonian and one can adiabatically eliminate high energy states to derive an effective description in term of states in $\mathcal{S}$. As a result the low-energy manifold is dressed by high-energy modes and the coupling between the slow and fast subspaces is removed. In contrast to the high-frequency regime, for which the effective Hamiltonian is obtained in the no-photon sector, here, different blocks contribute to the effective Hamiltonian. Therefore the low-energy dynamics in $\mathscr{H}_c$ corresponds to the dynamics seen from a suitable rotating frame in $\mathscr{H}$. In our case, this is the rotating frame in which the qubits rotate at their corresponding transition frequencies, i.e. the rotating frame of the qubits.

The adiabatic elimination of the high-energy states is performed via a generalized approach to Salwen's (nearly) degenerate perturbation theory [152] outlined in Appendix B. This perturbation theory leads to a matrix equation for the slow space, which should be solved in a self-consistent way for the quasienergies and eigenstates of the effective Hamiltonian, see Appendix B for details. For brevity, let us drop the index n from $|\alpha, n\rangle\rangle$ for the four states in the slow manifold that construct the effective Hamiltonian (i.e. a desired interaction) and denote them by $|\alpha\rangle\rangle \equiv |\alpha, n\rangle\rangle$, assuming that α tacitly distinguishes n. Hence $|\alpha\rangle$ is a state in $\mathcal{H}$ and $|\alpha\rangle\rangle$ is a state in the slow manifold of the composite space. Accordingly the quasienergy corresponding to $|\alpha\rangle\rangle$ is denoted by $\epsilon_\alpha^{(0)} \equiv \epsilon_{\alpha,n}^{(0)}$. For the Floquet matrix H_F, the generalized Salwen perturbation theory leads to the matrix equation,

$$\sum_{\beta=1}^{4} h_{\alpha\beta}(\epsilon) \langle\langle\beta|u\rangle\rangle = \epsilon \langle\langle\alpha|u\rangle\rangle \quad \text{with} \quad h_{\alpha\beta}(\epsilon) = \langle\langle\alpha|\mathcal{H}_{F0} + T(\epsilon)|\beta\rangle\rangle \tag{5.41}$$

for $\alpha = 1, 2, 3, 4$, the solution of which determines the quasienergies ϵ_α and Floquet states $|u_\alpha\rangle\rangle$ of the slow manifold of the interacting system. Here,

$$\mathcal{T}(\epsilon) = \sum_{k=0}^{+\infty} [\mathcal{V}\mathcal{G}_Q]^k \mathcal{V} \tag{5.42}$$

is the scattering matrix, where $\mathcal{G}_Q = \sum'_{\alpha,n}(|\alpha, n\rangle\rangle \langle\langle\alpha, n|)/[\epsilon - \epsilon_{\alpha,n}^{(0)}]$ is the Greens function associated with the fast space of H_{F0} and the notation $\sum'$ indicates that the degenerate space is excluded from this sum. Since $\mathcal{T}$ is a function of ϵ, the set of equations (5.41) needs to be solved in a self-consistent way.

In the absence of interactions, we get $\mathcal{T}(\epsilon) \equiv 0$ and the Floquet quasienergies $\epsilon_\alpha = \epsilon_\alpha^{(0)}$ for $\alpha = 1, 2, 3, 4$ are recovered from Eq. (5.41). For nonzero interactions, we make the ansatz that the quasienergies ϵ_α, and thus $\mathcal{T}(\epsilon)$ and $h_{\alpha\beta}$, associated to the slow space can be written as a perturbative expansion in interaction strength b ($\mathcal{V} \propto b$),

$$\epsilon_\alpha = \epsilon_\alpha^{(0)} + \delta\epsilon_\alpha, \quad \text{with} \quad \delta\epsilon_\alpha = \sum_{p=1}^{\infty} \kappa_{\alpha,p} b^p, \tag{5.43}$$

$$h_{\alpha\beta} = h_{\alpha\beta}(\epsilon_\alpha^{(0)}) + \sum_{p=1}^{\infty} h_{\alpha\beta,p} b^p, \tag{5.44}$$

where $\kappa_{\alpha,p}$ and $h_{\alpha\beta,p}$ are the perturbation coefficients. In practice we truncate the expansion at a desired cut-off order $p = p_c$ and calculate the eigenvalues of the effective Hamiltonian using equation (5.44). Note that the p-th order of ϵ_α modifies the matrix elements $h_{\alpha\beta}$ in $(p+2)$-th order because of the form of $\mathcal{T}(\epsilon)$ in Eq. (5.42), which subsequently changes the quasienergies of the updated matrix in $(p+2)$-th order. Hence the results (quasienergies) are exact up to p-th order. This suggests that the $\kappa_{\alpha,p}$ are determined by the following procedure: 1) truncate ϵ_α to p_c-th order, 2) calculate the matrix elements and quasienergies of the matrix and 3) compare the expansion (5.43) and calculated quasienergies.

Resonant Floquet engineering in bimodal driven systems

For bimodal driven systems, we again decompose the Floquet Hamiltonian $\mathcal{H}_F$ into non-interacting and interaction parts as in Eq. (5.39), where the parts are now defined in the composite space $\mathscr{H}_c = \mathscr{H} \otimes \mathscr{T}_1 \otimes \mathscr{T}_2$. The bare Floquet states $|\alpha, n_1, n_2\rangle\rangle$ are the eigenstates of the free Hamiltonian $\mathcal{H}_{F0}$ with quasienergies $\epsilon^{(0)}_{\alpha,n_1,n_2} = E^{(0)}_\alpha + n_1\omega_{d1} + n_2\omega_{d2}$. The eigenstates and quasienergies of the interacting Hamiltonian $\mathcal{H}_F$ are denoted by $|u_{\alpha,n_1,n_2}\rangle\rangle$ and $\epsilon_{\alpha,n_1,n_2}$ respectively. The manifold $\mathcal{S}$ is formed from a set of eigenstates of the free Floquet Hamiltonian $\mathcal{H}_{F0}$ that are perceived to implement a desired interaction. This manifold is engineered through the external modulation such that the states in $\mathcal{S}$ are set at zero energy in a suitable rotating frame and thus give rise to the slow dynamics of the system in the presence of an interaction $\mathcal{V}$.

To find the effective interaction Hamiltonians, we proceed as in the single mode case and adiabatically eliminate all Floquet states except for the four in the low-energy manifold and effectively describe the infinite-dimensional Floquet matrix by a 4 × 4 matrix. Dropping again the Fourier index for the low-energy states and quasienergies and denoting them by $|\alpha\rangle\rangle$ and $\epsilon^{(0)}_\alpha$, the Green's function of the fast space reads,

$$\mathcal{G}_Q(\epsilon) = \sum_{\alpha,n_1,n_2}{}' \frac{|\alpha, n_1, n_2\rangle\rangle \langle\langle\alpha, n_1, n_2|}{\epsilon - \epsilon^{(0)}_{\alpha,n_1,n_2}}, \tag{5.45}$$

where ϵ is the quasienergy of the degenerate manifold in the interacting limit and the sum runs over the fast space where the degenerate states are excluded (indicated by the prime). The procedure of constructing the self-consistent matrix equation and solving for its quasienergies runs analogous to the single-mode case, c.f. Eqs. (5.41), (5.42), (5.43) and (5.44).

5.3 Driven qubit schemes

In this section, we apply the Floquet engineering approach presented in Sec 5.2.2 to a driven two-qubit system with linear coupling [134]. We will show how to realize different types of qubit-qubit interactions in this system via appropriate single-mode and bimodal qubit modulations. The system we consider in this section is composed of two superconducting transmon qubits with Josephson energies E_{Jj} and capacitances C_j, $j = 1, 2$, as shown in Fig. 5.1. The two qubits are coupled linearly via a coupling capacitance C_t such that $C_t \ll C_j$. The dynamical nodal phases of the qubits and their conjugate variables are denoted by ϕ_j and $\pi_j = \hbar n_j$, i.e. $[\phi_i, \pi_j] = i\hbar\delta_{ij}$. The Hamiltonian of the circuit reads,

$$H_s = \sum_{j=1,2} E_{Jj}\cos(\phi_j) + E_{cj}n_j^2 + E_{cc}n_1 n_2, \tag{5.46}$$

where the capacitive energies are defined as,

$$\begin{aligned} E_{cj} &= \hbar^2(2\phi_0^2 C_j)^{-1}(1 - C_t/C_j), \\ E_{cc} &= \hbar^2(\phi_0^2 C_1 C_2)^{-1} C_t. \end{aligned} \tag{5.47}$$

Due to the nonlinearity of the transmon qubits, we truncate the Hamiltonian (5.46) to the single-excitation (qubit) subspace. The second-quantized form of the Hamiltonian in this subspace reads,

$$\begin{aligned} H_s &= H_0 + H_c, \\ H_0 &= \sum_{j=1,2} \hbar\omega_j \sigma_j^+\sigma_j^-, \quad H_c = g_c\sigma_1^y\sigma_2^y, \end{aligned} \tag{5.48}$$

where,

$$\begin{aligned}\hbar\omega_j &= \sqrt{2E_{Jj}E_{cj}} - E_{cj},\\ g_c &= -\frac{E_{cc}}{2\sqrt{2}}\left(\frac{E_{J1}E_{J2}}{E_{c1}E_{c2}}\right)^{1/4}.\end{aligned} \tag{5.49}$$

In the following sections, we consider a number of single-mode and bimodal time-dependent perturbations applied to the qubit(s). Since the coupling is fixed and the qubits are modulated, we call these driving methods *driven qubit schemes*. The aim is to enable different types of qubit-qubit couplings of the form,

$$e^{i\theta}\sigma_1^a\sigma_2^b + \text{H.c.}, \quad a,b \in \{x,y,z,+,-\}. \tag{5.50}$$

The following assumptions are made for all perturbations we consider here,

1. The two qubits are detuned from each other with a detuning Δ such that $|\Delta| \gg |g_c|$. Therefore, in the absence of driving the two qubits do not interact with each other.

2. The frequency (frequencies) of a drive, denoted by $\omega_d(\omega_{dj})$ for single-mode (two-modes) schemes, is (are) detuned from the transition frequency of the qubit it is applied to, therefore none of the drives create a bare excitation at the corresponding driven qubit.

To apply the Floquet formalism, we use the following basis for the Hilbert space $\mathscr{H}$ of two-qubits,

$$|\alpha=1\rangle \equiv |1_1,1_2\rangle\,, \quad |\alpha=2\rangle \equiv |1_1,0_2\rangle\,, \quad |\alpha=3\rangle \equiv |0_1,1_2\rangle\,, \quad |\alpha=4\rangle \equiv |0_1,0_2\rangle\,, \tag{5.51}$$

where $|0_j\rangle$ ($|1_j\rangle$) refers to the ground state (first excited state) of transmon j, i.e. $\sigma_j^+\sigma_j^-|n_j\rangle = n_j|n_j\rangle$. The state $|\alpha=j\rangle$ is the eigenstates of H_0 with the eigenenergy E_j,

$$E_1 = \hbar(\omega_1+\omega_2), \quad E_2 = \hbar\omega_1, \quad E_3 = \hbar\omega_2, \quad E_4 = 0. \tag{5.52}$$

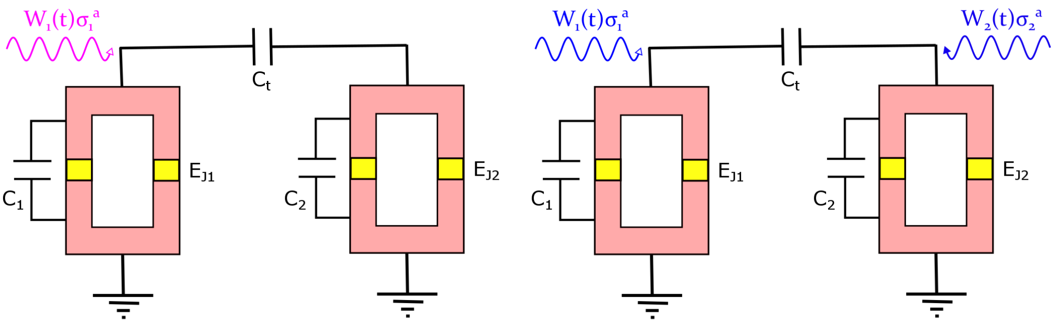

(a) (b)

Figure 5.1: Driven qubit schemes. Two transmon qubits are coupled linearly via a capacitance. The two qubits are non-interacting in the absence of driving, but using appropriate **(a)** single-mode or **(b)** bimodal drives with transverse ($a = x$) and longitudinal ($a = z$) modulations, it is possible to implement various two-qubit interactions.

5.3.1 Single-mode driven system

We first will show that by modulating a qubit of the circuit via a single-mode drive one can engineer parity-breaking ($\sigma_i^z\sigma_j^y$, $\sigma_i^z\sigma_j^x$), squeezing ($\sigma_i^+\sigma_j^+ + \text{H.c.}$) and hopping ($\sigma_i^+\sigma_j^- + \text{H.c.}$) interactions. By a single-mode drive, we mean that one of the qubits (here we assume qubit 1) is modulated by a periodic drive of the form,

$$H_d(t) = W_1(t)\sigma_1^a, \quad W_1(t) = b\cos(\omega_d t + \theta), \tag{5.53}$$

where ω_d and b are the modulation frequency and strength respectively. There are two types of single-mode modulations, namely *transverse modulation* for $a = x$ and *longitudinal modulation* for $a = z$. The total Hamiltonian of the circuit for a single mode driven scheme reads,

$$H(t) = H_s + H_d(t). \tag{5.54}$$

For $H(t)$, the following interactions can be implemented,

1. When the first qubit is driven with $a = x$ and $\omega_d = \omega_2$, the interaction $J_{zx}\sigma_1^z\sigma_2^x$ and $J_{zy}\sigma_1^z\sigma_2^y$ are implemented for $\theta = 0$ and $\theta = \pi$. This inter-

action is second order including single photon exchange with the drive i.e. $J_{zx} \sim J_{zy} \sim \frac{2\omega_2}{\omega_1^2-\omega_2^2} g_c b$. Alternatively by driving the second qubit one can realize $\sigma_1^x \sigma_2^z$ and $\sigma_1^y \sigma_2^z$. This scheme is also called the cross-resonant (CR) scheme [136, 137].

2. For $a = z$, $\theta = 0$, the hopping term $J_h \sigma_1^+ \sigma_2^- + \text{H.c.}$ is enabled if $\omega_d = \omega_1 - \omega_2$ and the squeezing term $J_s \sigma_1^+ \sigma_2^+ + \text{H.c.}$ is enabled if $\omega_d = \omega_1 + \omega_2$. Both of the processes are second order with one photon exchange and hence $J_s \sim \frac{2bg_c}{\omega_1+\omega_2}$ and $J_h \sim \frac{2bg_c}{\omega_1-\omega_2}$.

To derive these results explicitly, we first represent the Hamiltonian in the composite Hilbert space $\mathscr{H}_c = \mathscr{H} \otimes \mathscr{T}$, c.f. Eq. (5.16). For $H(t)$ as defined in Eq. (5.54), there are just three Fourier components, c.f. Eq. (5.11),

$$H^{(0)} = H_s, \quad H^{(1)} = \left(H^{(-1)}\right)^* = (b/2)e^{i\theta}\sigma_1^a, \tag{5.55}$$

where $H_s = H_0 + H_c$ is the static Hamiltonian defined in Eq. (5.54). The Floquet Hamiltonian thus $\mathcal{H}_F$ reads,

$$\mathcal{H}_F = \mathcal{H}_{F0} + \mathcal{V}, \tag{5.56}$$

where $\mathcal{H}_{F0}$ is the non-interacting part and $\mathcal{V}$ is the interaction,

$$\begin{aligned} \mathcal{H}_{F0} &= H_0 \otimes F_0 + \omega_d \mathbf{1} \otimes N, \\ \mathcal{V} &= H_c \otimes F_0 + H^{(1)} \otimes F_1 + H^{(-1)} \otimes F_{-1}. \end{aligned} \tag{5.57}$$

The states $|\alpha, n\rangle\rangle = |\alpha\rangle \otimes |n\rangle$ are the eigenstates of $\mathcal{H}_{F0}$ with eigenvalues with quasienergies $\epsilon_{\alpha,n}^{(0)}$,

$$\mathcal{H}_{F0} |\alpha, n\rangle\rangle = \epsilon_{\alpha,n}^{(0)} |\alpha, n\rangle\rangle, \quad \epsilon_{\alpha,n}^{(0)} = E_\alpha + n\omega_d, \tag{5.58}$$

We now discuss the two cases with the transverse ($a = x$) and longitudinal ($a = z$) modulations in the following sections.

Transverse modulation with single photon exchange

For an implementation of parity-breaking interactions $\sigma_1^z\sigma_2^x$, we take the following parameters for modulation,

$$\omega_d = \omega_2, \quad a = x, \quad \theta = 0. \tag{5.59}$$

With this parameters, the states $|\alpha = 1, n-1\rangle\rangle$ and $|\alpha = 2, n\rangle\rangle$ have quasienergies $\epsilon^{(0)}_{1,n-1} = \epsilon^{(0)}_{2,n} = \omega_1 + n\omega_d$, while the states $|\alpha = 3, n-1\rangle\rangle$ and $|\alpha = 4, n\rangle\rangle$ have quasienergies $\epsilon^{(0)}_{3,n-1} = \epsilon^{(0)}_{4,n} = n\omega_d$. We now define a rotating frame $\mathcal{U}_{q1}$ in the composite space $\mathscr{H}_c$ by,

$$\mathcal{U}_{q1} = \exp(-i\omega_1 t\sigma_1^+\sigma_1^- \otimes \mathbf{1}). \tag{5.60}$$

In this frame, the bare Floquet Hamiltonian transforms as $\mathcal{H}_{F0} \to \mathcal{H}_{F0} - \omega_1\sigma_1^+\sigma_1^-$ and the states $|\alpha = 1, n-1\rangle\rangle$, $|\alpha = 2, n\rangle\rangle$, $|\alpha = 3, n-1\rangle\rangle$ and $|\alpha = 4, n\rangle\rangle$ are all degenerate at $\epsilon^{(0)}_{\alpha,n} = n\omega_d$. In particular, the four states $|\alpha = 1, -1\rangle\rangle$, $|\alpha = 2, n = 0\rangle\rangle$, $|\alpha = 3, n = -1\rangle\rangle$ and $|\alpha = 4, n = 0\rangle\rangle$ form a degenerate manifold $\mathcal{S}$ at zero energy. $n = -1$ indicates that degeneracy is gained due to a single photon exchange with the drive. An example of quasienergies of the Floquet Hamiltonian $\mathcal{H}_{F0}$ is shown in Fig. 5.2. The degenerate manifold is separated from higher energy states by a gap of size $\omega_d \gg g_c, b$. Therefore, we eliminate the higher energy states by applying the perturbation toolbox introduced in Sec. 5.2.2 For this single-mode transverse driven system at $\omega_d = \omega_2$, the Slawen matrix has the structure,

$$\begin{bmatrix} h_{11}(\epsilon) & h_{12}(\epsilon) & 0 & 0 \\ h_{21}(\epsilon) & h_{22}(\epsilon) & 0 & 0 \\ 0 & 0 & h_{33}(\epsilon) & h_{34}(\epsilon) \\ 0 & 0 & h_{43}(\epsilon) & h_{44}(\epsilon) \end{bmatrix} \tag{5.61}$$

where $h_{\alpha\beta}$ are defined in Eq. (5.44). Therefore the degenerate manifold $\mathcal{S}$ decouples into two subspaces $\mathcal{S}^{(a)} = \{|\alpha = 1\rangle\rangle, |\alpha = 2\rangle\rangle\}$ and $\mathcal{S}^{(b)} = \{|\alpha = 3\rangle\rangle, |\alpha = 4\rangle\rangle\}$ (As explained in Sec. we drop the photon index n for the degenerate manifold at zero). We can thus solve the self-consistent equation individually in the two

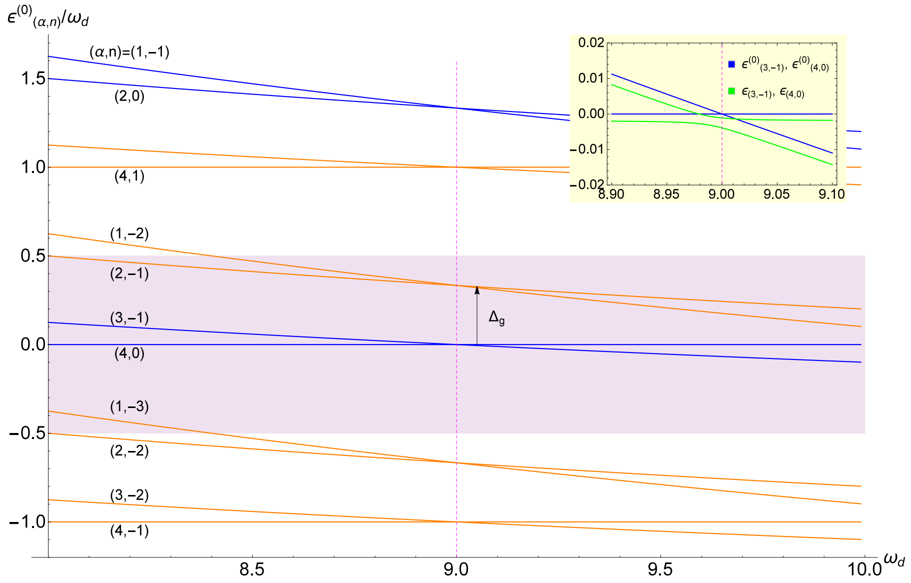

(a)

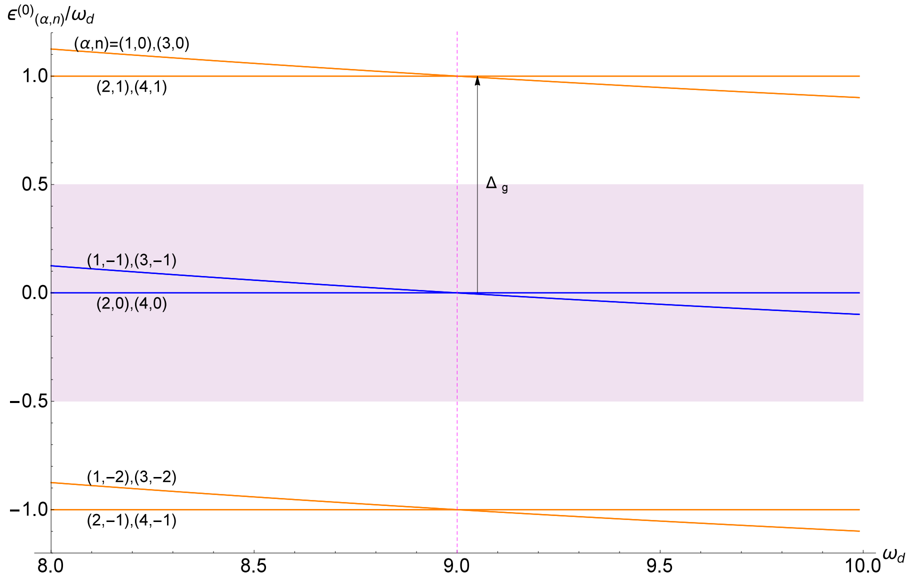

(b)

Figure 5.2: (a) Low-lying quasienergies of the Floquet matrix $\mathcal{H}_{F0}$ as a function of ω_d(GHz) for $\omega_1/(2\pi) = 12$ GHz, $\omega_2/(2\pi) = 9$ GHz. The states with blue color give rise to the effective Hamiltonian in the rotating frame of the qubits. Δ_g is the relevant gap for $\mathcal{H}_{F0}$ which is $\Delta_g \approx \omega_1 - \omega_2$ at the crossing point. The shaded area is the Floquet Brillouin zone. The inset shows the bare and dressed quasienergies of degenerate states at zero energy at the crossing point. (b) Quasienergies in the rotating frame defined with respect to $\omega_1\sigma_1^+\sigma_1^- \otimes \mathbf{1}$. The gap in the rotating frame changes to $\Delta_g \approx \omega_d$ at the crossing point.

subspaces. To make the perturbative ansatz in a single variable b, we introduce $\eta = g_c/b$. For $\mathcal{S}^{(a)}$, the ansatz reads,

$$\epsilon_\alpha = \omega_1 + \delta\epsilon_\alpha, \quad \delta\epsilon_\alpha = \kappa_{\alpha,1} b + \kappa_{\alpha,2} b^2 + O(b^3), \quad \text{for } \alpha = 1, 2, \tag{5.62}$$

where $\kappa_{\alpha,i} \equiv \kappa_{\alpha,i}(\omega_1, \omega_2, \eta)$. With this ansatz, the matrix elements are exact up to fourth order in b. By calculating the matrix elements, we can verify that they are at least second order in the drive amplitude b, which implies that the linear order of b in ϵ_α is zero, i.e. $\kappa_{1,\alpha} = 0$ (we set $\kappa_\alpha = \kappa_{2,\alpha}$ for simplicity). The quasienergies $\delta\epsilon_1$ and $\delta\epsilon_2$ read,

$$\begin{aligned} \delta\epsilon_\alpha = & \frac{-(2+\eta^2)\omega_1 \pm |\eta|\sqrt{(4+\eta^2)}\omega_2}{\omega_1^2 - \omega_2^2} b^2 \\ & - \frac{\kappa_\alpha(2+\eta^2)(\omega_1^2+\omega_2^2) + 2\omega_1(1 \pm \kappa_\alpha|\eta|\sqrt{(4+\eta^2)}\omega_2)}{(\omega_1-\omega_2)^2(\omega_1+\omega_2)^2} b^4, \end{aligned} \tag{5.63}$$

where $\alpha = 1(2)$ for the $+(-)$ sign. The unknown coefficients $\kappa_{\alpha,1}$ are determined by comparing the quasienergy (5.63) and anstaz (5.62),

$$\kappa_\alpha = \frac{-(2+\eta^2)\omega_1 \pm \sqrt{\eta^2(4+\eta^2)}\omega_2}{\omega_1^2 - \omega_2^2}, \quad \alpha = 1(2) \text{ for } +(-). \tag{5.64}$$

The corresponding eigenstates $|u_1\rangle\rangle$ and $|u_2\rangle\rangle$ are,

$$|u_\alpha\rangle\rangle = \frac{1}{\mathcal{N}}\left(\frac{-1 \pm \sqrt{4+\eta^2}}{2}|\alpha = 1\rangle\rangle + |\alpha = 2\rangle\rangle\right) \quad \alpha = 1(2) \text{ for upper(lower) sign}, \tag{5.65}$$

where $\mathcal{N}$ is a normalization pre-factor. For the subspace $\mathcal{S}^{(b)}$ we get,

$$\delta\epsilon_3 = -\delta\epsilon_2, \quad \delta\epsilon_4 = -\delta\epsilon_1, \tag{5.66}$$

and

$$|u_\alpha\rangle\rangle = \frac{1}{\mathcal{N}}\left(\frac{1 \mp \sqrt{4+\eta^2}}{2}|\alpha = 3\rangle\rangle + |\alpha = 4\rangle\rangle\right) \quad \alpha = 3(4) \text{ for } +(-) \text{ sign}. \tag{5.67}$$

The effective Hamiltonian in the composite space can then, after some elementary algebra, be written in terms of spin operators as,

$$\tilde{H}_{eff} = \sum_{\alpha} \epsilon_\alpha \left|u_\alpha\right\rangle\!\rangle \langle\!\left\langle u_\alpha\right| = \left(\frac{\omega_1}{2} + \delta\omega_1\right) \sigma_1^z + \delta\omega_2 \sigma_2^z + J_{zx} \sigma_1^z \sigma_2^x. \tag{5.68}$$

The parameters of the effective Hamiltonian explicitly read,

$$\begin{aligned}
\frac{\delta\omega_1}{\omega_1} &= \frac{(2+\eta^2)}{\omega_1^2 - \omega_2^2} b^2 - \frac{((2+\eta^2)^2 + 2)\omega_1^2 + (3(2+\eta^2)^2 + 10)\omega_2^2}{(\omega_1^2 - \omega_2^2)^3} b^4, \\
\frac{\delta\omega_2}{\omega_2} &= -\frac{\eta^2}{\omega_1^2 - \omega_2^2} b^2 + \frac{\eta^2(2+\eta^2)\omega_2(3\omega_1^2 + \omega_2^2)}{(\omega_1^2 - \omega_2^2)^3} b^4, \\
J_{zx} &= \frac{2\eta\omega_2}{\omega_1^2 - \omega_2^2} b^2 - \frac{2\eta(2+\eta^2)(3\omega_1^2 + \omega_2^2)\omega_2}{(\omega_1^2 - \omega_2^2)^3} b^4.
\end{aligned} \tag{5.69}$$

$\delta\omega_1$ and $\delta\omega_2$ are frequency shifts incurred on the two qubits due to the interaction and J_{zx} is the strength of the effective interaction between the qubits. In order to transform this Hamiltonian back to the Hilbert space $\mathscr{H}$, let us introduce the operator $\mathcal{U}_{q2}$,

$$\mathcal{U}_{q2} = \exp(-i\omega_2 t \sigma_2^+ \sigma_2^- \otimes \mathbf{1}). \tag{5.70}$$

The time-evolution operator in $\mathscr{H}$ is related to the time-evolution operator in the composite space as, c.f. Eq. (5.22),

$$\begin{aligned}
\langle\beta|U(t,t_0)|\alpha\rangle &= \sum_m \langle\!\langle\beta, m|\mathcal{U}_F(t-t_0)|\alpha, n\rangle\!\rangle \, e^{i(m-n)\omega_d t} \\
&= \sum_m \langle\!\langle\beta, m|\mathcal{U}_{q1}^\dagger \mathcal{U}_{q1} \mathcal{U}_F(t-t_0) \mathcal{U}_{q1}^\dagger \mathcal{U}_{q1}|\alpha, n\rangle\!\rangle \, e^{i(m-n)\omega_d t} \\
&= \langle\!\langle\beta|\mathcal{U}_{q1}^\dagger \mathcal{U}_{q2}^\dagger \mathcal{U}_{q1} \mathcal{U}_F(t-t_0) \mathcal{U}_{q1}^\dagger \mathcal{U}_{q2} \mathcal{U}_{q1}|\alpha\rangle\!\rangle \, .
\end{aligned} \tag{5.71}$$

In the second line we used $\mathcal{U}_{q1}^\dagger \mathcal{U}_{q1} = \mathbf{1}$. In the third line we have neglected all states except for the low-energy subspace $\mathcal{S}$ and also used that on this subspace $\mathcal{U}_{q2}$ satisfies, $\mathcal{U}_{q2} \left|\alpha, n\right\rangle\!\rangle = e^{in\omega_d t} \left|\alpha, n\right\rangle\!\rangle$. We can now write the last equation in terms of spin operators on the 4×4 space $\mathcal{S}$. Once truncated to this subspace, the rotating frame operators read,

$$\mathcal{U}_{q1} \to U_{q1} = \exp\left(i\omega_1 t\sigma_1^z/2\right), \quad \mathcal{U}_{q2} \to U_{q2}(t) = \exp\left(i\omega_2 t\sigma_2^z/2\right), \tag{5.72}$$

and thus we can write,

$$\langle\beta|U(t,t_0)|\alpha\rangle = \langle\beta|U_{q1}^\dagger U_{q2}^\dagger U_{eff} U_{q1} U_{q2}|\alpha\rangle\,. \tag{5.73}$$

Note that U_{qi} simply defines the rotating frame of qubit i and therefore $|\alpha^{(r)}\rangle = U_{q1}U_{q2}\,|\alpha\rangle$ is the state $|\alpha\rangle$ transformed to the rotating frame of the qubits. Hence Eq. (5.73) simply reads $\langle\beta|U(t,t_0)|\alpha\rangle = \langle\beta^{(r)}|U_{eff}(t-t_0)|\alpha^{(r)}\rangle$ which means U_{eff} is the time evolution operator in the rotating frame of the qubits,

$$U_{eff} = U_{q1} e^{-i\tilde{H}_{eff}(t-t_0)} U_{q1}^\dagger = e^{-iH_{eff}(t-t_0)}, \tag{5.74}$$

with,

$$H_{eff} = \delta\omega_1\sigma_1^z + \delta\omega_2\sigma_2^z + J_{zx}\sigma_1^z\sigma_2^x, \tag{5.75}$$

the effective Hamiltonian in the rotating frame of the qubits. An example of the parameters of the effective Hamiltonian is given in Tab. 5.1. The expression for J_{zx} (see Eq. (5.69)) shows that the effective interaction to the lowest order is second-order formed from two processes: 1) Single photon exchange with the drive ($\propto b$) and 2) $\sigma_y^{(1)}\sigma_y^{(2)}$ interaction ($\propto g_c = \eta b$). The incurred local detunings of the qubits due to the modulation cause a shift in the resonance in the transition probabilities such that one needs to detune the frequency of the drive accordingly to $\omega_d = \omega_2 + \delta\omega_2$ to get efficient interactions. In Fig. 5.3a, this shift in resonance is shown in the time-averaged transition probability $|00\rangle \to |01\rangle$, see Eq. (5.25) , as a function of external drive frequency ω_d and coupling strength g_c. In Fig. 5.3b, the probability of an erroneous process $|00\rangle \to |10\rangle$ is given for comparison. With the shifted external frequency and in the rotating frame of the qubits with respect to the modified qubit frequencies (i.e. $\omega_i \to \omega_i + \delta\omega_i$ in Eq. (5.72)), the system exhibits a pure interaction $H_{eff} = J_{zx}\sigma_1^z\sigma_2^x$. Analogously, for $\theta \neq 0$ an effective interaction $H_{eff} = J_{eff}\exp(i\theta)\sigma_1^z\sigma_2^+ + \text{H.c.}$ is realized ($J_{eff} \sim J_{zx}$), leading to $H_{eff} =$

	Parameters (MHz)		
	$\delta\omega_1$	$\delta\omega_2$	J_{zx}
Generalized Slawen method (2nd order)	-40.952	-12.857	-21.428
Generalized Slawen method (4th order)	-40.191	-12.499	-20.833
Generalized Slawen method (6th order)	-40.224	-12.513	-20.860
Exact result	-40.222	-12.515	-20.855

Table 5.1: Numerical values for frequency shifts $\delta\omega_i$ $(i = 1, 2)$ and interaction strength J_{zx} in Eq. (5.68) for $\omega_1/(2\pi) = 12$ GHz, $\omega_2/(2\pi) = \omega_d/(2\pi) = 9$ GHz, $b = 250$MHz and $\eta = 1.2$.

$J_{zy}\sigma_1^z\sigma_2^y$ for $\theta = \pi$.

Longitudinal modulation at single photon transition

In this section we discuss how to engineer squeezing and hopping terms in the linear circuit with longitudinal modulation (see Fig. 5.1). For that we change the operating frequency of the external drive. Let us first take the following parameters for the drive (5.53) which are relevant for squeezing,

$$\omega_d = \omega_1 + \omega_2, \quad a = z, \quad \theta = 0. \tag{5.76}$$

At this modulation frequency, the two bare Floquet states $|\alpha = 1, n = -1\rangle\rangle$ and $|\alpha = 4, n = 0\rangle\rangle$ are resonantly coupled through a single photon transition and the relevant manifold for the effective Hamiltonian is $\mathcal{S} = \{|\alpha = 1, n = -1\rangle\rangle$, $|\alpha = 4, n = 0\rangle\rangle$, $|\alpha = 2, n = -1\rangle\rangle$ and $|\alpha = 3, n = 0\rangle\rangle\}$. These states have quasienergies $\epsilon_1^{(0)} = \epsilon_4^{(0)} = 0$, $\epsilon_2^{(0)} = -\omega_2$ and $\epsilon_3^{(0)} = \omega_2$. In the rotating frame defined by $\mathcal{U}_- = \exp\left(i\omega_2 t/2(\sigma_1^z - \sigma_2^z) \otimes \mathbf{1}\right)$ these states form a degenerate manifold $\mathcal{S}$ at zero frequency. The rotating frame $\mathcal{U}_-$ is identical to the rotating frame of the qubits in the Hilbert space. The Salwen matrix on the subspace $\mathcal{S}$ takes the following form,

$$\begin{bmatrix} h_{11}(\epsilon) & 0 & 0 & h_{14}(\epsilon) \\ 0 & h_{22}(\epsilon) & h_{23}(\epsilon) & 0 \\ 0 & h_{32}(\epsilon) & h_{33}(\epsilon) & 0 \\ h_{41}(\epsilon) & 0 & 0 & h_{44}(\epsilon) \end{bmatrix} \tag{5.77}$$

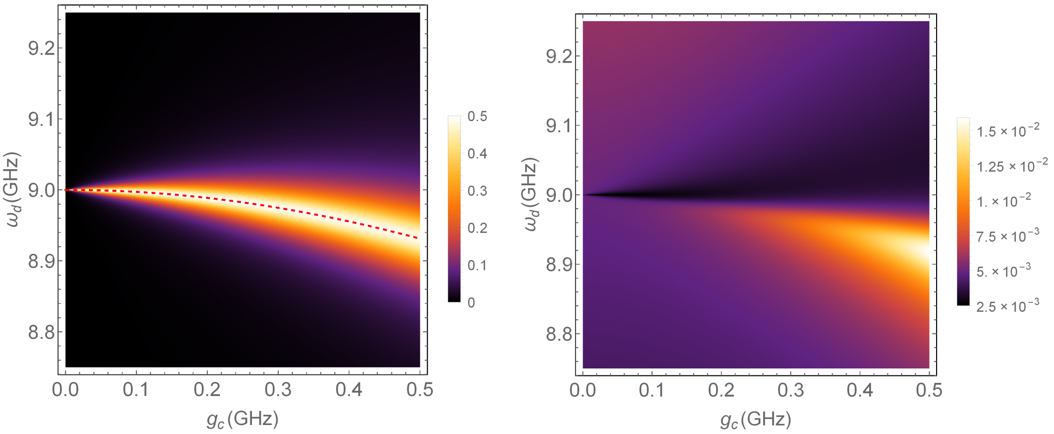

(a) **(b)**

Figure 5.3: (a) Time-averaged transition probability $\overline{\overline{P}}_{|00\rangle\rightarrow|01\rangle}$ as a function of external drive frequency ω_d and g_c. The resonance is due to the effective interaction $\sigma_z^1\sigma_y^2$ at single photon transition. The dashed line is the resonance condition $\omega_d = \omega_2 + \delta\omega_2$ in which $\delta\omega_2$ is given by Eq. (5.69). (b) Time-averaged transition probability of unwanted process $\overline{\overline{P}}_{|00\rangle\rightarrow|10\rangle}$ which is closest to resonance. $\omega_1/(2\pi) = 12$ GHz, $\omega_2/(2\pi) = 9$ GHz and $b = 150$ MHz.

This matrix leads to two sets of decoupled equations on the subspaces $\mathcal{S}^{(a)}$ and $\mathcal{S}^{(b)}$. In contrast to the transverse modulation, in which a single-photon transition couples the states $|\alpha = 1\rangle\rangle$ and $|\alpha = 2\rangle\rangle$, here the state $|\alpha = 1\rangle\rangle$ is coupled to $|\alpha = 4\rangle\rangle$ through a single-photon transition to enable squeezing. The effective Hamiltonian for squeezing thus reads,

$$H_{eff} = \delta\omega_1\sigma_1^z + \delta\omega_2\sigma_2^z + J_s(\sigma_1^+\sigma_2^+ + \text{H.c.}), \tag{5.78}$$

with the parameters,

$$\begin{aligned}
\delta\omega_1 &= -\frac{b^2\eta^2\omega_1}{\omega_1^2-\omega_2^2} - \frac{b^4\eta^2((2+\eta^2)\omega_1^4 - 4\omega_1^3\omega_2 + (1+3\eta^2)\omega_1^2\omega_2^2 + \omega_2^4)}{\omega_1(\omega_1^2-\omega_2^2)^3} + O(b^6),\\
\delta\omega_2 &= \frac{-b^2\eta^2\omega_2}{\omega_1^2-\omega_2^2} + \frac{b^4\eta^2\omega_2((2+3\eta^2)\omega_1^3 - 5\omega_1^2\omega_2 + (2+\eta^2)\omega_1\omega_2^2 + \omega_2^3)}{\omega_1(\omega_1^2-\omega_2^2)^3} + O(b^6),\\
J_s &= \frac{2b^2\eta}{\omega_1+\omega_2} - \frac{2b^4\eta(2+\eta^2)}{(\omega_1+\omega_2)^3} + O(b^6).
\end{aligned} \tag{5.79}$$

As an example, for $\omega_1/(2\pi) = 12$ GHz, $\omega_2/(2\pi) = 9$ GHz, $b = 200$ MHz and $g_c = 500$ MHz ($\eta = 2.5$), we get to the fourth order in the drive amplitude b, $\delta\omega_1/(2\pi) = 46.46$ MHz (exact result: 46.52 MHz), $\delta\omega_2/(2\pi) = -34.57$ MHz (exact: -34.63 MHz) and $J_s = 9.51$ MHz (exact: 9.51 MHz).

Alternatively, for engineering a hopping interaction, the parameters of the drive (5.53) are chosen as follows,

$$\omega_d = |\omega_1 - \omega_2|, \quad a = z, \quad \theta = 0. \tag{5.80}$$

For these parameters, the states in the manifold $\mathcal{S} = \{|\alpha = 1, n = -1\rangle\rangle, |\alpha = 4, n = 0\rangle\rangle, |\alpha = 2, n = -1\rangle\rangle, |\alpha = 3, n = 0\rangle\rangle\}$ have quasienergies $\epsilon_2^{(0)} = \epsilon_3^{(0)} = 0$, $\epsilon_1^{(0)} = \omega_2$ and $\epsilon_4^{(0)} = -\omega_2$ and become degenerate at zero energy in the rotating frame defined by $\mathcal{U}_+ = \exp\left(i\omega_2 t/2(\sigma_1^z + \sigma_2^z) \otimes \mathbf{1}\right)$. Again, this rotating frame coincides with the rotating frame of the qubits in $\mathscr{H}$. The effective Hamiltonian for the hopping is then derived to be,

$$H_{eff} = \delta\omega_1\sigma_1^z + \delta\omega_2\sigma_2^z + J_h(\sigma_1^+\sigma_2^- + \text{H.c.}), \tag{5.81}$$

with,

$$\begin{aligned}
\delta\omega_1 &= \frac{b^2\eta^2\omega_1}{\omega_1^2 - \omega_2^2} - \frac{b^4\eta^2((2+\eta^2)\omega_1^4 + 4\omega_1^3\omega_2 + (1+3\eta^2)\omega_1^2\omega_2^2 + \omega_2^4)}{\omega_1(\omega_1^2 - \omega_2^2)^3} + O(b^6),\\
\delta\omega_2 &= \frac{-b^2\eta^2\omega_2}{\omega_1^2 - \omega_2^2} + \frac{b^4\eta^2\omega_2((2+3\eta^2)\omega_1^3 + 5\omega_1^2\omega_2 + (2+\eta^2)\omega_1\omega_2^2 - \omega_2^3)}{\omega_1(\omega_1^2 - \omega_2^2)^3} + O(b^6),\\
J_h &= \frac{-2b^2\eta}{\omega_1 - \omega_2} - \frac{2b^4\eta(2+\eta^2)}{(\omega_1 - \omega_2)^3} + O(b^6).
\end{aligned} \tag{5.82}$$

For $\omega_1/(2\pi) = 12$ GHz, $\omega_2/(2\pi) = 9$ GHz and $g_c = 250$ MHz and $b = 100$ MHz, we get $\delta\omega_1/(2\pi) = 11.80$ MHz, $\delta\omega_2/(2\pi) = -8.83$ MHz and $J_h = -16.51$ MHz.

For a $\theta \neq 0$ one could also incorporate a static gauge field into the squeezing or hopping i.e. $J_s \to J_s e^{i\theta}$ and $J_h \to J_h e^{i\theta}$.

5.3.2 Bimodally driven system

In this section, we discuss scenarios in which both qubits in the linearly coupled circuit are driven by a bimodal drive. A bimodal drive in the driven qubit scheme refers to a quasiperiodic Hamiltonian of the form,

$$H_d(t) = W_1(t)\sigma_1^a + W_2(t)\sigma_2^a, \quad a = x, z. \tag{5.83}$$

with,

$$W_i(t) = \sum_{j=1,2} b_{ij}\cos(\omega_{dj}t + \theta_{ij}), \quad i = 1, 2, \tag{5.84}$$

where ω_{d1} and ω_{d2} are *incommensurate* frequencies,

$$\omega_{d1} = \omega_1 + \omega_2, \quad \omega_{d2} = \omega_1 - \omega_2. \tag{5.85}$$

The total Hamiltonian for a bimodally driven circuit reads,

$$H(t) = H_s + H_d(t), \tag{5.86}$$

where H_s is defined in Eq. (5.48). Based on the many-mode Floquet theory discussed in Sec. 5.1.2, the time-independent representation of this quasiperiodic Hamiltonian in the composite space $\mathscr{H}_c = \mathscr{H} \otimes \mathscr{T}_1 \otimes \mathscr{T}_2$ is given by,

$$\begin{aligned} \mathcal{H}_F &= \mathcal{H}_{F0} + \mathcal{V}, \\ \mathcal{H}_{F0} &= H_0 \otimes F_0 \otimes F_0 + \omega_1 N \otimes F_0 + \omega_2 F_0 \otimes N, \\ \mathcal{V} &= H_0 \otimes F_0 \otimes F_0 + \sum_{j=1,2}(h_j^{(1)} \otimes F_1 \otimes F_1 + h_j^{(2)} \otimes F_1 \otimes F_{-1} + \text{H.c.}), \end{aligned} \tag{5.87}$$

where $h_j^{(k)} = (b_{jk}/2)\exp(i\theta_{jk})\sigma_j^a$, $a = x$ for the transverse driving scheme, $a = z$ for the longitudinal driving scheme, c.f. Eq. (5.83), and the Fourier space operators F_n and N are defined in Eq. (5.15). The Floquet states $|\alpha, n_1, n_2\rangle\rangle = |\alpha\rangle \otimes |n_1\rangle \otimes |n_2\rangle$ are the eigenstates of the bare Floquet matrix $\mathcal{H}_{F0}$ with quasienergies, $\epsilon^{(0)}_{\alpha,n_1,n_2} = \epsilon^{(0)}_\alpha + n_1\hbar\omega_{d1} + n_2\hbar\omega_{d2}$, c.f. Eq. (5.52). In particular, the four states $|\alpha = 1\rangle\rangle \equiv |\alpha = 1, n_1 = -1, n_2 = -1\rangle\rangle$, $|\alpha = 2\rangle\rangle \equiv |\alpha = 2, n_1 = -1, n_2 = 0\rangle\rangle$, $|\alpha = 3\rangle\rangle \equiv |\alpha = 3, n_1 = 0, n_2 = -1\rangle\rangle$ and $|\alpha = 4\rangle\rangle \equiv$

$|\alpha = 4, n_1 = 0, n_2 = 0\rangle\rangle$ have energy zero and there is a gap of size $\omega_1 - \omega_2$ between these degenerate states and other higher energy states. In particular note that for the bimodally driven circuit we do not need to transform to a rotating frame as the states that give rise to the effective Hamiltonian have zero energy in the Floquet matrix. For finite interactions such that $|g_c|, |b_{ij}| \ll \omega_1 - \omega_2$, the effective dynamics is described by these sates and we can adiabatically eliminate all Floquet states except for the four in the low-energy manifold. For the derivation of the effective Hamiltonian one calculates the scattering matrix T using the Green's function $\mathcal{G}_{\mathcal{P}}$ and perturbation $\mathcal{V}$ as in Sec. 5.2.2. We now apply this procedure to the two types of perturbations, transverse and longitudinal bimodal modulation.

Longitudinal driving scheme

The drive Hamiltonian for this scheme reads,

$$H_d(t) = \sum W_i(t)\sigma_i^z, \tag{5.88}$$

where $W_i(t)$ is defined in Eq. (5.84). In this case the structure of the Salwen matrix is the same as in Eq. (5.77), where the subspace spanned by $\mathcal{S}^{(a)} = \{|\alpha = 1\rangle\rangle, |\alpha = 4\rangle\rangle\}$ decouples from that spanned by $\mathcal{S}^{(b)} = \{|\alpha = 2\rangle\rangle, |\alpha = 3\rangle\rangle\}$ and we can solve for quasienergies in each subspace independently. Let us first assume $\theta_1 = \theta_2 = 0$. In order to expand in a single variable, we define $b = g_c$ and $\eta_{ij} = b_{ij}/b$.

Using the ansatz of Eq.(5.43) for the quasienergies and expanding the matrix elements, one can verify that $\kappa_{\alpha,1} = 0$ and $\kappa_{\alpha,2} = \pm b^2/(\omega_1 + \omega_2) + O(b^4)$ (for the two states of $\mathcal{S}^{(a)}$, $+(-)$ for $\alpha = 1(4)$) and $\kappa_{\alpha,2} = \pm b^2/(\omega_1 - \omega_2) + O(b^4)$ (for $\mathcal{S}^{(b)}$, $+(-)$ for $\alpha = 2(3)$). Including $\kappa_{\alpha,2}$, the effective Hamiltonian is exact to fourth order in b and reads,

$$H_{eff} = \delta\omega_1\sigma_1^z + \delta\omega_2\sigma_2^z + J_{xx}\sigma_1^x\sigma_2^x + J_{yy}\sigma_1^y\sigma_2^y \tag{5.89}$$

	Parameters (MHz)		
	$\delta\omega_1$	$\delta\omega_2$	J_{xx}
Generalized Slawen method (2nd order)	15.052	−10.662	13.170
Generalized Slawen method (4th order)	14.942	−10.557	13.129
Exact result	14.944	−10.559	13.129

Table 5.2: Numerical values for frequency shifts $\delta\omega_i$ $(i = 1, 2)$ and interaction strength (J_{xx}). Parameters: $\omega_1/(2\pi) = 12GHz$, $\omega_2/(2\pi) = 8.5GHz$, $b = 300MHz$, $\eta_{11} = \eta_{21} = 0.75$, $\eta_{12} = 0.256$, $\eta_{22} = 0$.

where,

$$\begin{aligned}
\delta\omega_1 &= \frac{b^2\omega_1}{\omega_1^2-\omega_2^2} + O(b^4),\\
\delta\omega_2 &= -\frac{b^2\omega_2}{\omega_1^2-\omega_2^2} + O(b^4),\\
J_{xx} &= b^2\left(\frac{-\eta_{12}+\eta_{22}}{\omega_1-\omega_2} + \frac{\eta_{11}+\eta_{21}}{\omega_1+\omega_2}\right) + O(b^4),\\
J_{yy} &= b^2\left(\frac{\eta_{12}-\eta_{22}}{\omega_1-\omega_2} + \frac{\eta_{11}+\eta_{21}}{\omega_1+\omega_2}\right) + O(b^4).
\end{aligned} \tag{5.90}$$

To leading order in b, the frequency shifts $\delta\omega_i$ are independent from the external modulations and originate from the capacitive coupling. These shifts can be absorbed in the effective Hamiltonian by detuning the external drives according to $\omega_{d1} \to \omega_{d1} + \delta\omega_1 + \delta\omega_2$ and $\omega_{d2} \to \omega_{d2} + \delta\omega_1 - \delta\omega_2$, which sets the external drives back into resonance with the desired processes. The rotating frame of the qubits also needs to be re-defined with respect to the modified frequencies, i.e. $\omega_i \to \omega_i + \delta\omega_i$. By choosing the values for η_{ij} such that $(\eta_{12} - \eta_{22})/(\omega_1 - \omega_2) = -(\eta_{11} + \eta_{21})/(\omega_1 + \omega_2)$, $J_{yy} \sim 0$ and the interaction is purely $\sigma_1^x\sigma_2^x$. On the one hand, if $(\eta_{12} - \eta_{22})/(\omega_1 - \omega_2) = (\eta_{11} + \eta_{21})/(\omega_1 + \omega_2)$, then $J_{yy} \sim 0$ and a pure $\sigma_1^y\sigma_2^y$ interaction is implemented. On the other hand, for $\theta_{ji} = \pi/2$, the effective Hamiltonian takes the form,

$$H_{eff} = \delta\omega_1\sigma_1^z + \delta\omega_2\sigma_2^z + J_{xy}\sigma_1^x\sigma_2^y + J_{yx}\sigma_1^y\sigma_2^x. \tag{5.91}$$

The parameters of this Hamiltonian can be obtained from Eq. (5.90) by replacing $J_{xx} \to J_{xy}$ and $J_{yy} \to J_{yx}$.

Transverse driving scheme

This scheme is implemented using of a bimodal drive of the form (c.f. Eq. (5.84)),

$$H_d(t) = \sum W_i \sigma_i^x. \tag{5.92}$$

In this case, the off-diagonal elements of the effective matrix are zero, and therefore the effective Hamiltonian is,

$$H_{eff} = \delta\omega_1 \sigma_1^z + \delta\omega_2 \sigma_2^z + J_{zz} \sigma_1^z \sigma_2^z. \tag{5.93}$$

To the third order in b the parameters read,

$$\begin{aligned}
\delta\omega_1 &= \frac{-b^2(\eta_1^2 - \eta_2^2)}{\omega_2} + \frac{b^2\omega_1}{\omega_1^2 - \omega_2^2} + \frac{b^2(\eta_1^2(2\omega_1 - \omega_2) + \eta_2^2(2\omega_1 + \omega_2)}{4\omega_1^2 - \omega_2^2} + O(b^4),\\
\delta\omega_2 &= \frac{-b^2(\eta_3^2 - \eta_4^2)}{\omega_1} - \frac{b^2\omega_2}{\omega_1^2 - \omega_2^2} + \frac{b^2(\eta_3^2(\omega_1 - 2\omega_2) - \eta_4^2(\omega_1 + 2\omega_2)}{\omega_1^2 - 4\omega_2^2} + O(b^4),\\
J_{zz} &= \frac{4b^3(\eta_1\eta_3 - \eta_2\eta_4)}{\omega_1\omega_2} + \frac{4b^3\eta_2\eta_4}{3\omega_1(2\omega_1 - \omega_2)} + \frac{4b^3\eta_1\eta_3}{3\omega_1(2\omega_1 + \omega_2)}\\
&\qquad - \frac{8b^3\eta_2\eta_4}{3\omega_1(\omega_1 - 2\omega_2)} - \frac{8b^3\eta_1\eta_3}{3\omega_1(\omega_1 + 2\omega_2)} + O(b^4).
\end{aligned} \tag{5.94}$$

For $\omega_1/(2\pi) = 9\text{GHz}$, $\omega_2/(2\pi) = 5\text{GHz}$, $b = 400$ MHz, $\eta_1 = \eta_3 = 0.6$ and $\eta_2 = \eta_4 = 0$, we get $J_{zz} = 1.8\text{MHz}$.

5.4 Driven coupling schemes

In Sec. 5.3, we considered two linearly coupled qubits, where one or both of the qubits are driven via single-mode or bimodal perturbations. In this section, we turn to a different circuit, namely two qubits with nonlinear coupling where instead of the qubits, we apply the modulation to the coupler [62]. This circuit is shown in Fig. 5.4. Here we have two transmons with Josephson energies E_{Jj} and capacitances C_j, coupled via a dc-SQUID with total Josephson energy E_{Js} and total capacitance C_s, that is threaded by an external flux ϕ_{ext}. The

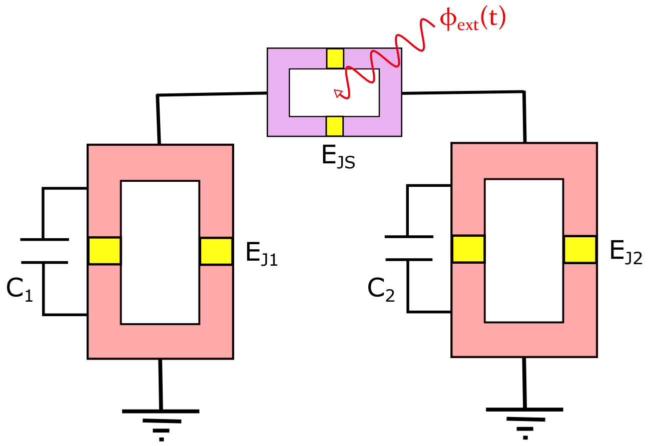

Figure 5.4: Two transmon qubits coupled via a nonlinear driven coupling.

Hamiltonian of the circuit reads,

$$H = \sum_{j=1,2} \left(E_{Jj}\cos(\phi_j) + E_{cj}n_j^2\right) + E_{cc}n_1 n_2 - E_{Js}\cos(\phi_{ext}/2)\cos(\phi_1 - \phi_2). \tag{5.95}$$

Note that this circuit has the same Hamiltonian as the linear circuit, see. Eq. (5.46), except that we have now added the contribution of the Josephson junctions of the coupling SQUID, i.e. the last term in Eq. (5.95). The capacitive energy scales are given in Eq. (5.47). We further assume that the external flux is composed of a dc-part ϕ_{dc} and an oscillating quasiperiodic part $W(t)$,

$$\begin{aligned} \phi_{ext}(t) &= \phi_{dc} + W(t), \\ W(t) &= 2\phi_{ac,1}\cos(\omega_{d1}t + \theta) + 2\phi_{ac,2}\cos(\omega_{d2}t), \end{aligned} \tag{5.96}$$

where $\omega_{d1} = \omega_1 + \omega_2$, $\omega_{d2} = \omega_1 - \omega_2$ and for $\phi_{ac} \ll \phi_{dc}$, we have $\cos(\phi_{ext}/2) \approx \cos(\phi_{dc}/2) - \sin(\phi_{dc}/2)W(t)$. In the single excitation subspace, the quantized Hamiltonian reads,

$$\begin{aligned} H &= H_0 + H_d(t), \\ H_0 &= \sum_{j=1,2} \omega_j \sigma_j^+ \sigma_j^- + g_c \sigma_1^y \sigma_2^y, \\ H_d(t) &= \left[\cos(\phi_{dc}/2) - \sin(\phi_{dc}/2)W(t)\right] H_1, \end{aligned} \tag{5.97}$$

with,

$$H_1 = \sum_{j=1,2} g_j \sigma_j^+ \sigma_j^- + g_x \sigma_1^x \sigma_2^x + g_z \sigma_1^z \sigma_2^z, \tag{5.98}$$

and

$$g_j = E_{Js} \overline{\phi}_j^2 /2, \quad g_x = -E_{Js} \overline{\phi}_1 \overline{\phi}_2, \quad g_z = -E_{Js} \overline{\phi}_1^2 \overline{\phi}_2^2 /4, \quad g_c = E_{cc}/(4\overline{\phi}_1 \overline{\phi}_2), \tag{5.99}$$

where $\overline{\phi}_j$ is the zero-point fluctuation amplitude of qubit j. We here assume a weak capacitive coupling, $|g_c| \ll |g_x|, |g_z|, |g_j|$, and neglect g_c in what follows, hence $H_0 = \sum_{j=1,2} \omega_j \sigma_j^+ \sigma_j^-$.

To discuss the generation of effective spin-spin interactions in this circuit, we first outline the idea using a more heuristic argument based on a Rotating Wave Approximation and then turn to derive more precise expressions with our Floquet engineering approach.

5.4.1 Rotating Wave Approximation (RWA)

Let us first assume that the oscillating drive is turned off, $\phi_{ac,1} = \phi_{ac,2} = 0$. In this case, the Hamiltonian reads $H = \sum_{j=1,2} \tilde{\omega}_j \sigma_j^+ \sigma_j^- + \tilde{g}_x \sigma_1^x \sigma_2^x + \tilde{g}_z \sigma_1^z \sigma_2^z$, where $\tilde{\omega}_j = \omega_j + \cos(\phi_{dc}/2) g_j$ is the modified qubit transition frequency and $\tilde{g}_x = \cos(\phi_{dc}/2) g_x$ and $\tilde{g}_z = \cos(\phi_{dc}/2) g_z$. In the rotating frame of the qubits defined by $U_{qj} = \exp(-i\tilde{\omega}_j t \sigma_j^+ \sigma_j^-)$, the Hamiltonian and the spin operators transform as $H \to H - \sum_{j=1,2} \tilde{\omega}_j \sigma_j^+ \sigma_j^-$ and $\sigma_j^\pm \to \exp(\pm i \tilde{\omega}_j t) \sigma_j^\pm$. Therefore, the term $\tilde{g}_x \sigma_1^x \sigma_2^x$ rotates at the two frequencies $\tilde{\omega}_{d+} = \tilde{\omega}_1 + \tilde{\omega}_2$ and $\tilde{\omega}_{d-} = |\tilde{\omega}_1 - \tilde{\omega}_2|$. Provided $|\tilde{g}_x| \ll \tilde{\omega}_{d+}, \tilde{\omega}_{d-}$, which we choose to be the case, we can therefore discard it. The Hamiltonian is then well-approximated by the non-rotating term $H \approx \tilde{g}_z \sigma_1^z \sigma_2^z$.

If instead, we apply the oscillating flux described in Eq. (5.96) and set $\phi_{dc} = \pi$, the term $\sigma_j^+ \sigma_j^-$ and $\sigma_1^z \sigma_2^z$ in H_1 rotate at the frequencies ω_{d1} and ω_{d2} in the rotating frame of the qubits due to the rotating prefactor. For $g_j, g_z \ll \omega_{d1}, \omega_{d2}$ these terms can then be neglected in a rotating wave approximation. The only non-rotating contribution is then given by the term $W(t) g_x \sigma_1^x \sigma_2^x$, which, in the rotating frame, reads

$$F(t)g_x\sigma_1^x\sigma_2^x \xrightarrow{U_{q1}U_{q2}} e^{i\theta}g_x\phi_{ac,1}\sigma_1^+\sigma_2^+ + g_x\phi_{ac,2}\sigma_1^+\sigma_2^- + \text{H.c.} + \text{r.t.}. \tag{5.100}$$

Here r.t. refers to other rotating terms which oscillate at $2\omega_{dj}$ and $2\omega_j$ for $j = 1, 2$. Under the assumption that $g_x \ll 2\omega_j$, we can drop these fast-oscillating terms and H can be approximated by,

$$H \approx e^{i\theta}g_x\phi_{ac,1}\sigma_1^+\sigma_2^+ + g_x\phi_{ac,2}\sigma_1^+\sigma_2^- + \text{H.c.}. \tag{5.101}$$

Therefore if $\phi_{ac} = \phi_{ac,1} = \phi_{ac,2}$, we get $H \approx b\sigma_1^x\sigma_2^x$ for $\theta = 0$ and $H \approx b\sigma_1^y\sigma_2^y$ for $\theta = \pi$, where $b = g_x\phi_{ac}$ is the effective interaction strength. We also note that for the two single mode driving cases, $\phi_{ac,1} = 0$ or $\phi_{ac,2} = 0$ a hopping or a squeezing term would be enabled.

5.4.2 Beyond RWA: Bimodal Floquet Theory

We now derive more accurate expressions for the effective interactions generated by the drive described in Eq. (5.96) via our Floquet engineering approach. The infinite-dimensional matrix H_F to represent this bimodal driven in the Floquet space reads,

$$\begin{aligned} &H_F = H_{F0} + H_{F1}, \\ &H_{F0} = H_0 \otimes F_0 \otimes F_0 + \omega_1 N \otimes F_0 + \omega_2 F_0 \otimes N, \\ &H_{F1} = \phi_{ac,1}H_1 \otimes F_1 \otimes F_1 + e^{i\theta}\phi_{ac,2}H_1 \otimes F_1 \otimes F_{-1} + \text{H.c.}. \end{aligned} \tag{5.102}$$

In the limit $|g_j|, |g_x|, |g_z| \ll |\omega_1 - \omega_2|$, we can derive an effective Hamiltonian in terms of the four states $|\alpha = 1\rangle\rangle \equiv |\alpha = 1, m_1 = -1, m_2 = -1\rangle\rangle$, $|\alpha = 2\rangle\rangle \equiv |\alpha = 2, m_1 = -1, m_2 = 0\rangle\rangle$, $|\alpha = 3\rangle\rangle \equiv |\alpha = 3, m_1 = 0, m_2 = -1\rangle\rangle$ and $|\alpha = 4\rangle\rangle \equiv |\alpha = 4, m_1 = 0, m_2 = 0\rangle\rangle$. Using Salwen's method, the effective matrix again decouples into two subspaces $S_1 = \{|\alpha = 1\rangle\rangle, |\alpha = 4\rangle\rangle\}$ and $S_2 = \{|\alpha = 2\rangle\rangle, |\alpha = 3\rangle\rangle\}$. For $\phi_{ac} = \phi_{ac,1} = \phi_{ac,2}$ and $\theta = 0$, we get the following quasienergies for these subspaces,

$$\begin{aligned}\epsilon_\alpha &= b - \left(\frac{1}{\omega_1^2} + \frac{1}{\omega_2^2} + \frac{32\eta_\alpha^2}{(\omega_1-\omega_2)^2} + \frac{1+16\eta_\alpha^2}{(\omega_1+\omega_2)^2}\right)b^3 + O(b^5), \quad \alpha = 1,2,\\ \epsilon_\alpha &= -b - \left(\frac{3}{\omega_1^2} + \frac{3}{\omega_2^2} + \frac{32\eta_\alpha^2}{(\omega_1-\omega_2)^2} + \frac{3+16\eta_\alpha^2+32\eta_z^2}{(\omega_1+\omega_2)^2}\right)b^3 + O(b^5), \quad \alpha = 3,4.\end{aligned} \tag{5.103}$$

where $\eta_1 = \eta_4 = (g_1 - g_2)/g_x$, $\eta_2 = \eta_3 = (g_1 + g_2)/g_x$, $\eta_z = g_z/g_x$, $b = g_x\phi_{ac}$. The effective Hamiltonian thus reads,

$$H_{eff} = \delta\omega_1\sigma_1^z + \delta\omega_2\sigma_2^z + J_{xx}\sigma_1^x\sigma_2^x + J_{yy}\sigma_1^y\sigma_2^y, \tag{5.104}$$

and the parameters of this Hamiltonian to third order in b are,

$$\begin{aligned}\delta\omega_1 &= \frac{b^2}{4}\left(\frac{2}{\omega_1} + \frac{1}{\omega_1-\omega_2} + \frac{1}{\omega_1+\omega_2}\right) - 2b^3(\eta_1-\eta_2)\eta_z\left(\frac{1}{\omega_1-\omega_2} + \frac{1}{\omega_1+\omega_2}\right),\\ \delta\omega_2 &= \frac{b^2}{4}\left(\frac{2}{\omega_2} - \frac{1}{\omega_1-\omega_2} + \frac{1}{\omega_1+\omega_2}\right) - 2b^3(\eta_1+\eta_2)\eta_z\left(\frac{1}{\omega_1-\omega_2} + \frac{1}{\omega_1+\omega_2}\right),\\ J_{xx} &= b + b^3\left(\frac{2\eta_z^2-\eta_1^2}{(\omega_1-\omega_2)^2} + \frac{2\eta_z-\eta_2^2}{(\omega_1+\omega_2)^2}\right),\\ J_{yy} &= b^3\left(\frac{\eta_1^2}{(\omega_1-\omega_2)^2} + \frac{1}{2\omega_1\omega_2} - \frac{\eta_2^2}{(\omega_1-\omega_2)^2}\right).\end{aligned} \tag{5.105}$$

The effective Hamiltonian (5.104) differs from the Hamiltonian (5.101), that was based on the rotating wave approximation, in two aspects: it contains frequency shifts on the qubits and interaction terms of third order (and higher). For $\theta = 0$, we can eliminate the $\sigma_1^y\sigma_2^y$ interaction by assuming a slight difference in the driving amplitudes, i.e. by choosing $\phi_{ac,1} = \phi_{ac}$ and $\phi_{ac,2} = \phi_{ac} + \delta\phi_{ac}$. To linear order in $\delta\phi_{ac}$, the strength of the $\sigma_1^y\sigma_2^y$ interaction is then given by,

$$\begin{aligned}J_{yy} &= \left.J_{yy}\right|_{\delta\phi_{ac}=0} + D_y\delta\phi_{ac} \equiv 0,\\ D_y &= \frac{g_x}{2}\left(1 + \frac{3b^2}{2\omega_1\omega_2} + \frac{6b^2\eta_z^2}{(\omega_1-\omega_2)^2} + \frac{6b^2(\eta_2^z-\eta_2^2)}{(\omega_1+\omega_2)^2}\right) \approx g_x/2,\end{aligned} \tag{5.106}$$

where $J_{yy}|_{\delta\phi_{ac}=0}$ is given in Eq. (5.105). Hence for an amplitude mismatch of $\delta\phi_{ac} \approx 2J_{yy}/g_x$, the yy-interaction is suppressed leading to $J_{yy} = 0$.

5.5 Summary

In this chapter, we introduced a setting for analog implementation of a complete set of spin-spin interactions in coupled transmon circuits. To this end, we employed the time independent formalism of periodically and quasi-periodically quantum systems in a composite Hilbert space. The time-dependent system can therefore be written in a matrix form and the desired states which contribute in a specific two-body interaction, appear as the low-energy manifold of that matrix. We presented a generic procedure to derive an effective Hamiltonian in terms of the low-energy states and proved that this Hamiltonian indeed describes the low-energy behaviour of the original quantum system in the rotating frame of the qubits. We discussed several single-mode and bimodal schemes to realize different spin-spin interactions in transmon circuits with driven qubits and driven nonlinear coupling.

In the next chapter, we show that the modulation schemes can be employed to simulate the Kitaev honeycomb model with superconducting circuits.

Chapter 6

Quantum simulation of Kitaev honeycomb lattice model

In this chapter, we use the engineered spin-spin couplings introduced in Chap. 5 to implement the Kitaev honeycomb model [155] with superconducting circuits. This model is a frustrated spin model with two-body interactions which exhibits rich topological properties. For a specific parameter regime, it behaves as a toric code and gives rise to abelian anyons. There is another parameter regime for which the model is gapless. In this regime, the excitations are non-abelian anyons and the model also supports Majorana zero-mode fermions [156] binding to vortices on the lattice [157]. In this chapter, we first give an introduction to the honeycomb model in Sec. 6.1 and then present our approach to implement it with superconducting circuit using two driving schemes, namely driven qubit and driven coupling schemes.

6.1 Kitaev Honeycomb lattice model

In the Kitaev honeycomb lattice model [155], the degrees of freedom are spins living on the vertices of a honeycomb lattice, see Fig. 6.1. Each spin is coupled to its three nearest neighbors through three different types of interactions $\sigma^x\sigma^x$, $\sigma^y\sigma^y$ and $\sigma^z\sigma^z$. These interactions are shown as color coded links in Fig. 6.1.

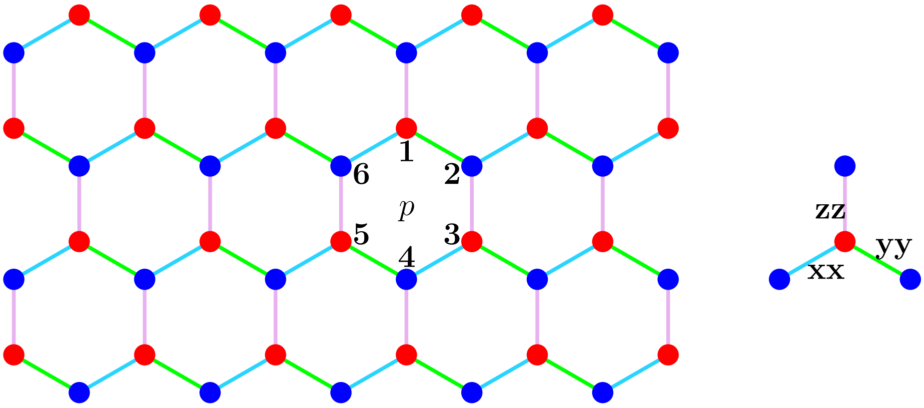

Figure 6.1: The Kitaev honeycomb lattice model. Spins sitting on the vertices of a honeycomb lattice constitute the degrees of freedom of the model. Each spin interacts via 3 different color coded interactions xx, yy and zz with nearest neighbors. The spins of a plaquette p are labelled from 1 to 6.

The Hamiltonian of the model reads,

$$H = -J_{xx} \sum_{\text{blue links}} \sigma_i^x \sigma_j^x - J_{yy} \sum_{\text{green links}} \sigma_i^y \sigma_j^y - J_{zz} \sum_{\text{pink links}} \sigma_i^z \sigma_j^z. \tag{6.1}$$

For each honeycomb cell, one can define a *plaquette operator*, see Fig. 6.1,

$$W_p \equiv \sigma_1^z \sigma_2^x \sigma_3^y \sigma_4^z \sigma_5^x \sigma_6^y. \tag{6.2}$$

These operators square to the identity and their corresponding eigenvalues read,

$$w_p = \pm 1. \tag{6.3}$$

The eigenvalue $w_p = -1$ is associated to a vortex on the plaquette p. We note that plaquette operators commute with each other and also with the Hamiltonian (6.1) which means that they are constants of motion.

$$\begin{aligned} &[W_p, W_{p'}] = 0 \quad \text{for all } p \text{ and } p', \\ &[H, W_p] = 0 \quad \text{for all } p. \end{aligned} \tag{6.4}$$

The plaquette operators share a set of joint eigenstates and the set of eigenvalues $\{w_p\}$ separates the Hilbert space of the model into individual sectors.

On a sufficiently large honeycomb lattice with N spins, there are $N/2$ plaquettes. The 2^N-dimensional Hilbert space thus decomposed into $2^{N/2}$ sectors associated to the eigenvalues and each sector has a dimension of $2^{N/2}$. In other words, each plaquette has one degree of freedom which is not captured by W_p. Since W_p are conserved quantities, the Hamiltonian does not mix these sectors, and the physics of the model can be studied on each sector individually. This greatly simplifies the analysis of the model and in particular, due to a theorem by Lieb [158], we know that the ground state of the model resides in the no-vortex sector, i.e. $w_p = +1$ for all p.

In the original treatment by Kitaev [118, 155], each spin is represented by two fermionic modes, which introduce artificial (non-physical) degrees of freedom in the model. The fermionic modes are then further decomposed into four Majorana particles, in terms of which the problem can be solved analytically. There is however a simpler and more accessible approach outlined by Chen and Nussinov [159], in which they first map the Hamiltonian to a fermionic model via the Jordan-Wigner transformation [91]. The fermionic model is then written in terms of Majorana particles and subsequently recast to the following Hamiltonian by re-grouping Majoranas and defining a new fermionic mode,

$$H = \sum \left[\epsilon_q d_q^\dagger d_q + i\frac{\Delta_q}{2}\left(d_q^\dagger d_{-q}^\dagger + \text{H.c.}\right)\right], \tag{6.5}$$

where,

$$\begin{aligned} \epsilon_q &= 2J_z - 2J_x \cos q_x - 2J_y \cos q_y, \\ \Delta_q &= 2J_x \sin q_x + 2J_y \sin q_y. \end{aligned} \tag{6.6}$$

Eq. (6.5) describes the Hamiltonian of a p-wave Fermi superfluid with site-dependent chemical potential. It is known that by Bogliubov transformation the Hamiltonian can be diagonalized to derive the dispersion relation,

$$E_q = \sqrt{\epsilon_q^2 + \Delta_q^2}. \tag{6.7}$$

This relation exhibits gapped and gapless phases. The border of the two phases is defined by $E_q = 0$ and this leads to following conditions on the interaction strengths for the gapless phase,

$$\begin{aligned} |J_{xx}| &\le |J_{yy}| + |J_{zz}|, \\ |J_{yy}| &\le |J_{xx}| + |J_{zz}|, \\ |J_{zz}| &\le |J_{xx}| + |J_{yy}|. \end{aligned} \tag{6.8}$$

The gapped phase is then realized if the magnitude of any of the $J_\alpha (\alpha = xx, yy, zz)$ is larger than the sum of the other two. This regime is called the phase A of the model. In this phase, it is possible to make an exact mapping between the zero-fermion sector of the honeycomb model and the toric code [155]. Hence, in analogy to the toric code, the same abelian anyonic excitations are expected to exist in the honeycomb model in the gapped phase as well.

To explore these excitations, let us consider an operator σ_a^z acting on a spin a in the ground state of the model as shown in Fig. 6.2. This spin is shared by three plaquettes. While the spin operator commutes with the plaquette operator W_p of one of the neighboring cells (p_4 in the figure), it anti-commutes with the other two (p_1 and p_2). As a result, the eigenvalue of W_p for those two plaquettes become -1, which is associated to the existence of vortices or anyons on them. Likewise σ_a^x creates vortices on p_2 and p_4 and σ_a^y generates two vortices on p_1 and p_4. A vortex on a plaquette can be annihilated by creating a second vortex on that plaquette. For example, starting from the ground state, if one first acts with σ_a^x and then with σ_b^y on two adjacent spins a and b as shown in Fig. 6.2, two vortices are first created on p_2 and p_4 due to σ_a^x, while the σ^y operator produces vortices on p_2 and p_3. Therefore the result of the composite operator $\sigma_a^x \sigma_b^y$ is to generate excitations on p_1 and p_4. In this way, by combining spin operators one could move the vortices around the lattice.

The gapless phase of the model is realized when the conditions (6.8) are met. Based on an analogy with $p + ip$ superfluids, Kitaev argues that the excitations in this phase are *non-abelian anyons.* As opposed to abelian anyons of the gapped phase, non-abelian anyons are useful for topological quantum computation. However, for this purpose one needs to open a gap in this regime,

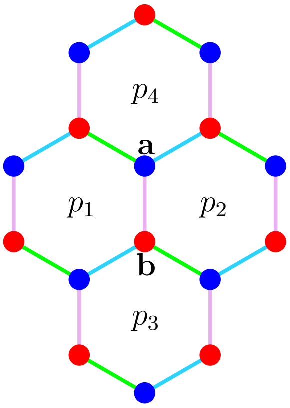

Figure 6.2: A piece of honeycomb lattice with four cells. By applying σ^z to spin a, two vortices are created on p_1 and p_2. Applying σ^x to spin a and to spin b, creates two vortices on cells p_3 and p_4.

which is feasible through the application of a magnetic field.

We now turn to the discussion of the implementations of the model in superconducting circuits [160]. In our implementations, transmon qubits form the spin degrees of freedom and we use two driven schemes to realize the couplings as discussed in Chap. 5.

6.2 Implementation based on driven qubits

In an implementation based on driven qubit scheme, the xx and yy couplings are realized through fixed capacitive couplings as discussed in Sec. 5.3.2. The zz coupling is realized using an undriven dc-SQUID which can be tuned via the dc flux through it to adjust the coupling strength, see Sec. 5.4.1 and Fig. 6.3. As we discussed in Chap. 5, the xx and yy couplings are second-order while the zz coupling is fourth-order in the interaction strength. Therefore to ensure that the first-order couplings [1] are ineffective, we assume that each of the two nearest neighbors are detuned by several GHz with respect to each other [2]. This large detuning is shown by two different colors (red and blue)

---

[1] Remember that to the first order the capacitive coupling has the form $\sigma^y\sigma^y$ and the SQUID coupling is of the inductive form $\sigma^x\sigma^x$.

[2] Note that in Chap. 5, we made the same assumption that the two-qubits are detuned with respect to each other.

for the qubits in Figs. 6.1 and 6.3. Furthermore, to suppress next-nearest interactions, we still need to slightly detune next-nearest neighbor qubits (two red or blue qubits which share a common neighbor).

In this scheme, a typical qubit i of the lattice is modulated via a longitudinal drive $W_i(t)\sigma_i^z$. To define the form of $W_i(t)$, let us first consider two neighboring qubits i and j building a xx or yy link. Based on the discussion in Sec. 5.3.2, to engineer these interactions *both frequencies* $\omega_i \pm \omega_j$ are needed. For two coupled qubits, a xx or yy interaction can be obtained by driving one qubit at the sum and the other at the difference of the two transition frequencies. For example, we choose,

$$W_i = b_{ij} \cos\big[(\omega_i + \omega_j)t\big], \quad W_j = b_{ji} \cos\big[(\omega_i - \omega_j)t\big], \tag{6.9}$$

where b_{ij} is the amplitude of the drive applied to qubit i to engineer the interaction with qubit j and b_{ji} is the amplitude of the drive applied to qubit j to engineer the interaction with qubit i. We also discussed in Sec. 5.3.2 that in order to implement a *pure xx* interaction the amplitudes should meet the following relation,

$$\frac{b_{ji}}{\omega_i - \omega_j} = \frac{b_{ij}}{\omega_i + \omega_j}. \tag{6.10}$$

On the other hand, for a pure yy coupling it is needed that,

$$\frac{b_{ji}}{\omega_i - \omega_j} = -\frac{b_{ij}}{\omega_i + \omega_j}. \tag{6.11}$$

Since in the honeycomb model each qubit should build both xx and yy interactions with two neighbors (e.g. j and j', see Fig. 6.3a) and we assume that the neighbors have different transition frequencies, four different modulation frequencies are required to generate both interactions. These frequency components explicitly read,

$$\omega_i + \omega_j, \quad \omega_i - \omega_j, \quad \omega_i + \omega_{j'}, \quad \omega_i - \omega_{j'}. \tag{6.12}$$

To reduce the number of frequency components applied to a qubit, we can generalize the form (6.9) to two neighbors [3] and propose the following simplified form of the drive applied to a qubit i, see Fig. 6.3a,

$$W_i = b_{ij}\cos\big[(\omega_i+\omega_j)t\big] + b_{ij'}\cos\big[(\omega_i-\omega_{j'})t\big]. \tag{6.13}$$

Here the first component of the drive at qubit i is responsible to generate an interaction with qubit j and the second component builds an interaction with qubit j'. Due to the assumed detunings between next-nearest neighbors j and j', the first (second) component does not affect the interaction between i and j' (j). Note that the proposed drive (6.13) is not symmetric with respect to the neighbors of the qubit i, so we should define the positions of j and j'. As the xx and yy links that connect qubits on a honeycomb lattice form a zigzag line, we can identify j and j' by left and right neighbors of qubit i. Here we choose qubit j (j') to be to the right (left) of qubit i. This convention means that since $j(j')$ is to the right (left) of the qubit i, this qubit is modulated by $\omega_i+\omega_j(\omega_i-\omega_{j'})$. One could equally choose the opposite convention, but it is important to stick to a same convention when applying the drive (6.13) to qubits. For example, in Fig. 6.3a the qubit i is the left of qubit j, so the drive W_j applied to qubit j has a component proportional to cos $\big[(\omega_j-\omega_i)t\big]$, see Eq. (6.13). On the other hand, the qubit i is to the right of j', therefore according to the convention, the applied drive $W_{j'}$ to qubit j' should have a component cos $\big[(\omega_{j'}-\omega_i)t\big]$. In this way, we make sure that each pair of qubits are driven by both the difference and sum of their transition frequencies to implement a xx or yy interaction, c.f. Eq. (6.9).

We now consider a four-qubit module of the honeycomb lattice which consists of a transmon qubit and its three nearest neighbors as shown in Fig. 6.3b. Through numerical simulations we verify that (1) the proposed drive will indeed generate the required interactions in the honeycomb lattice and (2) this local drive does not have long-range effects i.e. locally engineered interactions work to a good-approximation in a many body system. For this four-qubit

---

[3] A qubit has three neighbors but the third neighbor is on a zz link without modulation. Here we are just concerned about xx and yy links.

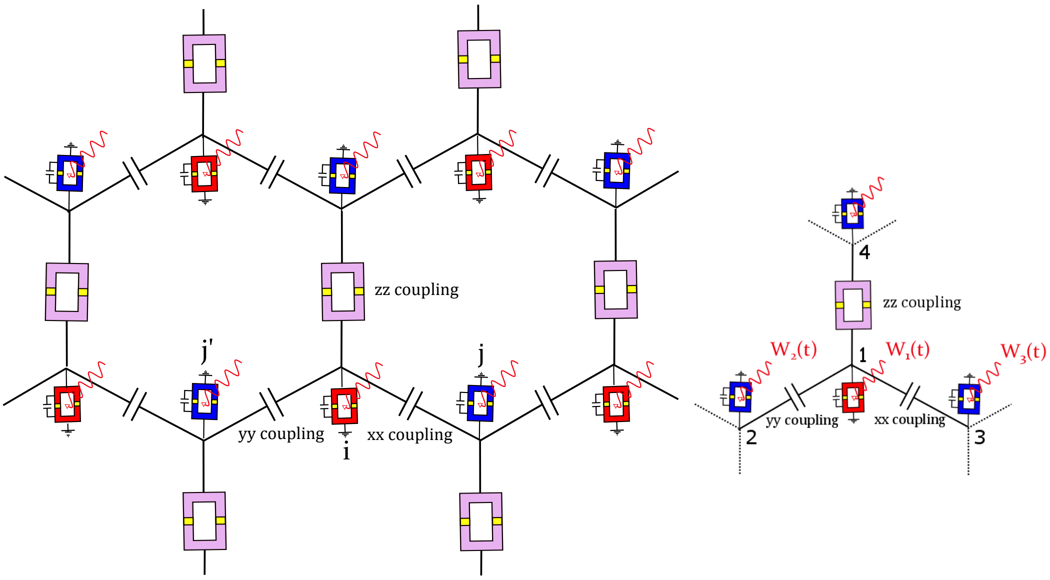

(a) **(b)**

Figure 6.3: (a) Implementation of a honeycomb cell in quantum simulation of the Kitaev model on a honeycomb lattice using driven qubit scheme. Each qubit (e.g. i) is modulated by two frequency components: $\omega_i + \omega_j$ where j is the right neighbor and $\omega_i - \omega_{j'}$ where j' is the left neighbor, see Eq. (6.13). (b) A typical qubit and three adjacent neighbors used for numerical simulations.

module, we consider the following drives,

$$\begin{aligned} W_1(t) &= b_{12}\cos(\omega_1 - \omega_2) + b_{13}\cos(\omega_1 + \omega_3), \\ W_2(t) &= b_{21}\cos(\omega_1 + \omega_2), \\ W_3(t) &= b_{31}\cos(\omega_1 - \omega_3). \end{aligned} \tag{6.14}$$

Note that we have neglected the modulating function $W_4(t)$ (with two components) which is applied to qubit 4, and the second components of $W_2(t)$ and $W_3(t)$, c.f. Eq. (6.13) [4]. These fields are relevant for the other two neighbors of qubits 2, 3 and 4 which are not shared by them. We assume that these components are off-resonant with respect to the interaction within the considered module and hence ignore them. This is a valid assumption, since the next-nearest neighbors are detuned with respect to each other, which makes

---

[4] Including these modes will substantially increase the dimension of the Floquet Hamiltonian in the extended space.

sure that the off-resonant components do not cause a large deviation from the expected behaviour. Nevertheless, a crude estimation of their effect could be made by noting that the second frequency component of $W_1(t)$ (i.e. $\omega_1 + \omega_3$) is off-resonant for the xx-link or zz-link interactions. In other words, the off-resonant component is irrelevant for the implementation of those couplings. Likewise the first component of $W_1(t)$ is off-resonant with the interaction between qubit 1 and 3 or 4 (yy and zz-links). The effect of the off-resonant fields can easily be calculated in our simulation by turning them on and off. We therefore expect that the effect of the components that we didn't include in Eq. (6.14) should be comparable to the effect of off-resonant component of $W_1(t)$ on the xx coupling, etc.

Furthermore, the relations (6.10) and (6.11) require that the amplitudes of the oscillating fields $W_i(t)$ in Eq. (6.14) should satisfy,

$$\frac{b_{12}}{\omega_1 - \omega_2} = \frac{b_{21}}{\omega_1 + \omega_2}, \quad \frac{b_{13}}{\omega_1 + \omega_3} = -\frac{b_{31}}{\omega_1 - \omega_3}. \tag{6.15}$$

As an example, for the parameters of the module we choose $\omega_1/(2\pi) = 6.1$ GHz, $\omega_2/(2\pi) = 9.6$ GHz, $\omega_3/(2\pi) = 9.1$ GHz and $\omega_4/(2\pi) = 9.9$ GHz for the transition frequencies of the four qubits, $g_c = 200$ MHz for the capacitive couplings, $g_x = -200$ MHz and $g_z = -10$ MHz for the zz coupling of the SQUID. For the coefficients b_{ij} in Eq. (6.14), we assume $b_{12} = 213.3$ MHz, $b_{21} = -48$ MHz, $b_{13} = -41.7$ MHz and $b_{31} = 204.1$ MHz. The Floquet matrix of this minimal circuit has four individual frequency modes with four qubit degrees of freedom. For numerical calculations with the Floquet matrix and the derivation of an effective Hamiltonian, we truncate the infinite space of the drive to 9 photonic states ($n = -4$ to $n = 4$). The effective Hamiltonian of this system takes the form,

$$H_{eff} = \sum_{j=1}^{4} \delta\omega_j \sigma_j^z + J_{xx}\sigma_1^x\sigma_3^x + J_{yy}\sigma_1^y\sigma_2^y + J_{zz}\sigma_1^z\sigma_4^z, \tag{6.16}$$

with coupling strengths $J_{xx} = 5.21$ MHz, $J_{yy} = -5.20$ MHz, $J_{zz} = -9.9$ MHz and frequency shifts $\delta\omega_1 = -13.41$ MHz, $\delta\omega_2 = 6.77$ MHz, $\delta\omega_3 = 7.38$ MHz

	Parameters (MHz)			
Coupling	$\delta\omega_1$	J_{xx}	J_{yy}	J_{zz}
All on	-13.41	5.21	-5.20	-9.9
Qubit 1 and 2	-4.41	5.44	0	0
Qubit 1 and 3	-5.10	0	-5.34	0
Qubit 1 and 4	-4.00	0	0	-10

Table 6.1: The coefficients of effective Hamiltonian for driving amplitudes $b_{12} = 213.3$MHz, $b_{21} = -48$MHz, $b_{13} = -41.7$MHz and $b_{31} = 204.1$MHz. In second through the fourth row just one of the couplings turned on. The parameters of the undriven Hamiltonian are $g_c = -g_x = 200$MHz and $g_z = -10$MHz.

and $\delta\omega_4 = -6.96$ MHz. Tab. 6.1 shows the effective interaction parameters and frequency shift for qubit 1 for this case. In the table, we have also shown the relevant interaction strengths and frequency shifts when just one of the couplings is turned on and the two others are turned off. The aggregate contributions of the individual two-body couplings deviate from the parameters calculated for the four-body module by 1% $\sim$ 1MHz in the frequency shift and by almost 4% in the coupling strengths.

In Fig. 6.4, the lowest 100 quasienergies of the fast space of the four-body Floquet matrix and their maximum coupling element (in the scattering matrix $\mathcal{T}$, i.e. t_{max}) to the dynamical (slow) space are shown for two cases that result in almost the same effective couplings: one with weaker couplings in the undriven lattice and stronger drive and a second in the opposite limit. For both cases a gap of 300MHz exist between the slow space at zero energy and high energy states and the ratio t_{max}/ϵ is ~ 0.05 which validates the adiabatic elimination and the effective Hamiltonian H_{eff}.

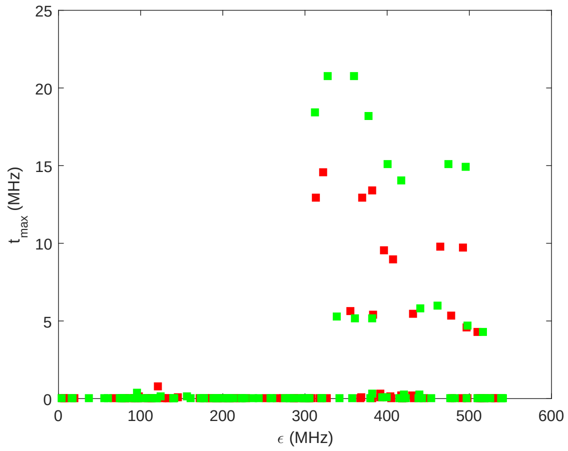

Figure 6.4: Validity of adiabatic elimination in an implementation based on the driven qubit schemes. The maximum coupling element t_{max} between the slow space and the lowest states of the fast space of the driven four-body circuit is shown as a function of quasienergies ϵ (of the fast space). Red (green) squares show the data for weaker (stronger) couplings in the lattice with stronger (weaker) modulation. Both cases have the same effective couplings (~ 5.2 MHz for $|J_{xx}|$ and $|J_{yy}|$ and $\sim$ 10 MHz for $|J_{zz}|$) and an effective gap of $\sim$ 300 MHz. Parameters $b_{12} = 213.3(177.7)$ MHz, $b_{21} = -48(-40)$ MHz, $b_{13} = -41.7(-34)$ MHz and $b_{31} = 204.1(166.2)$ MHz for data shown in red (green). The parameters of the undriven Hamiltonian are $g_c = -g_x = 200(250)$ MHz and $g_z = -10$ MHz.

6.3 Implementation based on driven couplings

In the driven coupling scheme the xx and yy links are implemented by driven SQUIDs (c.f. Sec. 5.4) and the zz link is implemented by an undriven SQUID, see Fig. 6.5. The oscillating flux through the coupler SQUID between two qubits i and j which form a xx or yy link is defined as,

$$\phi_{ij}(t) = \pi + 2\phi_{ij,1}\cos\left((\omega_i - \omega_j)t + \theta_{ij}\right) + 2\phi_{ij,2}\cos\left((\omega_i + \omega_j)t\right), \tag{6.17}$$

where $\theta_{ij} = 0(\pi)$ for a $xx(yy)$ link. Note that in contrast to the driven qubit scheme, the qubits are not driven directly. Let us first comment on the transition frequency pattern of the qubits in this scheme. Note that as opposed to the driven qubit scheme, here the xx and yy interactions are first order in the coupling strength, which gives us more freedom to choose the frequency pattern. It is possible to choose the same transition frequency pattern as for the driven qubit scheme where each qubit is largely detuned with respect to its neighbors. Alternatively, the transition frequencies of the qubits lying on a zigzag line which is formed by xx and yy links can be chosen to be closer to each other. The qubits on the zz links are still required to be sufficiently detuned, as the zz interaction is fourth-order and there is a strong first-order xx coupling associated with this coupler. We therefore explore two regimes of qubit transition frequencies of a four-body circuit shown in Fig. 6.5b:

1. Large detuning regime. Here we choose the same transition frequencies as in the driven qubit example: $\omega_1/(2\pi) = 6.1$ GHz, $\omega_2/(2\pi) = 9.6$ GHz, $\omega_3/(2\pi) = 9.1$ GHz and $\omega_4/(2\pi) = 9.9$ GHz.

2. Small detuning regime. We choose the following values for the transition frequencies: $\omega_1/(2\pi) = 6.1$ GHz, $\omega_2/(2\pi) = 6.45$ GHz and $\omega_3/(2\pi) = 6.55$ GHz and $\omega_4/(2\pi) = 9.9$ GHz.

For both regimes, we use the same coupling parameters. For the xx and yy couplings, the parameters of the coupling SQUIDs read,

$$g_x = -300\text{MHz}, \quad g_z = -10\text{MHz}, \quad g_i = g_j = 150\text{MHz}, \quad \phi_{ij,1} = \phi_{ij,2} = 0.1. \tag{6.18}$$

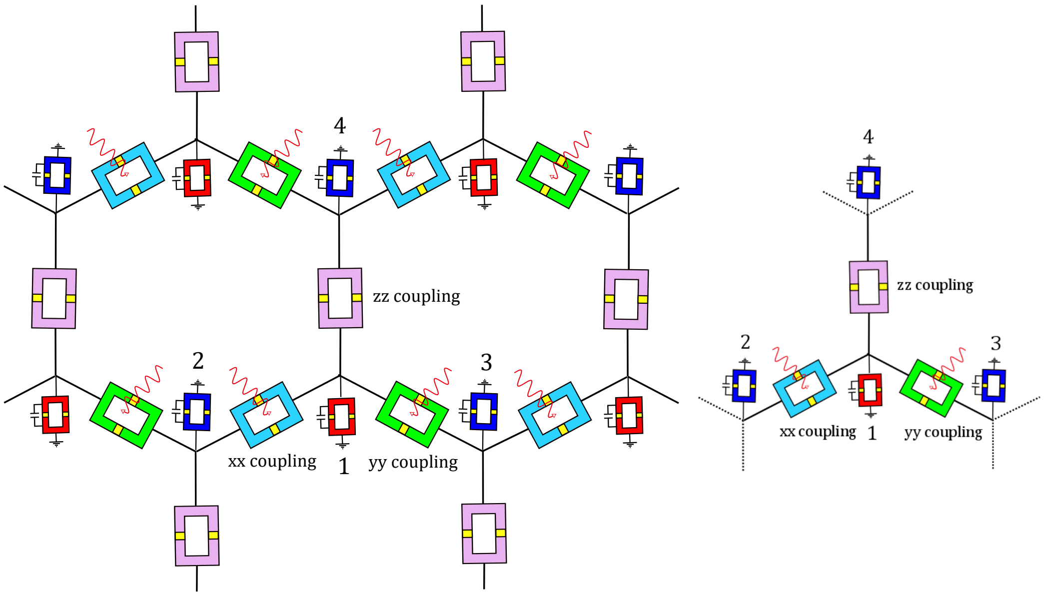

(a) (b)

Figure 6.5: (a) Implementation of the Kitaev model on a honeycomb lattice in superconducting circuits based on driven coupling scheme (b) A typical qubit and three nearest neighbors considered for numerical simulations.

For zz links the parameters read,

$$g_x = -200\text{MHz}, \quad g_z = -10\text{MHz}. \tag{6.19}$$

Through numerical simulation to perform adiabatic elimination using Salwen method, we can verify that the effective Hamiltonian takes the same form as Eq. (6.16). In the large detuning regime, we get the parameters $J_{xx} = J_{yy} = 30$ MHz and $J_{zz} = 10$ MHz in agreement with the RWA. For the opposite regime of small detunings, the couplings read $J_{xx} = 29.78$ MHz, $J_{yy} = 29.80$ MHz, $J_{zz} = -9.8$ MHz and $\delta\omega_1 = -14.85$ MHz. To validate the adiabatic elimination, we have also calculated the maximum coupling strength between the states that give rise to the effective Hamiltonian (i.e. the degenerate manifold at zero energy) and the states with lowest energies in the fast space. The result is shown in Fig. 6.6 and shows that there is an effective gap ~ 400MHz between the two fast and slow subspaces, while the coupling reaches a maximum of $\sim$ 40MHz. Therefore the derived Floquet Hamiltonian should be

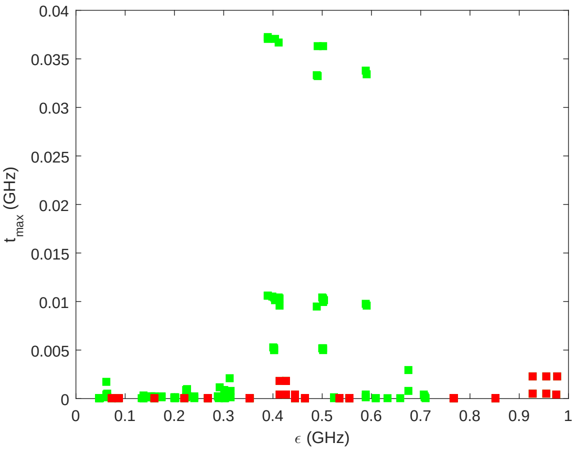

Figure 6.6: Validity of adiabatic elimination in an implementation based on driven couplings. The maximum coupling element t_{max} between the slow space and the lowest states of the fast space of the driven four-body circuit is shown as a function of quasienergies ϵ (of the fast space). Red (green) squares show the data for small (large) detuning regime of qubit transition frequencies. Both cases have an effective coupling of $\sim$ 30 MHz and an effective gap of $\sim$ 400 MHz. For the large detuning regime the couplings are well approximated by RWA. Parameters: $\omega_1/(2\pi) = 6.1$ GHz, $\omega_2/(2\pi) = 6.45$ GHz and $\omega_3/(2\pi) = 6.55$ GHz and $\omega_4/(2\pi) = 9.9$ GHz for green data and $\omega_1/(2\pi) = 6.1$ GHz, $\omega_2/(2\pi) = 9.6$ GHz, $\omega_3/(2\pi) = 9.1$ GHz and $\omega_4/(2\pi) = 9.9$ GHz for red data.

well-approximated by the derived effective Hamiltonian.

6.4 Discussion and outlook

In this section, we make an overview of the results and give an outlook towards further advances.

We discussed that, in an implementation of the honeycomb model based on qubit driven schemes, each qubit is driven by a bimodal drive. This drive is designed such that one of the components contributes to build up an xx interaction with one neighbor, while the second component contributes to generate a yy interaction with another neighbor. Based on our discussion in Chap. 5, an implementation of a xx or yy interaction requires modulations by both the sum and the difference of the transition frequencies. Our modulation scheme here is based on the fact that it is possible to modulate each of the qubits forming xx or yy interaction by one of these frequencies. In this scheme, these interactions are constructed through second-order processes and the interaction strengths in our numerical example reach $|J_{xx}| \sim |J_{yy}| \sim 5$MHz. For the zz interaction which is implemented by an undriven SQUID, the interaction strength is $|J_{zz}| \sim 10$MHz. In the driven coupling scheme, xx and yy couplings are implemented by SQUIDs which couple the qubits and are driven by bimodal external fluxes at the sum and difference of the transition frequencies of the corresponding qubits. The zz coupling is realized in the same way as in driven qubit schemes. Here xx and yy are first-order in the modulation strengths and we can reach $|J_{xx}| \sim |J_{yy}| \sim 30$MHz.

It is important to note that in both schemes J_{xx}, J_{yy} and J_{zz} can be tuned independently. The first two are tuned via the modulation amplitudes and the latter is modified by the dc flux of the coupling SQUID. Thus, in principle it is feasible to explore both phases of the honeycomb model. We discussed in Sec. 6.1 that the abelian phase is realized when $|J_\alpha| > |J_\beta| + |J_\gamma|$, $\alpha, \beta, \gamma \in \{xx, yy, zz\}$. In this phase the model can be mapped onto the toric code model. Let us consider $|J_{zz}| \gg |J_{xx}|, |J_{yy}|$ and $J_{zz} > 0$. In this regime, it is energetically favourable for two spins that form a z-link to be aligned. Therefore there are two spin configurations that participate in the low energy sector of the model which can be described by one effective spin,

$$|\uparrow\uparrow\rangle \rightarrow |\Uparrow\rangle\,, \quad |\downarrow\downarrow\rangle \rightarrow |\Downarrow\rangle\,. \tag{6.20}$$

In terms of these effective spins z-links can be replaced by spins and the honeycomb lattice turns to a square lattice which hosts the toric code. We would then anticipate that our adiabatic approach for ground state preparation in the toric code can be applied to the honeycomb model as well. The preparation of the ground state in the honeycomb model can be verified by measuring plaquette operators W_p defined in Eq. (6.2). The outcome of the measurement should be +1 for all honeycomb cells. Note that the toric code is a perturbative limit of the honeycomb model, namely it appears in the fourth-order of a perturbative expansion. In reference [161], different lattice sizes for the honeycomb model are considered. Although even a small lattice Hamiltonian as well. Kells *et al.*[161] finds that the smallest finite-size lattice to produce the toric code without lower order terms has 36 spins. In the abelian phase, one can also manipulate vortices as described in Sec. 6.1 or perform quantum error correction [179].

Using our proposed circuits, one can also investigate the non-abelian phase of the model. Compared to the abelian phase, the topological properties of this gapless phase is less explored [162]. Kitaev shows that applying a magnetic field of the form,

$$H_B = \sum_j h_x \sigma_j^x + h_y \sigma_j^y + h_z \sigma_j^z, \tag{6.21}$$

opens a gap in this phase. In our implementations, it should be achievable to implement this Hamiltonian by incorporating resonant modulations of the qubits, in addition to the modulation forms we discussed throughout this chapter to realize the couplings.

6.5 Summary

In this chapter, we introduced the Kitaev's honeycomb lattice model and discussed two implementations of this model. Our implementations are based on the engineered spin-spin interactions considered in Chap. 5. In the first implementation, we relied on driven qubit schemes while in the second proposal, we used driven couplings. For both architectures, we numerically calculated the low-energy effective Hamiltonian of a four-body segment of the lattice and showed that the low-energy physics should be described by the honeycomb model.

Chapter 7

Conclusions and future directions

In this thesis, we explored a number of possibilities of employing engineered single and multi-mode microwave driving in analog quantum simulation of few and many body quantum systems with superconducting circuits. To lay the foundations of the discussions in the later chapter, we first presented an introduction to superconducting quantum circuits and quantum simulation in **chapters 2** and **3**. In **chapter 2**, we discussed the physics of superconducting circuits, their applicability as qubits for quantum information processing and the Hamiltonian description of such systems. In **chapter 3**, we described analog and digital quantum simulation and gave a brief review of recent theoretical and experimental advances in the field of quantum simulation with superconducting circuits. The results we demonstrated in the subsequent chapters can be summarized as follows,

1. An analog quantum simulation of the Kitaev toric code and honeycomb lattice models, discussed in chapter 4.
2. A toolbox for generating arbitrary spin-spin interactions in coupled transmon circuits with linear and nonlinear couplings, which was the subject of chapter 5.

In **chapter 4**, we introduced a transmon-based superconducting circuit for an analog quantum simulation of the toric code. This model is defined on a two-dimensional lattice with four-body star and plaquette interactions and features topological order. To directly generate these interactions, the main idea we applied here was to introduce a *driven ancilla* degree of freedom which mediates interactions between four qubits that form a star or plaquette term, but yet it remains in its ground state. This dynamical ancilla is implemented in our architecture by a dc-SQUID, which is threaded by a suitable external oscillating flux which consists of eight frequency components. We showed that the toric code Hamiltonian is the effective Hamiltonian of the lattice in the rotating frame of the qubits. Since the model is realized in a rotating frame, the topologically-ordered ground state manifold of the model is not prepared in the cryogenic enviroment of the circuit. For this reason, we proposed an adiabatic approach for the ground state preparation. We examined a minimal eight-qubit model, which is accessible for state-of-the-art superconducting circuit technology. In particular, superconducting circuits allow for realizing periodic boundary conditions, a feature that is not easily available in other platforms but crucial for exploring topological order. We thus expect our work to open up a realistic path towards an experimental investigation of this intriguing area of quantum many-body physics. Our scheme is highly versatile and not restricted to implementations of the toric code only. Several directions for generalizations appear very intriguing at this stage:

Toric code with perturbations In our proposal, the goal was to deliver a *neat* realization of the toric code Hamiltonian. Nonetheless, it is pretty straight-forward in our designed circuit to add several types of perturbations to the toric code Hamiltonian. For example by tuning the time-independent flux bias of the coupling SQUIDs away from the operating point for the toric code, one can generate additional two-body interactions of the form $\sigma^z\sigma^z$ between neighboring qubits. It should then be possible to study the topological properties in the presence of several perturbations or local defects.

$\mathbb{Z}_2$ topological order at finite temperatures It is known that the degenerate ground state manifold of the toric code is not protected at finite temperatures [163, 164]. This effect is related to the generation and propagation of anyons due to dissipative processes. This fact can also be confirmed by noting that the fidelity of our adiabatic preparation reduces to low values for long preparation times. Therefore a future direction to investigate would be to extend our proposal to finite temperatures [168, 169] and to stabilize the topological protection at finite temperatures [166, 167].

Quantum simulation of LGT Quantum simulation of Lattice Gauge Theories (LGT) have been the subject of intensive studies in recent years, namely in the ultracold atoms [170, 171], trapped ions [172, 173] and superconducting circuits [101, 102] communities. The toric code itself is an example of a $\mathbb{Z}_2$ LGT, which is a certain limit of $U(1)$ LGT (lattice QED) in the absence of fermions. The multi-body interactions that lie at the heart of our analog simulator, indeed appear in almost all LGTs. Our approach to generate four-body interactions is then useful for quantum simulation of other LGTs. For example, one-dimensional $U(1)$ lattice QED comprises three-body interactions. It should in principle be easier to implement than the toric code! A two-dimensional $U(1)$ lattice QED (with fermions) poses more challenges, since in addition to the spin degrees of freedom present in the toric code (gauge bosons), one should include additional degrees of freedom at the vertices of the lattice representing the fermionic field in quantum electrodynamics. The ultimate goal of quantum simulators is of course the celebrated QCD (quantum chromodynamics) [174].

Quantum anealing The quest for multi-body interactions is not only motivated by the quantum simulation of condensed matter and many-body models like LGTs or topological models of the toric code family (e.g. Wen models), but it proves vital for quantum information applications like *quantum annealing.* In a proposal by Lechner *et al* [175] the non-local Hamiltonian of the quantum annealing problem is mapped to a local Hamiltonian at the cost of additional four-body constraints. For an implementation in superconducting circuits, an easy way to generate these constraints would then be appealing [176, 177].

In **chapter 5**, we presented our results for engineering single-mode and bimodal driven superconducting circuits to generate arbitrary spin-spin interactions using the framework of Floquet theory. Here the aim was to propose a unified theory and toolbox that could be easily generalized to a variety of systems and driving schemes. For this purpose, we found the time-independent formalism of the Floquet theory an expedient setting to build desired effective interactions. Specifically, in our Floquet engineering approach, we work in the resonant regime which is generally more difficult to handle in the time domain. Floquet engineering typically relies on a perturbation theory in the parameter "drive amplitude/detuning", which leads to divergences in resonant cases. Therefore one needs to remove resonance terms (e.g. by moving to a rotating frame) before applying the perturbation theory in the time-domain. In contrast, the resonantly coupled states constitute a low energy manifold in our Floquet engineering approach. This manifold is the basis for an effective Hamiltonian, which we derived using of the Salwen's perturbation theory [152]. Compared to Van Vlack theory which requires finding an operator that block-diagonalizes the Hamiltonian, our approach based on Salwen theory depends on energies that can be determined in a self-consistent manner and therefore it is easier to go to higher orders of the perturbation. While time-dependent treatments could lead to more compact forms of an effective Hamiltonian than approaches in the composite space like ours, the latter prove more apt for numerical approaches to Floquet engineering. In our work, we applied this toolbox to two types of systems: linearly coupled transmon qubits with the drives applied to the qubits and nonlinearly coupled qubits with driven coupling. Our schemes can also be applied to superconducting architectures with other types of qubits. In particular, the following generalizations could lead to advances in the field of quantum simulation with superconducting circuits,

Floquet engineering of three-body interactions Our setup can be generalized in the first place to three spin interactions. For example we envisage that coupling three transmon capacitively and driving one of the qubits at a frequency that equals the sum of all transition frequencies, leads to a three-qubit squeezing interaction. The three-body interactions are interesting for a number of condensed matter models [178]. More generally, a three-body interaction can provide a base for an *analog-digital quantum simulation*, where in addition to one and two-body terms, one is also armed with bigger blocks with three-body terms to start a digital quantum simulation with.

Floquet engineering of Liouvillians A second direction to investigate is Floquet engineering in periodically driven-dissipative systems based on our approach. In a periodically driven superconducting circuit, one can incorporate a *fast-decaying* ancilla through a coupling to a strongly dissipative channel. The Liouvillian superoperator of such a system can then be represented in a composite extended space $\mathscr{L}_c = \mathscr{H} \otimes \mathscr{H} \otimes \mathscr{T}$, where as usual $\mathscr{H}$ is the Hilbert space of the system and $\mathscr{T}$ is the Fourier space of periodic functions. An effective Liouvillian can be defined in the slow decaying and low energy subspace. It should be possible to engineer the jump operators of the effective Liouvillian through designing appropriate driving protocols.

Based on the results of chapter 5, we introduced two architectures for analog quantum simulator of the Kitaev honeycomb model in **chapter 6**, namely an architecture based on driven qubit schemes and a second architecture based on driven coupling schemes. This work can be pushed forward by considering an adiabatic approach for preparation of the vortex-free ground state of the model. As opposed to the toric code, the honeycomb model is a frustrated spin model, and as a result ground state preparation via an adiabatic sweep from a reference state can be more involved than for the toric code. Implementation of quantum error correction in this model [179] can be the subject of another research project in this direction.

In conclusion, our work has shown the great potential of engineered microwave driving in quantum simulation and quantum information and we hope that this opens up new avenues with this regard.

Appendix A

Expressions for Schrieffer-Wolff transformation

For the Hamiltonian (4.20) and generator (4.23), Schrieffer-Wolff transformation gives the followings expressions up to the fourth order,

$$\begin{aligned}[S,\mathcal{H}] = &\sum_j E_L(\phi_{q+;j}\phi_{+;j} + \phi_{q-;j}\phi_{-;j}) \\ &- 4\sum_j E_{Cq;j}\pi_j(\pi_{S+;j} + \pi_{S-;j}) \\ &- \sum_j \frac{E_L}{2}\sum(\phi_{q+;j} + \phi_{q-;j})^2 \\ &+ \sum_j E_J \cos(\phi_{ext;j}/2)\sin(\phi_{-;j})\phi_{q-;j},\end{aligned} \tag{A.1}$$

$$\begin{aligned}[S,[S,\mathcal{H}]] = &\sum_j \frac{E_L}{2}\sum(\phi_{q+;j} + \phi_{q-;j})^2 \\ &+ 2E_{Cq;j}(\pi_{S+;j} + \pi_{S-;j})^2 \\ &+ \sum_j \frac{E_J}{2}\cos(\phi_{ext;j}/2)\cos(\phi_{-;j})\phi^2_{q-;j},\end{aligned} \tag{A.2}$$

$$[S,[S,[S,\mathcal{H}]]] = \sum_j \frac{E_J}{4}\cos(\phi_{ext;j}/2)\sin(\phi_{-;j})\phi^3_{q-;j}, \tag{A.3}$$

$$[S,[S,[S,[S,\mathcal{H}]]]] = -\sum_j \frac{E_J}{8}\cos(\phi_{ext;j}/2)\cos(\phi_{-;j})\phi_{q-;j}^4, \tag{A.4}$$

with,

$$\pi_{S\pm;j} \equiv \pi_{S\pm;m,n} = \pi_{\pm;n,m} \pm \pi_{\pm;n-1,m} + \pi_{\pm;n,m-1} \pm \pi_{\pm;n-1,m-1}. \tag{A.5}$$

Appendix B

Projection-operator approach to Salwen perturbation theory

We here present a generalized approach to Salwen perturbation theory [152]. For an unperturbed Hamiltonian H_0 on Hilbert space $\mathscr{H}$ with eigenstates and eigenenergies $|\alpha\rangle$ and $\epsilon_\alpha^{(0)}$, we assume that $\mathscr{H} = \mathcal{S} \oplus \mathcal{F}$ in which $\mathcal{S}$ is a the subspace of nearly degenerate eigenstates of H_0 such that $|\alpha\rangle \in \mathcal{S}$ is separated in energy from all other states $|\beta\rangle \in \mathcal{F}$ with an energy gap, i.e.

$$|\epsilon_\alpha - \epsilon_\gamma| \ll |\epsilon_\beta - \epsilon_\gamma|, \tag{B.1}$$

for any $|\gamma\rangle \in \mathcal{S}$. We now consider a perturbation V to the Hamiltonian H_0 and write the Schrödinger equation for the perturbed Hamiltonian $H = H_0 + V$ as,

$$H\,|u_\alpha\rangle = \epsilon_\alpha\,|u_\alpha\rangle\,, \quad |\alpha\rangle \in \mathscr{H}, \tag{B.2}$$

in which $|u_\alpha\rangle$ is the eigenstate corresponding to $|\alpha\rangle$ with energy ϵ_α. The goal is to find an effective Hamiltonian H_{eff} defined on $\mathcal{S}$ which has the same eigenenergies ϵ_α as H. To derive this effective description perturbatively, we assume that the energy gap is larger than any coupling element $\langle\alpha|V|\beta\rangle$ for $|\alpha\rangle\,, |\beta\rangle \in \mathscr{H}$. This means that the states in $\mathcal{S}$ maintain large overlap with $\mathcal{S}$ after turning on the interaction. We define $\mathcal{P}$ and $\mathcal{Q}$ to be the projectors onto the two subspaces $\mathcal{S}$ and $\mathcal{F}$ respectively,

$$\mathcal{P} = \sum_{\alpha\in\mathcal{S}} |\alpha\rangle\langle\alpha|\,, \quad \mathcal{Q} = \sum_{\beta\in\mathcal{F}} |\beta\rangle\langle\beta|\,, \tag{B.3}$$

where $\mathcal{Q} = 1 - \mathcal{P}$, $\mathcal{P}^2 = \mathcal{P}$ and $\mathcal{Q}^2 = \mathcal{Q}$. By applying these projectors onto Eq. (B.2) and using $\mathcal{Q} = 1 - \mathcal{P}$, the Schrödinger equation can now be written as two coupled equations,

$$\begin{aligned} &\mathcal{P}H\mathcal{P}|u_\alpha\rangle + \mathcal{P}H\mathcal{Q}|u_\alpha\rangle = \epsilon_\alpha\mathcal{P}|u_\alpha\rangle\,, \\ &\mathcal{Q}H\mathcal{P}|u_\alpha\rangle + \mathcal{Q}H\mathcal{Q}|u_\alpha\rangle = \epsilon_\alpha\mathcal{Q}|u_\alpha\rangle\,, \quad |\alpha\rangle\in\mathcal{S}. \end{aligned} \tag{B.4}$$

We are just concerned with the perturbed eigenstates of $\mathcal{S}$, so $||\mathcal{Q}|u_\alpha\rangle|| \ll 1$. We can thus solve the second equation of (B.4) for $\mathcal{Q}|u_\alpha\rangle$ to get,

$$\mathcal{Q}|u_\alpha\rangle = \mathcal{G}(\epsilon_\alpha)\mathcal{Q}V\mathcal{P}|u_\alpha\rangle\,, \tag{B.5}$$

where we used $\mathcal{P}H_0\mathcal{Q} = \mathcal{Q}H_0\mathcal{P} = 0$. $\mathcal{G}(\epsilon_\alpha) = (\epsilon_\alpha\mathbf{1} - \mathcal{Q}H\mathcal{Q})^{-1}$ is the Green's function of the interacting system projected onto the subspace $\mathcal{F}$. We plug Eq. (B.5) into Eq. (B.4) to get an equation which defines the effective Hamiltonian for the subspace $\mathcal{S}$,

$$\mathcal{P}H\mathcal{P}|u_\alpha\rangle + \mathcal{P}V\mathcal{Q}\mathcal{G}(\epsilon_\alpha)\mathcal{Q}V\mathcal{P}|u_\alpha\rangle = \epsilon_\alpha\mathcal{P}|u_\alpha\rangle \equiv H_{eff}\mathcal{P}|u_\alpha\rangle\,, \tag{B.6}$$

with,

$$H_{eff}(\epsilon_\alpha) \equiv \mathcal{P}H\mathcal{P} + \mathcal{P}V\mathcal{Q}\mathcal{G}(\epsilon_\alpha)\mathcal{Q}V\mathcal{P}. \tag{B.7}$$

One can now calculate $\mathcal{G}$ as a perturbative expansion in V,

$$\mathcal{G}(\epsilon_\alpha) = \mathcal{G}_Q\sum_{n=0}^{\infty}(V\mathcal{G}_Q)^n, \tag{B.8}$$

where $\mathcal{G}_Q(\epsilon_\alpha) = \mathcal{Q}(\epsilon_\alpha \mathbf{1} - H_0)^{-1}\mathcal{Q}$ is the Green's function of the non-interacting system projected onto $\mathcal{F}$,

$$\mathcal{G}_Q(\epsilon_\alpha) = \sum_{|\beta\rangle \in \mathcal{F}} \frac{|\beta\rangle \langle\beta|}{\epsilon_\alpha - \epsilon_\beta^{(0)}}. \tag{B.9}$$

The effective Hamiltonian now reads,

$$H_{eff}(\epsilon_\alpha) = \mathcal{P}(H_0 + \mathcal{T}(\epsilon_\alpha))\mathcal{P}, \tag{B.10}$$

where we have defined the scattering matrix $\mathcal{T}$ as,

$$\mathcal{T}(\epsilon_\alpha) = V \sum_{n=0}^{\infty} (\mathcal{G}_Q V)^n. \tag{B.11}$$

Note that the condition $||\mathcal{Q}\,|u_\alpha\rangle\,|| \ll 1$ indicates that $|\,\langle\beta|\mathcal{Q}|u_\alpha\rangle\,| \approx |\,\langle\beta|\mathcal{G}_Q V|\alpha\rangle\,| \ll 1$, so $|\,\langle\beta|V|\alpha\rangle\,| \ll |\epsilon_\beta - \epsilon_\alpha|$, i.e. the coupling between the two subspaces should be much smaller than the gap as stated earlier. The effective Schrödinger Eq. (B.6) is a self-consistent equation as the effective Hamiltonian H_{eff} depends on the unknown energy ϵ_α. To get the effective Hamiltonian to second order, we can approximate $\epsilon_\alpha \approx \epsilon_\alpha^{(0)}$. For higher order corrections, one can solve for the eigenenergies of $H_{eff}(\epsilon_\alpha^{(0)})$ and plug them back to Eq. (B.6) to continue recursively. We however take an alternative approach and make a perturbative ansatz for ϵ_α as explained in the main text.

Bibliography

[1] S. M. Girvin, *Circuit QED: superconducting qubits coupled to microwave photons* in Quantum Machines: Measurement and Control of Engineered Quantum Systems, lecture notes of the Les Houches summer school: volume 96, Oxford University Press (2014).

[2] Crispin Gardiner and Peter Zoller, *The Quantum World of Ultra-Cold Atoms and Light Book II: The Physics of Quantum-Optical Devices*, Imperial College Press (2015).

[3] Charles A. Desoer and Ernest S. Kuh, *Basic Circuit Theory*, McGraw-Hill (1969).

[4] D. P. DiVincenzo, *The physical Implementation of Quantum Computation*, Fortschr. Phys. 48, 2000 (2000).

[5] B. D. Josephson, *Possible new effects in superconductive tunnelling*, Phys. Lett. 1, 251 (1962).

[6] B. D. Josephson, *The discovery of tunnelling supercurrents*, Rev. Mod. Phys. 46, 251 (1974).

[7] Y. Nakamura, Y. A. Pashkin and J. Tsai, *Coherent control of macroscopic quantum states in a single-Cooper-pair box*, Nature 398, 786 (1999).

[8] V. Bouchiat, D. Vion, P. Joyez, D. Esteve, and M. H. Devoret, *Quantum coherence with a single Cooper pair*, Physica Scripta T76, 165 (1998).

[9] Y. Makhlin, G. Scohn and A. Shnirman, *Josephson-junction qubits with controlled couplings*, Nature 398, 305 (1999).

[10] J. E. Mooij, T. P. Orlando, L. Levitov, L. Tian, C. H. van der Wal, and S. Lloyd, *Josephson Persistent-Current Qubit*, Science 285, 1036 (1999).

[11] V. Ambegaokar and A. Baratoff, *Tunneling Between Superconductors*, Phys. Rev. Lett. 10, 486 (1963).

[12] A. Cottet, *Implementation of a Quantum Bit in a Superconducting Circuit*, PhD thesis, Universite Paris VI (2002).

[13] Eric T. Holland, *Cavity State Reservoir Engineering in Circuit Quantum Electrodynamics*, PhD thesis, Yale university (2015).

[14] J. Koch, T. M. Yu, J. Gambetta, A. A. Houck, D. I. Schuster, J. Majer, A. Blais, M. H. Devoret, S. M. Girvin, and R. J. Schoelkopf, *Charge insensitive qubit design derived from the Cooper pair box*, Phys. Rev. A 76, 042319 (2007).

[15] J. A. Schreier, A. A. Houck, J. Koch, D. I. Schuster, B. R. Johnson, J. M. Chow, J. M. Gambetta, J. Majer, L. Frunzio, M. H. Devoret, S. M. Girvin, and R. J. Schoelkopf, *Suppressing charge noise decoherence in superconducting charge qubits*, Phys. Rev. B 77, 180502 (2008).

[16] S. E. Nigg, H. Paik, B. Vlastakis, G. Kirchmair, S. Shankar, L. Frunzio, M. H. Devoret, R. J. Schoelkopf, and S. M. Girvin, *Black-Box Superconducting Circuit Quantization*, Phys. Rev. Lett. 108, 240502 (2012).

[17] V. E. Manucharyan, J. Koch, L. I. Glazman, M. H. Devoret, *Fluxonium: Single Cooper-Pair Circuit Free of Charge Offsets*, Science 326 (2009).

[18] John Clarke, Alex I. Braginski, *The SQUID Handbook, Volume I and II*, Wiley (2006).

[19] John Clarke. *Principles and applications of SQUIDs*, Proceedings of the IEEE 77(8), 1208 (1989).

[20] M. Tinkham, *Introduction to superconductivity*, Dover publication Inc. (2004).

[21] R.J. Johansson, *Quantum mechanics in superconducting circuits and nanomechanical devices*, PhD thesis, Chalmers University of Technology (2009).

[22] M. H. Devoret, A. Wallraff, J. M. Martinis, *Superconducting Qubits: A Short Review*, arXiv:cond-mat/0411174.

[23] M. H. Devoret and J. M. Martinis. *Implementing Qubits with Superconducting Integrated Circuits*, Quant. Info. Proc. 3, 163 (2004).

[24] J. Clarke and F. K. Wilhelm, *Superconducting quantum bits*, Nature 453, 1031 (2008).

[25] G. Wendin and V. S. Shumeiko, *Superconducting Quantum Circuits, Qubits and Computing*, arXiv:cond-mat/0508729.

[26] G. Wendin, *Quantum information processing with superconducting circuits: a review*, Rep. Prog. Phys. 80, 106001 (2017).

[27] D. Vion, A. Aassime, A. Cottet, P. Joyez, H. Pothier, C. Urbina, D. Esteve, M. H. Devoret, *Manipulating the Quantum State of an Electrical Circuit*, Science 296, 886 (2002).

[28] J.R. Friedman, V. Patel, W. Chen, S. Tolpygo, J. E. Lukens, *Quantum superposition of distinct macroscopic states*, Nature 406, 43 (2000).

[29] C.H. Van derWal, A. Ter Haar, F. Wilhelm, R. Schouten, C. Harmans, T. Orlando, S. Lloyd, J. Mooij, *Quantum Superposition of Macroscopic Persistent-Current States*, Science 290, 773 (2000).

[30] I. Chiorescu, Y. Nakamura, C. J. P. M. Harmans, and J. E. Mooij, *Coherent Quantum Dynamics of a Superconducting Flux Qubit*, Science 299, 1869 (2003).

[31] J. M. Martinis, S. Nam, J. Aumentado, C. Urbina, *Rabi Oscillations in a Large Josephson-Junction Qubit*, Phys. Rev. Lett. 89, 117901 (2002).

[32] M. Steffen, M. Ansmann, R. McDermott, N. Katz, R. C. Bialczak, E. Lucero, M. Neeley, E. M. Weig, A. N. Cleland, and J. M. Martinis, *State Tomography of Capacitively Shunted Phase Qubits with High Fidelity*, Phys. Rev. Lett. 97, 050502 (2006).

[33] J.Q. You, X. Hu, S. Ashhab, F. Nori, *Low-decoherence flux qubit*, Phys. Rev. B 75, 140515 (2007).

[34] M. Steffen, S. Kumar, D. P. DiVincenzo, J. R. Rozen, G. A. Keefe, M. B. Rothwell, and M. B. Ketchen, *High-coherence hybrid superconducting qubit*, Phys. Rev. Lett. 105, 100502 (2010).

[35] F. Yan, S. Gustavsson, A. Kamal, J. Birenbaum, A. P. Sears, D. Hover, T. J. Gudmundsen, J. L. Yoder, T. P. Orlando, J. Clarke, A. J. Kerman, and W. D. Oliver, *The flux qubit revisited to enhance coherence and reproducibility*, Nat. Commun. 7, 12964 (2016).

[36] R. Barends, J. Kelly, A. Megrant, A. Veitia, D. Sank, E. Jeffrey, T. C. White, J. Mutus, A. G. Fowler, B. Campbell, Y. Chen, Z. Chen, B. Chiaro, A. Dunsworth, C. Neill, P. O'Malley, P. Roushan, A. Vainsencher, J. Wenner, A. N. Korotkov, A. N. Cleland and John M. Martinis, *Superconducting quantum circuits at the surface code threshold for fault tolerance*, Nature 508, 500 (2014).

[37] J. Kelly, R. Barends, A. G. Fowler, A. Megrant, E. Jeffrey, T. C. White, D. Sank, J. Y. Mutus, B. Campbell, Yu Chen, Z. Chen, B. Chiaro, A. Dunsworth, I.-C. Hoi, C. Neill, P. J. J. O'Malley, C. Quintana, P. Roushan, A. Vainsencher, J. Wenner, A. N. Cleland and John M. Martinis, *State preservation by repetitive error detection in a superconducting quantum circuit*, Nature 519, 66 (2015).

[38] R. Barends, A. Shabani, L. Lamata, J. Kelly, A. Mezzacapo, U. Las Heras, R. Babbush, A. G. Fowler, B. Campbell, Y. Chen, Z. Chen, B. Chiaro, A. Dunsworth, E. Jeffrey, E. Lucero, A. Megrant, J. Y. Mutus, M. Neeley, C. Neill, P. J. J. OŠMalley, C. Quintana, P. Roushan, D. Sank, A. Vainsencher, J. Wenner, T. C. White, E. Solano, H. Neven, and J. M.

Martinis, *Digitized adiabatic quantum computing with a superconducting circuit*, Nature 534, 222 (2016).

[39] E. T. Jaynes, F.W. Cummings, *Comparison of quantum and semiclassical radiation theories with application to the beam maser*, Proc. IEEE. 51, 89 (1963).

[40] J. M. Raimond, M. Brune, and S. Haroche, *Manipulating quantum entanglement with atoms and photons in a cavity*, Rev. Mod. Phys. 73, 565 (2001).

[41] Alexandre Blais, Ren-Shou Huang, Andreas Wallraff, S. M. Girvin, and R. J. Schoelkopf, *Cavity quantum electrodynamics for superconducting electrical circuits: An architecture for quantum computation*, Phys. Rev. A 69, 062320 (2004).

[42] Matthew D. Reed, *Entanglement and Quantum Error Correction with Superconducting Qubits*, PhD thesis, Yale university (2013).

[43] D. I. Schuster, A. A. Houck, J. A. Schreier, A. Wallraff, J. M. Gambetta, A. Blais, L. Frunzio, J. Majer, B. Johnson, M. H. Devoret, S. M. Girvin and R. J. Schoelkopf, *Resolving photon number states in a superconducting circuit*, Nature 445, 515 (2007).

[44] C. Cohen-Tannoudji, J. Dupont-Roc, G. Grynberg, *Atom-Photon Interactions: Basic Processes and Applications*, Wiley (2004).

[45] J. Gambetta, A. Blais, D. I. Schuster, A. Wallraff, L. Frunzio, J. Majer, M. H. Devoret, S. M. Girvin, and R. J. Schoelkopf, *Qubit-photon interactions in a cavity: Measurement-induced dephasing and number splitting*, Phys. Rev. A 74, 042318 (2006).

[46] David I. Schuster, *Circuit Quantum Electrodynamics*, PhD thesis, Yale University (2007).

[47] E. M. Purcell, *Resonance Absorption by Nuclear Magnetic Moments in a Solid*, Phys. Rev. 69, 681 (1946).

[48] A. A. Houck, J. A. Schreier, B. R. Johnson, J. M. Chow, Jens Koch, J. M. Gambetta, D. I. Schuster, L. Frunzio, M. H. Devoret, S. M. Girvin, and R. J. Schoelkopf, *Controlling the Spontaneous Emission of a Superconducting Transmon Qubit*, Phys. Rev. Lett. 101, 080502 (2008).

[49] J. Majer, J. M. Chow, J. M. Gambetta, Jens Koch, B. R. Johnson, J. A. Schreier, L. Frunzio, D. I. Schuster, A. A. Houck, A. Wallraff, A. Blais, M. H. Devoret, S. M. Girvin and R. J. Schoelkopf, *Coupling superconducting qubits via a cavity bus*, Nature 449, 443 (2007).

[50] L. DiCarlo, J. M. Chow, J. M. Gambetta, Lev S. Bishop, B. R. Johnson, D. I. Schuster, J. Majer, A. Blais, L. Frunzio, S. M. Girvin, and R. J. Schoelkopf, *Demonstration of two-qubit algorithms using a superconducting quantum processor*, Nature 460, 240 (2009).

[51] A. Blais, J. Gambetta, A. Wallraff, D. I. Schuster, S. M. Girvin, M. H. Devoret, and R. J. Schoelkopf, *Quantum-information processing with circuit quantum electrodynamics*, Phys. Rev. A 75, 032329 (2007).

[52] J. M. Chow, J. M. Gambetta, L. Tornberg, Jens Koch, Lev S. Bishop, A. A. Houck, B. R. Johnson, L. Frunzio, S. M. Girvin, and R. J. Schoelkopf, *Randomized Benchmarking and Process Tomography for Gate Errors in a Solid-State Qubit*, Phys. Rev. Lett. 102, 090502 (2009).

[53] E. Lucero, M. Hofheinz, M. Ansmann, R. C. Bialczak, N. Katz, M. Neeley, A. D. O'Connell, H. Wang, A. N. Cleland, and J. M.Martinis, *High-Fidelity Gates in a Single Josephson Qubit*, Phys. Rev. Lett. 100, 247001 (2008).

[54] Jerry M. Chow, *Quantum Information Processing with Superconducting Qubits*, PhD thesis, Yale university (2010).

[55] M. H. Devoret, S. Girvin, R. Schoelkopf, *Circuit-QED: How strong can the coupling between a Josephson junction atom and a transmission line resonator be?*, Ann. Phys. 16, 767 (2007).

[56] M. Wallquist, V. S. Shumeiko, and G. Wendin, *Selective coupling of superconducting charge qubits mediated by a tunable stripline cavity*, Phys. Rev. B 74, 224506 (2006).

[57] M. W. McLachlan, *Theory and Applications of Mathieu Functions*, Clarendon Press (1947).

[58] Milton Abramowitz and I. A. Stegun, *Handbook of Mathematical Functions*, Dover publications Inc. (1965).

[59] M. R. Geller, E. Donate, Y. Chen, C. Neill, P. Roushan, and J. M. Martinis, *Tunable coupler for superconducting Xmon qubits: Perturbative nonlinear model*, Phys. Rev. A 92, 012320 (2015).

[60] Y. Chen *et. al.*, *Qubit Architecture with High Coherence and Fast Tunable Coupling*, Phys. Rev. Lett. 113, 220502 (2014).

[61] Dvir Kafri, Chris Quintana, Yu Chen, Alireza Shabani, John M. Martinis, and Hartmut Neven, *Tunable inductive coupling of superconducting qubits in the strongly nonlinear regime*, Phys. Rev. A 95, 052333 (2017).

[62] David C. McKay, Stefan Filipp, Antonio Mezzacapo, Easwar Magesan, Jerry M. Chow, and Jay M. Gambetta, *Universal Gate for Fixed-Frequency Qubits via a Tunable Bus*, Phys. Rev. Applied 6, 064007 (2016).

[63] O. Astafiev, Yu A. Pashkin, T. Yamamoto, Y. Nakamura, and J. S. Tsai. *Single-shot measurement of the Josephson charge qubit*, Phys. Rev. B 69, 180507 (2004).

[64] R. Vijay, M. H. Devoret, and I. Siddiqi, *Invited Review Article: The Josephson bifurcation amplifier*, Rev. Sci. Instrum. 80, 111101 (2009).

[65] François Mallet, Florian R Ong, Agustin Palacios-Laloy, Francois Nguyen, Patrice Bertet, Denis Vion, and Daniel Esteve. *Single-shot qubit readout in circuit quantum electrodynamics*, Nat. Phys. 5, 791 (2009).

[66] L. S. Bishop, L. Tornberg, D. Price, E. Ginossar, A. Nunnenkamp, A. A. Houck, J. M. Gambetta, J. Koch, G. Johansson, S. M. Girvin, and R. J.

Schoelkopf, *Proposal for generating and detecting multi-qubit GHz states in circuit QED*, New J. Phys. 11, 073040 (2009).

[67] Daniel. T. Sank, *Fast, Accurate State Measurement in Superconducting Qubits*, PhD thesis, UCSB (2014).

[68] M. D. Reed, B. R. Johnson, A. A. Houck, L. DiCarlo, J. M. Chow, D. I. Schuster, L. Frunzio, and R. J. Schoelkopf, *Fast reset and suppressing spontaneous emission of a superconducting qubit*, App. Phys. Lett. 96, 203110 (2010).

[69] J. M. Chow, L. DiCarlo, J. M. Gambetta, A. Nunnenkamp, L. S. Bishop, L. Frunzio, M. H. Devoret, S. M. Girvin, and R. J. Schoelkopf, *Detecting highly entangled states with a joint qubit readout*, Phys. Rev. A 81, 062325 (2010).

[70] L. DiCarlo, M. D. Reed, L. Sun, B. R. Johnson, J. M. Chow, J. M. Gambetta, L. Frunzio, S. M. Girvin, M. H. Devoret and R. J. Schoelkopf, *Preparation and measurement of three-qubit entanglement in a superconducting circuit*, Nature 467, 574 (2010).

[71] S. Filipp, P. Maurer, P. J. Leek, M. Baur, R. Bianchetti, J. M. Fink, M. Göppl, L. Steffen, J. M. Gambetta, A. Blais, and A. Wallraff, *Two-Qubit State Tomography Using a Joint Dispersive Readout*, Phys. Rev. Lett. 102, 200402 (2009).

[72] M. H. Devoret, *Quantum Fluctuations in Electrical Circuits* in Quantum Fluctuations ed. by S. Reynaud, E. Giacobino, J. Zinn-Justin, Les Houches Session LXIII, Elsevier (1997).

[73] R. P. Feynman, *Simulating Physics with Computers*, R. P. Int. J. Theor. 21, 467 (1982).

[74] I. M. Georgescu, S. Ashhab, and Franco Nori, *Quantum simulation*, Rev. Mod. Phys. 86, 153 (2014).

[75] Iulia Buluta and Franco Nori, *Quantum Simulators*, Science 326, 108 (2009).

[76] Philipp Hauke, Fernando M. Cucchietti, Luca Tagliacozzo, Ivan Deutsch and Maciej Lewenstein, *Can one trust quantum simulators?*, Rep. Prog. Phys. 75, 082401 (2012).

[77] S. Lloyd, *Universal Quantum Simulators*, Science 23, 1073 (1996).

[78] Tomi H. Johnson, Stephen R. Clark and Dieter Jaksch, *What is a quantum simulator?*, EPJ Quantum Technology 1:10 (2014).

[79] Michael A. Nielsen, Isaac L. Chuang, *Quantum Computation and Information*, Cambridge University Press (2010).

[80] A. Aspuru-Guzik, A. D. Dutoi, P. J. Love, and M. Head-Gordon, *Simulated Quantum Computation of Molecular Energies*, Science 309, 1704-1707 (2005).

[81] A. Friedenauer, H. Schmitz, J. T. Glückert, D. Porras, T. Schätz, *Simulating a quantum magnet with trapped ions*, Nat. Phys. 4, 757 (2008).

[82] R. Babbush, J. McClean, D. Wecker, A. Aspuru-Guzik and N. Wiebe, *Chemical Basis of Trotter-Suzuki Errors in Quantum Chemistry Simulation*, Phys. Rev. A 91, 022311 (2015).

[83] S. Schmidt, J. Koch, *Circuit QED lattices: Towards quantum simulation with superconducting circuits*, Ann. Phys. 525, 395 (2013).

[84] G. S. Paraoanu, *Recent Progress in Quantum Simulation Using Superconducting Circuits*, J. Low. Temp. Phys. 175, 633-654 (2014).

[85] Guillermo Romero, Enrique Solano and Lucas Lamata, *Quantum Simulations with Circuit Quantum Electrodynamics*, in Quantum Simulations with Photons and Polaritons, Editor: Dimitris G. Angelakis, Springer (2017).

[86] S. Schmidt, D. Gerace, A. A. Houck, G. Blatter, and H. E. Türeci, *Nonequilibrium delocalization-localization transition of photons in circuit quantum electrodynamics*, Phys. Rev. B 82, 100507 (2010).

[87] A. Mezzacapo, U. Las Heras, J. S. Pedernales, L. DiCarlo, E. Solano and L. Lamata, *Digital Quantum Rabi and Dicke Models in Superconducting Circuits*, Sci. Rep. 4, 7482 (2014).

[88] N. K. Langford, R. Sagastizabal, M. Kounalakis, C. Dickel, A. Bruno, F. Luthi, D. J. Thoen, A. Endo and L. DiCarlo, *Experimentally simulating the dynamics of quantum light and matter at deep-strong coupling*, Nat. Commun. 8, 1715 (2017).

[89] Y. Salathé, M. Mondal, M. Oppliger, J. Heinsoo, P. Kurpiers, A. Potoćnik, A. Mezzacapo, U. Las Heras, L. Lamata, E. Solano, S. Filipp, and A. Wallraff, *Digital Quantum Simulation of Spin Models with Circuit Quantum Electrodynamics*, Phys. Rev. X 5, 021027 (2015).

[90] D. Ballester, G. Romero, J. J. García-Ripoll, F. Deppe, and E. Solano, *Quantum Simulation of the Ultrastrong-Coupling Dynamics in Circuit Quantum Electrodynamics*, Phys. Rev. X 2, 021007 (2012).

[91] P. Jordan and E. Wigner, *Über das Paulische Äquivalenzverbot*, Zeitschrift Physics 47, 631 (1928).

[92] U. Las Heras, L. García Álvarez, A. Mezzacapo, E. Solano and L. Lamata, *Fermionic models with superconducting circuits*, EPJ Quantum Technology 2, 8 (2015).

[93] R. Barends, L. Lamata, J. Kelly, L. Garía-Álvarez, A. G. Fowler, A Megrant, E Jeffrey, T. C. White, D. Sank, J. Y. Mutus, B. Campbell, Yu Chen, Z. Chen, B. Chiaro, A. Dunsworth, I.-C. Hoi, C. Neill, P. J. J. OŠMalley, C. Quintana, P. Roushan, A. Vainsencher, J. Wenner, E. Solanoăand John M. Martinis, *Digital quantum simulation of fermionic models with a superconducting circuit*, Nat. Commun. 6, 7654 (2015).

[94] J. J. García-Ripoll, E. Solano, M. A. Martin-Delgado, *Quantum simulation of Anderson and Kondo lattices with superconducting qubits*, Phys. Rev. B 77, 024522 (2008).

[95] Martin Leib and Michael J. Hartmann, *Bose-Hubbard dynamics of polaritons in a chain of circuit quantum electrodynamics cavities*, New J. Phys. 12, 093031 (2010).

[96] A. Nunnenkamp, J. Koch, S. M. Girvin, *Synthetic gauge fields and homodyne transmission in Jaynes-Cummings lattices*, New J. Phys. 13, 095008 (2011).

[97] J. Koch, A. A. Houck, K. Le Hur, S. M. Girvin, *Time-reversal symmetry breaking in circuit-QED based photon lattices*, Phys. Rev. A 82, 043811 (2010).

[98] J. Raftery, D. Sadri, S. Schmidt, H. E. Türeci, and A. A. Houck, *Observation of a Dissipation-Induced Classical to Quantum Transition*, Phys. Rev. X 4, 031043 (2014).

[99] Mattias Fitzpatrick, Neereja M. Sundaresan, Andy C. Y. Li, Jens Koch, and Andrew A. Houck, *Observation of a Dissipative Phase Transition in a One-Dimensional Circuit QED Lattice*, Phys. Rev. X 7, 011016 (2017).

[100] A. Mezzacapo, E. Rico, C. Sabín, I. L. Egusquiza, L. Lamata, and E. Solano, *Non-Abelian* $SU(2)$ *Lattice Gauge Theories in Superconducting Circuits*, Phys. Rev. Lett. 115, 240502 (2015).

[101] D. Marcos, P. Rabl, E. Rico, and P. Zoller, *Superconducting Circuits for Quantum Simulation of Dynamical Gauge Fields*, Phys. Rev. Lett. 111, 110504 (2013).

[102] D. Marcos, P. Widmer, E. Rico, M. Hafezi, P. Rabl, U.-J. Wiese, P. Zoller, *Two-Dimensional Lattice Gauge Theories with Superconducting Quantum Circuits*, Ann. Phys. 351, 634 (2014).

[103] Alberto Peruzzo, Jarrod McClean, Peter Shadbolt, Man-Hong Yung, Xiao-Qi Zhou, Peter J. Love, Alán Aspuru-Guzik and Jeremy L. O'Brien, *A variational eigenvalue solver on a photonic quantum processor*, Nat. Commun. 5, 4213 (2014).

[104] P. J. J. O'Malley, R. Babbush, I. D. Kivlichan, J. Romero, J. R. McClean, R. Barends, J. Kelly, P. Roushan, A. Tranter, N. Ding, B. Campbell, Y. Chen, Z. Chen, B. Chiaro, A. Dunsworth, A. G. Fowler, E. Jeffrey, A. Megrant, J. Y. Mutus, C. Neill, C. Quintana, D. Sank, A. Vainsencher, J. Wenner, T. C. White, P. V. Coveney, P. J. Love, H. Neven, A. Aspuru-Guzik, and J. M. Martinis, *Scalable Quantum Simulation of Molecular Energies*, Phys. Rev. X 6, 031007 (2016).

[105] J. Braumüller, M. Marthaler, A. Schneider, H. Rotzinger, M. Weides, and A. V. Ustinov, *Analog quantum simulation of the Rabi model in the ultra-strong coupling regime*, Nat. Commun. 8, 779 (2017).

[106] A. Yu. Kitaev, *Fault-tolerant quantum computation by anyons*, Ann. Phys. 303, 2 (2003).

[107] Mahdi Sameti, Anton Potočnik, Dan E. Browne, Andreas Wallraff, Michael J. Hartmann, *Superconducting quantum simulator for topological order and the toric code*, Phys. Rev. A 95, 042330 (2017).

[108] C. Nayak, S. H. Simon, A. Stern, M. Freedman, and S. Das Sarma, *Non-Abelian anyons and topological quantum computation*, Rev. Mod. Phys. 80, 1083 (2008).

[109] Xiao-Gang Wen, *Topological Order: From Long-Range Entangled Quantum Matter to a Unified Origin of Light and Electrons*, ISRN Condensed Matter Physics, 198710 (2013).

[110] John B. Kogut, *An introduction to lattice gauge theory and spin systems*, Rev. Mod. Phys. 51, 659 (1979).

[111] Daniel Gottesman, *Stabilizer Codes and Quantum Error Correction*, arXiv:quant-ph/9705052.

[112] J. Kempe, A. Kitaev, and O. Regev, *The Complexity of the Local Hamiltonian Problem*, SIAM J. Comput. 35, 1070 (2006).

[113] R. König, *Simplifying quantum double Hamiltonians using perturbative gadgets*, Quantum Inf. Comput. 10, 292 (2010).

[114] C. G. Brell, S. Flammia, S. Bartlett, and A. Doherty, *Toric codes and quantum doubles from two-body Hamiltonians*, New J. Phys. 13, 053039 (2011).

[115] Austin G. Fowler, Matteo Mariantoni, John M. Martinis, Andrew N. Cleland, *Surface codes: Towards practical large-scale quantum computation*, Phys. Rev. A 86, 032324 (2012).

[116] Eric Dennis, Alexei Kitaev, Andrew Landahl, John Preskill, *Topological quantum memory*, J. Math. Phys. 43, 4452-4505 (2002).

[117] M. Dalmonte, S. Montangero, *Lattice gauge theories simulations in the quantum information era*, Contemporary Physics 57, 388 (2016).

[118] Jiannis K. Pachos, *Introduction to Topological Quantum Computation*, Cambridge University Press (2012).

[119] Sergey Bravyi, David DiVincenzo, Daniel Loss, *Schrieffer-Wolff transformation for quantum many-body systems*, Ann. Phys. 326, 2793 (2011)

[120] Michal Leskes, P. K. Madhu, Shimon Vega, *Floquet theory in solid-state nuclear magnetic resonance*, Prog. Nucl. Magn. Reson. Spectrosc. 57, 345 (2010).

[121] Ingo Scholz, Jacco D. van Beek, Matthias Ernst, *Operator-based Floquet theory in solid-state NMR*, Solid State Nucl. Magn. Reson. 37, 39 (2010).

[122] N. Goldman and J. Dalibard, *Periodically Driven Quantum Systems: Effective Hamiltoninas and Engineered Gauge Fields*, Phys. Rev. X 4, 031027 (2014).

[123] N. A. Masluk, I. M. Pop, A. Kamal, Z. K. Minev, and M. H. Devoret, *Microwave Characterization of Josephson Junction Arrays: Implementing a Low Loss Superinductance*, Phys. Rev. Lett. 109, 137002 (2012).

[124] M. T. Bell, I. A. Sadovskyy, L. B. Ioffe, A. Yu. Kitaev, and M. E. Gershenson, *Quantum Superinductor with Tunable Non-Linearity*, Phys. Rev. Lett. 109, 137003 (2012).

[125] N. Samkharadze, A. Bruno, P. Scarlino, G. Zheng, D. P. DiVincenzo, L. DiCarlo, and L. M. K. Vandersypen, *High-Kinetic-Inductance Superconducting Nanowire Resonators for Circuit QED in a Magnetic Field*, Phys. Rev. Appl. 5, 044004 (2016).

[126] Justyna Łodyga, Paweł Mazurek, Andrzej Grudka, Michał Horodecki, *Simple scheme for encoding and decoding a qubit in unknown state for various topological codes*, Sci. Rep. 5, 8975 (2015).

[127] Alioscia Hamma and Daniel A. Lidar, *Adiabatic Preparation of Topological Order*, Phys. Rev. Lett. 100, 030502 (2008).

[128] A. Palacios-Laloy, F. Nguyen, F. Mallet, P. Bertet, D. Vion, D. Esteve, *Tunable Resonators for Quantum Circuits*, J. Low Temp. Phys. 151, 1034 (2008).

[129] M. Sandberg, F. Persson, I. C. Hoi, C. M. Wilson and P. Delsing, *Exploring circuit quantum electrodynamics using a widely tunable superconducting resonator*, Phys. Scr. T137, 014018 (2009).

[130] André Eckardt, Egidijus Anisimovas, *High-frequency approximation for periodically driven quantum systems from a Floquet-space perspective*, New. J. Phys. 17, 093039 (2015).

[131] M. Holthaus, *Floquet engineering with quasienergy bands of periodically driven optical lattices*, J. Phys. B: At. Mol. Opt. Phys 49, 013001 (2016).

[132] M. Bukov, L. D'Alessio and A. Polkovnikov, *Universal high-frequency behaviour of periodically driven systems: from dynamical stabilization to Floquet engineering*, Adv. Phys. 64, 139 (2015).

[133] M. P. Silveri, J. A. Tuorila, E. V. Thuneberg and G. S. Paraoanu, *Quantum systems under frequency modulation*, Rep. Prog. Phys. 80 056002 (2017).

[134] Chad Rigetti, Alexandre Blais, and Michel Devoret, *Protocol for Universal Gates in Optimally Biased Superconducting Qubits*, Phys. Rev. Lett. 94, 240502 (2005).

[135] Matthew Reagor *et al.*, *Demonstration of universal parametric entangling gates on a multi-qubit lattice*, Sci. Adv. 4, eaao3603 (2018).

[136] Chad Rigetti and Michel Devoret, *Fully microwave-tunable universal gates in superconducting qubits with linear couplings and fixed transition frequencies*, Phys. Rev. B 81, 134507 (2010).

[137] Jerry M. Chow, A. D. Córcoles, Jay M. Gambetta, Chad Rigetti, B. R. Johnson, John A.Smolin, J. R. Rozen, George A. Keefe, Mary B. Rothwell, Mark B. Ketchen, and M. Steffen, *Simple All-Microwave Entangling Gate for Fixed Frequency Superconducting Qubits*, Phys. Rev. Lett. 107, 080502 (2011).

[138] Jerry M. Chow, Jay M. Gambetta, Andrew W. Cross, Seth T. Merkel, Chad Rigetti and M. Steffen, *Microwave-activated conditional-phase gate for superconducting qubits*, New J. Phys. 15 115012 (2013).

[139] G. S. Paraoanu, *Microwave-induced coupling of superconducting qubits*, Phys. Rev. B 74, 140504 (2006).

[140] Anne M. Forney, Steven R. Jackson, and Frederick W. Strauch, *Multi-frequency control pulses for multilevel superconducting quantum circuits*, Phys. Rev. A 81, 012306 (2010).

[141] Eliot Kapit, *Universal two-qubit interactions, measurement, and cooling for quantum simulation and computing*, Phys. Rev. A 92, 012302 (2015).

[142] M. Grifoni and P. Hänggi, *Driven quantum tunneling*, Phys. Rep. 304, 229 (1998).

[143] G. Floquet, *Sur les équations différentielles linéaires á coefficients périodiques*, Annales de Í École Normale Supérieure 12, 47 (1883).

[144] Jon H. Shirley, *Solution of the Schrödinger Equation with a Hamiltonian Periodic in Time*, Phys. Rev. 138, B979 (1965).

[145] Hideo Sambe, *Steady States and Quasienergies of a Quantum-Mechanical System in an Oscillating Field*, Phys. Rev. A 7, 2203 (1973).

[146] Tak-San Ho, Shih-I Chu, James V. Tietz, *Semiclassical many-mode floquet theory*, Chem. Phys. Lett. 96, 464 (1983).

[147] S. I. Chu and D. A. Telnov, *Beyond the Floquet theorem: generalized Floquet formalisms and quasienergy methods for atomic and molecular multiphoton processes in intense laser fields*, Phys. Rep. 390, 1 (2004).

[148] Shih-I Chu, *Generalized Floquet Theoretical Approaches to Intense-Field Multiphoton and Nonlinear Optical Processes*, Adv. Chem. Phys. 73, 739 (1999).

[149] Sang-Kil Son, Siyuan Han, and Shih-I Chu, *Floquet formulation for the investigation of multiphoton quantum interference in a superconducting qubit driven by a strong ac field*, Phys. Rev. A 79, 032301 (2009).

[150] Tak-San Ho and Shih-I Chu, *Semiclassical many-mode Floquet theory. II. Nonlinear multiphoton dynamics of a two-level system in a strong bichromatic field*, J. Phys. B: At. Mol. Phys. 17, 2101 (1984).

[151] J. H. Van Vleck, *On σ-Type Doubling and Electron Spin in the Spectra of Diatomic Molecules*, Phys. Rev. 33, 467 (1929).

[152] H. Salwen, *Resonance Transitions in Molecular Beam Experiments. I. General Theory of Transitions in a Rotating Magnetic Field*, Phys. Rev. 99, 1274 (1955).

[153] N. Goldman, J. Dalibard, M. Aidelsburger, and N. R. Cooper, *Periodically driven quantum matter: The case of resonant modulations*, Phys. Rev. A 91, 033632 (2015).

[154] Johannes Hausinger and Milena Grifoni, *Dissipative two-level system under strong ac driving: A combination of Floquet and Van Vleck perturbation theory*, Phys. Rev. A 81, 022117 (2010).

[155] Alexei Kitaev, *Anyons in an exactly solved model and beyond*, Ann. Phys. 321, 2 (2006).

[156] F. Wilczek, *Majorana returns*, Nat. Phys. 5, 614 (2009).

[157] N. Read and D. Green, *Paired states of fermions in two dimensions with breaking of parity and time-reversal symmetries and the fractional quantum Hall effect*, Phys. Rev. B 61, 10267 (2000).

[158] Elliott H. Lieb, *Flux Phase of the Half-Filled Band*, Phys. Rev. Lett. 73, 2158 (1994).

[159] H.-D. Chen and Z. Nussinov, *Exact results of the Kitaev model on a hexagonal lattice: spin states, string and brane correlators, and anyonic excitations*, J. Phys. A 41, 075001 (2008).

[160] J. Q. You, Xiao-Feng Shi, Xuedong Hu, and Franco Nori, *Quantum emulation of a spin system with topologically protected ground states using superconducting quantum circuits*, Phys. Rev. B 81, 014505 (2010).

[161] G. Kells, N. Moran and J. Vala, *Finite size effects in the Kitaev honeycomb lattice model on a torus*, J. Stat. Mech. P03006, (2009)

[162] Hong-Chen Jiang, Zheng-Cheng Gu, Xiao-Liang Qi, and Simon Trebst, *Possible proximity of the Mott insulating iridate* Na_2IrO_3 *to a topological phase: Phase diagram of the Heisenberg-Kitaev model in a magnetic field*, Phys. Rev. B 83, 245104 (2011).

[163] Claudio Castelnovo and Claudio Chamon, *Entanglement and topological entropy of the Toric code at finite temperature*, Phys. Rev. B 76, 184442 (2007).

[164] R. Alicki, M. Fannes and M. Horodecki, *On thermalization in Kitaev's 2D model*, J. Phys. A: Math. Theor. 42, 065303 (2009).

[165] O. Viyuela, A. Rivas and M. A. Martin-Delgado, *Generalized toric codes coupled to thermal baths*, New J. Phys. 14 033044 (2012).

[166] Eliot Kapit, Mohammad Hafezi, and Steven H. Simon, *Induced Self-Stabilization in Fractional Quantum Hall States of Light*, Phys. Rev. X 4, 031039 (2014).

[167] Charles-Edouard Bardyn, Torsten Karzig, *Exponential lifetime improvement in topological quantum memories*, Phys. Rev. B 94, 094303 (2016).

[168] Kevin C. Young, Mohan Sarovar, Jon Aytac, C. M. Herdman and K. Birgitta Whaley, *Finite temperature quantum simulation of stabilizer Hamiltonians*, J. Phys. B 45, 154012 (2012).

[169] Yi-Cong Zheng and Hui-Khoon Ng, *Digital quantum simulator in the presence of a bath*, Phys. Rev. A 96, 042329 (2017).

[170] U.-J. Wiese, *Ultracold quantum gases and lattice systems: quantum simulation of lattice gauge theories*, Ann. Phys. 525, 777 (2013).

[171] Erez Zohar, J. Ignacio Cirac, Benni Reznik, *Quantum simulations of lattice gauge theories using ultracold atoms in optical lattices*, Rep. Prog. Phys. 79, 014401 (2016).

[172] Esteban A. Martinez, Christine A. Muschik, Philipp Schindler, Daniel Nigg, Alexander Erhard, Markus Heyl, Philipp Hauke, Marcello Dalmonte, Thomas Monz, Peter Zoller and Rainer Blatt, *Real-time dynamics of lattice gauge theories with a few-qubit quantum computer*, Nature 534, 516 (2016).

[173] P. Hauke, D. Marcos, M. Dalmonte, and P. Zoller, *Quantum Simulation of a Lattice Schwinger Model in a Chain of Trapped Ions*, Phys. Rev. X 3, 041018 (2013).

[174] Uwe-Jens Wiese, *Towards quantum simulating QCD*, Nucl. Phys. A931, 246 (2014).

[175] Wolfgang Lechner, Philipp Hauke and Peter Zoller, *A quantum annealing architecture with all-to-all connectivity from local interactions*, Sci. Adv. 1, e1500838 (2015).

[176] N. Chancellor, S. Zohren and P. A. Warburton, *Circuit design for multibody interactions in superconducting quantum annealing systems with applications to a scalable architecture*, npj Quantum Information 3, 21 (2017).

[177] Shruti Puri, Christian Kraglund Andersen, Arne L. Grimsmo and Alexandre Blais, *Quantum annealing with all-to-all connected nonlinear oscillators*, Nat. Commun. 8, 15785 (2017).

[178] M. Hafezi, P. Adhikari, and J. M. Taylor, *Engineering three-body interaction and Pfaffian states in circuit QED systems*, Phys. Rev. B 90, 060503 (2014).

[179] Yi-Chan Lee, Courtney Brell and Steven T. Flammia, *Topological quantum error correction in the Kitaev honeycomb model*, J. Stat. Mech. 2017, 083106 (2017).